FAST SOLUTION TO ELECTROMAGNETIC SCATTERING BY LARGE-SCALE COMPLICATED STRUCTURES USING ADAPTIVE INTEGRAL METHOD

EWE WEI BIN

NATIONAL UNIVERSITY OF SINGAPORE

2004

FAST SOLUTION TO ELECTROMAGNETIC SCATTERING BY LARGE-SCALE COMPLICATED STRUCTURES USING ADAPTIVE INTEGRAL METHOD

EWE WEI BIN

(*B.Eng.(Hons.), Universiti Teknologi Malaysia*)

A THESIS SUBMITTED

FOR THE DEGREE OF DOCTOR OF PHILOSOPHY

DEPARTMENT OF ELECTRICAL AND COMPUTER ENGINEERING

NATIONAL UNIVERSITY OF SINGAPORE

2004

Acknowledgements

First of all, I would like to express my gratitude to my supervisors, Associate Professor Li Le-Wei and Professor Leong Mook Seng, for their invaluable guidance. Without their advice and encouragement, this thesis would not have been possible.

I would also like to thank Mr. Sing Cheng Hiong of the Microwave Research Laboratory and Mr. Ng Chin Hock of the Radar & Signal Processing Laboratory for their kind cooperation and assistance during my studies.

And also my thanks go to Mr. Ng Tiong Huat, Mr. Li Zhong-Cheng, Mr. Wang Yaojun, Mr. Chua Chee Parng, Mr. Gao Yuan, Mr. Chen Yuan and other friends in Microwave Research Laboratory for their help, friendship and fun.

Finally, I am grateful to my family members for their support throughout my studies.

Table of Contents

Summary

In this thesis, electromagnetic scattering by large and complex objects is studied. We have considered the large-scale electromagnetic problems of three types of scatterers, i.e., perfectly electric conducting (PEC) objects, dielectric objects, and composite conducting and dielectric objects. The electromagnetic problems of these objects are formulated using the integral equation method and solved by using the method of moments (MoM) accelerated using the adaptive integral method (AIM).

The electromagnetic analysis of PEC object is performed using the surface integral equation (SIE). The MoM is applied to convert the resultant integral equations into a matrix equation and solved by an iterative solver. The adaptive integral method is implemented to reduce memory requirement for the matrix storage and to accelerate the matrix-vector multiplications in the iterative solver. Numerical examples are presented to demonstrate the accuracy of the solver. The fast solutions to electromagnetic scattering and radiation problems of real-life electrically large metallic objects are also presented.

Next, the electromagnetic scattering by dielectric object is considered. The problem is formulated by using the SIE and the volume integral equation (VIE), respectively. The integral equations are converted into matrix equations in the MoM procedure. The AIM is modified to cope with the additional material information. Numerical examples are presented to demonstrate the applicability of the modified AIM to characterize scattering by large-scale dielectric objects.

For the electromagnetic scattering by composite conducting and dielectric objects, it is described using the SIE and the hybrid volume-surface integral equation, respectively. The MoM is used to discretize the integral equations and convert them into matrix equations. The AIM is altered in order to consider the interaction between different materials, i.e., conductor and dielectric object. Several examples are presented to demonstrate again the capability of the modified AIM for scattering by large-scale composite conducting and dielectric objects.

In addition to the AIM, preconditioning techniques such as diagonal preconditioner, block-diagonal preconditioner, zero fill-in ILU preconditioner and ILU with threshold preconditioner have also been used to further accelerate the solution of the scattering problems. These preconditioners are constructed by using the near-zone matrix generated by the AIM. By using these preconditioners, the number of iterations and the overall solution time have been effectively reduced.

List of Figures

List of Tables

Chapter 1

Introduction

1.1 Background and Motivation

The study of electromagnetic scattering is a challenging field in science and engineering. It has a wide range of engineering applications, such as tracking aircraft using radar, observing the Earth using remote sensing satellites, etc. Electromagnetic scattering can be considered as the *disturbance* caused by an obstacle or scatterer to the original field configurations. It is desirable to solve the scattering problems using an analytical method and obtain closed-form or approximate solutions. However, only a limited number of electromagnetic scattering problems can be solved exactly using an analytical method. Tedious experiments and measurements must be carried out for those problems which cannot be solved by analytical methods.

In order to tackle the electromagnetic scattering problems of real life applications, which normally have no simple solutions, one can use numerical methods to obtain an approximate solution. By using a digital computer, one can solve the complicated scattering problems numerically and obtain solutions with *acceptable* accuracy. Method of moments (MoM) is a numerical method that has been widely used in solving electromagnetic problems. The MoM discretizes the integral

equations and converts them into a dense matrix equation. The matrix storage requirement for the matrix is of $O(N^2)$. The matrix equation can be solved by using either a direct solver or an iterative solver. A direct solver, such as the Gaussian Elimination, solves the matrix equation in $O(N^3)$ floating-point operations. On the other hand, all iterative solvers require matrix-vector multiplications at every iteration, where the operation is in the order of $O(N^2)$. Hence the total computational cost of an iterative solver is of $O(N_{iter}N^2)$ where the N_{iter} is the number of iterations to achieve convergence. It is obviously advantageous to solve the matrix equation using an iterative solver.

The matrix-vector multiplication is normally the bottleneck of iterative solvers. The $O(N^2)$ computational complexity is prohibitively high for a large value of N. Moreover, the $O(N^2)$ matrix storage requirement has also prevented the iterative solver from solving a matrix equation with a large number of unknowns. These stringent computational requirements have prevented the MoM from solving scattering problems of electrically large objects. The complexity increase if the object is made of complex material since additional unknowns are required to properly characterize the material properties. Hence the large-scale electromagnetic problems can only be solved by expensive supercomputer or workstation. Large-scale electromagnetic problems are unlikely to be solved on a personal computer, which has only limited computing resources.

The shortcomings of MoM have motivated the work in this thesis. The objective of this thesis is to develop a numerical method that is able to solve large-scale electromagnetic scattering problems in a fast and efficient manner through the use of a personal computer. This method is based on the MoM, where the scattering problems are characterized by the integral equation method, and a fast algorithm technique is applied to reduce the memory requirement and to accelerate the solution time. We have first focused on the fast solution to the electromagnetic scattering problems involved perfect electric conductors. Then the method is modified and is applied to analyze electromagnetic scattering by objects with complex

material properties.

1.2 Literature Review

The analysis of electromagnetic problems using the integral equation method is a rather classical method in the field of electromagnetic wave theory. Before the computer era, the work on integral equation method was focused on getting good approximate or asymptotic solutions. With the advancement of digital computer, numerical methods have been developed to obtain approximate solutions for the Maxwell's equations. The numerical treatments of various electromagnetic problems using an integral equation method can be traced back to 1960s [1–10]. Several papers were presented to deal with two-dimensional (2-D) electromagnetic problems such as the scattering problems of infinitely long cylinders [1, 3, 5, 7]. The three dimensional (3-D) electromagnetic problems for wire antennas and surface scatterers have also been studied extensively [2, 6, 8–10].

In 1968, R. F. Harrington published a book on obtaining numerical solutions of electromagnetic problems formulated by the integral equation method [11]. In his book, he used the reaction concept and integral equations to develop a systematic and functional-space method for solving electromagnetic problems. This technique was later named as the method of moments, whose name was adopted from the related works published by other researchers during that period of time [12, 13]. The MoM is a general method for solving linear operator equations and it approximates the solution of the unknown quantities by using a finite series of *basis functions*. The MoM can be applied to solve electromagnetic problems of arbitrary linear structures. However, the capability of the MoM is dependent on the speed and available storage of a digital computer.

1.2.1 Methods for the Analysis of Metallic Structures

In 1966, Richmond presented a method for the analysis of an arbitrarily shaped metallic structure with the surface modeled by wire grids [8]. It is simple to model the metallic surface with wire grids and easy to implement it into computer codes. However, this method is not suitable for the computation of near fields and its accuracy has also been questioned [14].

The direct modeling of metallic surfaces has been used to overcome the weakness of wire girds method. Andreasen was the first person who applied the electric field integral equation (EFIE) to analyze the 3-D metallic structure of bodies of revolution (BoR) [4], but the MoM solution of the BoR was given by Mautz and Harrington in 1969 [15]. Mautz and Harrington also showed that the EFIE and magnetic field integral equation (MFIE) do not have an unique solution due to the interior resonance of BoR. They proposed a remedy, the combined field integral equation (CFIE), to eliminate the interior resonance problem and produce accurate an solution [16].

Oshiro proposed a method called Source Distribution Technique to analyze scattering problems of general 3-D metallic structures [9]. He discretized the surface into small cells and the current is assumed to be constant over each of the small cells. The unknown currents are determined by using point matching to the integral equations. Knepp and Goldhirsh had used the second-order quadrilateral patches to the metallic surface and applied point matching to the MFIE [17]. Wang et. al. used the quadrilateral patches to model rectangular plate and applied the Galerkin method to solve the EFIE [18]. The analysis of structures consisting of both wires and metallic surface has been reported by Newman and Pozar [19].

In 1980, the rooftop basis functions that are defined over a pair of rectangular patches were proposed by Glisson and Wilton to solve EFIE [20]. These basis functions have eliminated the fictitious line charges that exist in the EFIE. Rao et. al. implemented the basis functions on triangular patches, which provide better modeling capability [21]. This method has been widely used in electromagnetic simulation

for surface scatterers.

1.2.2 Methods for the Analysis of Dielectric Structures

The numerical analysis of dielectric objects is more complicated than the analysis of metallic objects. The analysis of 2-D object was reported by Richmond [5, 7]. In his papers, he presented numerical treatment to the infinitely long inhomogeneous cylinder illuminated by TM and TE waves. The unknown currents are assumed constant over the discretized cells and point matching is applied to the volume EFIE.

In 1973, Poggio and Miller formulated the integral equations for piecewise homogeneous dielectric objects [22]. Chang and Harrington adopted the formulation to analyze material cylinders [23] while Wu and Tsai used the formulation to analyze lossy dielectric BoR [24]. This formulation is commonly referred as the PMCHWT formulation. Later, Mautz and Harrington presented a more general equation for the analysis of dielectric BoR [25]. The analysis of an arbitrarily shaped 3-D dielectric object was given by Umashankar et. al. [26]. They used the triangular patches to model the dielectric surface and performed the analysis using PMCHWT formulation. Sarkar et. al. extended this method to analyze lossy dielectric objects [27]. In 1994, Medgyesi-Mitschang et. al. generalized the method by considering the junction problems of dielectric objects [28].

In 1984, Schaubert et. al. used the rooftop basis functions that are defined on a pair of tetrahedral elements to the analysis of 3-D dielectric object [29]. These basis functions are used together with the Galerkin procedure of moment method for solving the volume EFIE. This method is best suitable for the analysis of an inhomogeneous dielectric object.

1.2.3 Methods for the Analysis of Composite Conducting and Dielectric Structures

The analysis of composite conducting and dielectric objects is the combination of the analysis of metallic and dielectric structures. In 1979, Medgyesi-Mitschang and Eftimiu reported the analysis of metallic BoR coated with dielectric material [30]. In their method, they applied the EFIE to the metallic structure and PMCHWT formulation to the dielectric structure. The analysis of BoR with metallic and dielectric junctions was carried out by Medgyesi-Mitschang and Putnam [31, 32]. Rao et. al. applied the rooftop basis functions and Garlekin procedure moment method to the analysis of conducting bodies coated with lossy materials [33]. Medgyesi-Mitschang et. al. used the same method except that the CFIE was applied to the closed metallic structure [28].

In 1988, Jin et. al. formulated the hybrid volume-surface integral equations (VSIE) to analyze the composite conducting and dielectric structures [34]. Lu and Chew discretized the dielectric region and surface of the conductor using the tetrahedral elements and triangular patches, respectively and applied rooftop basis functions to solve the resultant VSIE [35].

1.2.4 Fast Algorithms

The method of moments (MoM) was developed to discretize the integral equation and convert it into a matrix equation. Solving the matrix equation generated by MoM using a direct solver requires $O(N^3)$ operations. On the other hand, solving the matrix equation using iterative solver in straightforward manner requires computational complexity of $O(N^2)$ per iteration.

Many fast solutions have been proposed to speed up the matrix-vector multiplication of the iterative solver. Greengard and Rokhlin had devised a fast multipole algorithm to solve static problems [36]. This algorithm has been extended to solve the integral equation for electromagnetic scattering problems and it is commonly

known as fast multipole method (FMM) [37–40]. The computational complexity and storage requirement of the FMM are $O(N^{1.5})$ and $O(N^{1.5}\log N)$, respectively. The FMM makes use of the addition theorem for the Bessel function to translate it from one coordinate system to another one. By doing this, one just needs to discretize the scatterer and place the sub-scatterers into groups. The aggregate radiation pattern of the sub-scatterers of every group is calculated and translated to non-neighbor groups with the aid of addition theorem. This reduces the computational complexity as one just needs to compute the direct interaction between the elements within same group and its neighboring groups, and approximates the far-field interactions using the FMM. Later, the multilevel version of FMM, Multilevel FMM Algorithm (MLFMA), was proposed to further reduce the computational complexity and storage requirement to $O(N\log N)$ and $O(N)$, respectively [41–45]. Even the MLFMA exhibits $O(N\log N)$ complexity, however the large constant factor in this asymptotic bound make it incompetent to other fast algorithms in certain cases.

Fast algorithms based on the fast Fourier transform (FFT) algorithm have also been proposed to reduce the computational complexity of the iterative solvers [46–68]. By exploiting the translation invariance of the Green's function, the convolution in the integral equation can be computed by using the FFT and multiplication in the Fourier space. When the FFT is incorporated into the conjugate gradient (CG) algorithm, the resulting method is called the CG-FFT method [46, 61–68]. The computational complexity and storage requirements of CG-FFT are $O(N\log N)$ and $O(N)$, respectively. However, the CG-FFT requires the integral equation to be discretized on uniform rectangular grids and this has limited its usage to complex 3-D objects. The staircase approximation due to the approximation of curved boundaries by using uniform grids will produce error in the final solution. To overcome the weakness of the CG-FFT, Bleszynski et. al. have presented another grid-based solver, adaptive integral method (AIM) to solve electromagnetic scattering problems [47, 48]. This method retains the advantages of CG-FFT and offers excellent modeling capability and flexibility by using triangular

patches. Similar approaches have been also used by the precorrected-FFT method [58–60].

Among these three types of fast algorithms we have discussed, only MLFMA and AIM are suitable for the electromagnetic analysis of arbitrarily shaped geometries. After considering the project requirements and the advantages of the AIM (such as less memory requirement for the setup and relatively simple implementation on personal computer as compared to the FMM), we have chosen the AIM as the fast algorithm to be used and further enhanced in this thesis.

1.3 Outline of Thesis

This thesis contains eight chapters. Chapter 2 presents the derivation of integral equations for the electromagnetic scattering problems, which will be used in the subsequent chapters. Method of moments, the numerical method for solving the electromagnetic problems formulated by an integral equation method, will also be given.

Chapter 3 introduces the Adaptive Integral Method, which will be used to accelerate the matrix-vector multiplication in iterative solver and to reduce storage requirement. The accuracy, computational complexity and matrix storage requirement issues in our AIM implementation will also be discussed.

The AIM analysis of electromagnetic scattering problem of metallic structures will be presented in Chapter 4. Chapter 5 analyzes the scattering problem of dielectric objects based on the use of the AIM. Chapter 6 presents the application of the AIM to analyze the scattering problem of composite conducting and dielectric objects. The research work in these chapters will focus on the accuracy and applicability of the AIM in solving the scattering problems of different type of scatterers.

In Chapter 7, preconditioning techniques will be presented to accelerate the convergence rate of the iterative solver. Numerical examples will be presented to

demonstrate the performance of the preconditioners on solving scattering problems formulated using integral equations.

Finally, the conclusion and suggestions for future works will be given in Chapter 8.

1.4 Some Original Contributions

In consideration of the earlier proposed integral equations which were established based on surface meshes only, the new contributions of the present thesis in the course of research are:

1. Development of fast algorithms for full wave analysis of horn antenna and parabolic reflector.

2. Further development of fast algorithms based on the AIM for solving electromagnetic scattering problem of dielectric objects and composite dielectric and conducting objects characterized using the surface integral equation method.

3. New development of fast algorithms based on the AIM for solving electromagnetic scattering problem of composite dielectric and conducting objects characterized using the hybrid volume-surface integral equation method.

4. Development of preconditioning algorithms for the iterative solver. Simple and efficient preconditioning algorithms based on the incomplete lower-upper (ILU) decomposition have been developed to accelerate the convergence of the iterative solution.

The contributions of our research have resulted in the following publications:

1.4.1 Article in Monograph Series

1. W. B. Ewe, L. W. Li and M. S. Leong, "Solving mixed dielectric/conducting scattering problem using adaptive integral method," *Progress In Electromag-*

netics Research, vol. 46, pp. 143–163, 2004, EMW Publishing: Boston, MA.

1.4.2 Journal Articles

1. W. B. Ewe, L. W. Li and M. S. Leong, "Fast solution of mixed dielectric/conducting scattering problem using volume-surface adaptive integral method," *IEEE Transactions on Antennas and Propagation*, vol. 52, no. 11, pp. 3071–3077, November 2004.

2. W. B. Ewe, L. W. Li, Q. Wu and M. S. Leong, "Preconditioners for adaptive integral method implementation," *IEEE Transactions on Antennas and Propagation*, accepted for publication, January 2005.

3. W. B. Ewe, L. W. Li, Q. Wu and M. S. Leong, "AIM solution to electromagnetic scattering using parametric geometry," *IEEE Antennas and Wireless Propagation Letters*, accepted for publication, January 2005.

4. W. B. Ewe, L. W. Li, Q. Wu and M. S. Leong, "Analysis of reflector and horn antennas using adaptive integral method," *IEICE Transactions on Communications: Special Section on 2004 International Symposium on Antennas and Propagation*, vol. E88-B, no. 6, June 2005.

1.4.3 Conference Presentations

1. W. B. Ewe, Y. J. Wang, L. W. Li and E. P. Li, "Solution of scattering by homogeneous dielectric bodies using parallel pre-corrected FFT algorithm," in *Proc. of International Conference on Scientific and Engineering Computation*, Singapore, December 2002, pp. 348–352.

2. W. B. Ewe, L. W. Li, and M. S. Leong, "Solving electromagnetic scattering of mixed dielectric conducting object using volume-surface adaptive integral method," in *Proc. of 2003 Progress In Electromagnetics Research Symposium (PIERS'03)*, Singapore, October 2003, pp. 164.

3. W. B. Ewe, L. W. Li and M. S. Leong, "Solution to scattering problem of composite conducting/dielectric body using Adaptive Integral Method," in *Proc. of 2003 International Symposium on Antennas, Propagation, and EM Theory*, Beijing, China, October 2003, pp. 445–447.

4. W. B. Ewe, L. W. Li and M. S. Leong, "Solving mixed dielectric scattering problem using Adaptive Integral Method," in *Proc. of 2003 Asia Pacific Microwave Conference*, vol. 2, Seoul, Korea, November 2003, pp. 732–734.

5. W. B. Ewe, L. W. Li and M. S. Leong, "A novel preconditioner (ILU) for Adaptive Integral Method implementation in solving large-scale electromagnetic scattering problem of composite dielectric and conducting objects," *Proc. of* 5^{th} *ARPU Doctoral Student Conference* (in CD format and web-database), Sydney, Australia, August 2004.

6. W. B. Ewe, L. W. Li and M. S. Leong, "Analysis of reflector and horn antennas using Adaptive Integral Method," in *Proc. of 2004 International Symposium on Antennas and Propagation*, Sendai, Japan, August 2004, pp. 229–232.

7. W. B. Ewe, L. W. Li and M. S. Leong, "Preconditioning techniques for Adaptive Integral Method implementation in fast codes," in *Proc. of 2004 Progress In Electromagnetics Research Symposium (PIERS'04)*, Nanjing, China, August 2004, p. 29.

Chapter 2

Integral Equation Method In Computational Electromagnetics

2.1 Introduction

The integral equation method has been used in computational electromagnetics to solve for the unknown source distribution of an electromagnetic problem. It is in contrast to the differential equation method which emphasizes on solving the electromagnetic field. By using the integral equation method, the relationship between the field and source can be established using the integro-differential equation. And together with equivalence principles, one can formulate integral equations to describe the electromagnetic scattering problem of a scatterer. The resultant integral equations can be solved by using numerical methods. The method of moments (MoM) is the most popular numerical method for solving the integral equation of electromagnetic problems [69–76]. By employing the MoM, the unknown source distribution is discretized by using a set of known functions and converted into a matrix equation which can be solved by various type of matrix solvers.

In this chapter, we will derive the integral equations that will be used in the subsequent chapters. Next, we will also explain the use of MoM in solving the

integral equations of electromagnetic problems.

2.2 Integral Equations

In this section, we will first derive the relationship between a source and its resultant field. Then we will carry out the derivation of integral equations for electromagnetic problems by using two equivalence principles, i.e., surface equivalence principle and volume equivalence principle. In the following derivation and throughout the thesis, the time factor e^{jwt} is assumed and suppressed.

2.2.1 Source-Field Relationship

We need to establish a relationship between a source and the field radiated by the source so that the relationship can be used to formulate integral equations of electromagnetic problems. The source we have mentioned is not necessarily a physical source but it can also be a mathematically equivalent source. By considering two types of sources, the electric and magnetic current densities, we are able to express the radiating fields due to these current densities in a homogeneous medium by using the magnetic vector potential $\boldsymbol{A}$ and the electric vector potential $\boldsymbol{F}$. If the current densities are resided in a volume V, the magnetic and electric vector potentials are expressed as

$$\boldsymbol{A}(\boldsymbol{r}) = \mu \int_V \boldsymbol{J}_V(\boldsymbol{r}')G(\boldsymbol{r},\boldsymbol{r}')\ dV' \tag{2.1a}$$

$$\boldsymbol{F}(\boldsymbol{r}) = \epsilon \int_V \boldsymbol{K}_V(\boldsymbol{r}')G(\boldsymbol{r},\boldsymbol{r}')\ dV' \tag{2.1b}$$

where $\boldsymbol{J}_V$ and $\boldsymbol{M}_V$ denote the electric and magnetic volume current densities, respectively; while ϵ and μ are the permittivity and permeability of the homogeneous medium, respectively. The $G(\boldsymbol{r},\boldsymbol{r}')$ is the 3-D scalar Green's function

$$G(\boldsymbol{r},\boldsymbol{r}') = \frac{e^{-jk|\boldsymbol{r}-\boldsymbol{r}'|}}{4\pi|\boldsymbol{r}-\boldsymbol{r}'|}, \tag{2.2}$$

where $k = \omega\sqrt{\mu\epsilon}$ is the wavenumber and ω is the angular frequency. Primed coordinates $\boldsymbol{r}'$ are used to denote the points in the source region, and unprimed coordinates $\boldsymbol{r}$ denote the observation point. If the current densities are confined to a surface S, the magnetic and electric vector potentials are

$$\boldsymbol{A}(\boldsymbol{r}) = \mu \int_S \boldsymbol{J}_S(\boldsymbol{r}')G(\boldsymbol{r},\boldsymbol{r'})\, dS' \tag{2.3a}$$

$$\boldsymbol{F}(\boldsymbol{r}) = \epsilon \int_S \boldsymbol{K}_S(\boldsymbol{r}')G(\boldsymbol{r},\boldsymbol{r'})\, dS' \tag{2.3b}$$

where $\boldsymbol{J}_S$ and $\boldsymbol{M}_S$ are the electric and magnetic surface current densities, respectively.

The electric and magnetic fields can be then expressed in term of the vector potentials as

$$\boldsymbol{E} = -j\omega\boldsymbol{A} - \frac{j\omega}{k^2}\boldsymbol{\nabla}(\boldsymbol{\nabla}\cdot\boldsymbol{A}) - \frac{1}{\epsilon}\boldsymbol{\nabla}\times\boldsymbol{F} \tag{2.4a}$$

$$\boldsymbol{H} = \frac{1}{\mu}\boldsymbol{\nabla}\times\boldsymbol{A} - j\omega\boldsymbol{F} - \frac{j\omega}{k^2}\boldsymbol{\nabla}(\boldsymbol{\nabla}\cdot\boldsymbol{F}). \tag{2.4b}$$

By defining the following operators

$$\mathcal{L}\boldsymbol{X} = jk\int_\Omega \boldsymbol{X}G + \frac{1}{k^2}\boldsymbol{\nabla}\boldsymbol{\nabla}\cdot(\boldsymbol{X}G)\, d\Omega' \tag{2.5a}$$

$$\mathcal{M}\boldsymbol{X} = \boldsymbol{\nabla}\times\int_\Omega \boldsymbol{X}G\, d\Omega' \tag{2.5b}$$

with $\Omega = S$ or V, we can rewrite the electric and magnetic fields in a more compact form as

$$\boldsymbol{E} = -\eta\mathcal{L}\boldsymbol{J} - \mathcal{M}\boldsymbol{K} \tag{2.6a}$$

$$\boldsymbol{H} = \mathcal{M}\boldsymbol{J} - \frac{1}{\eta}\mathcal{L}\boldsymbol{K} \tag{2.6b}$$

where $\eta = \sqrt{\mu/\epsilon}$ is the intrinsic impedance.

We can also express the electric field using the mixed-potential form in which both vector and scalar potentials are used. In the mixed-potential form, the electric

field is given as

$$\boldsymbol{E} = -j\omega\mu\boldsymbol{A} - \boldsymbol{\nabla}\Phi - \boldsymbol{\nabla} \times \boldsymbol{F} \tag{2.7}$$

where the scalar potential

$$\Phi(\boldsymbol{r}) = \frac{j\eta}{k} \int_{\Omega} \rho_e(\boldsymbol{r}')g(\boldsymbol{r}, \boldsymbol{r}') \; d\Omega'. \tag{2.8}$$

The ρ_e denotes the electric charge density and it satisfies the continuity equation

$$\boldsymbol{\nabla} \cdot \boldsymbol{J}_{\Omega} = -j\omega\rho_e \tag{2.9}$$

2.2.2 Surface Equivalence Principle

It is possible that different kinds of source distributions outside a given region can produce the same field inside the region. Two sources producing the same field within a region of interest are said to be equivalent within that region. By using the surface equivalence principle (SEP), the sources inside a volume can be replaced with suitable electric and magnetic current densities flowing on the closed surface of the volume. It is a more rigorous formulation of the Huygen's principle, and it is based on the Uniqueness Theorem which requires either the tangential components of the electric field over the boundary, or the tangential components of the magnetic field over the boundary, or the former over part of the boundary and the latter over the rest of the boundary, to uniquely specify a field in a lossy region or lossless region [77, 78].

To derive the SEP, we first consider a closed surface S as shown in Fig. 2.1. The volume enclosed by S is denoted by V and outside S by V_{∞}. The current densities $\boldsymbol{J}$ and $\boldsymbol{K}$ are residing on S and are radiating in $V \cup V_{\infty}$. In Fig. 2.1(a), the current densities produce $\boldsymbol{E}_1$ and $\boldsymbol{H}_1$ throughout the V and V_{∞}. By using the boundary conditions, there exist no surface currents flowing on the surface S. In the Fig. 2.1(b), if the fields in V are allowed to be different from the V_{∞}, say, $\boldsymbol{E}_2$ and $\boldsymbol{H}_2$, then the surface current densities must exist to support the discontinuity.

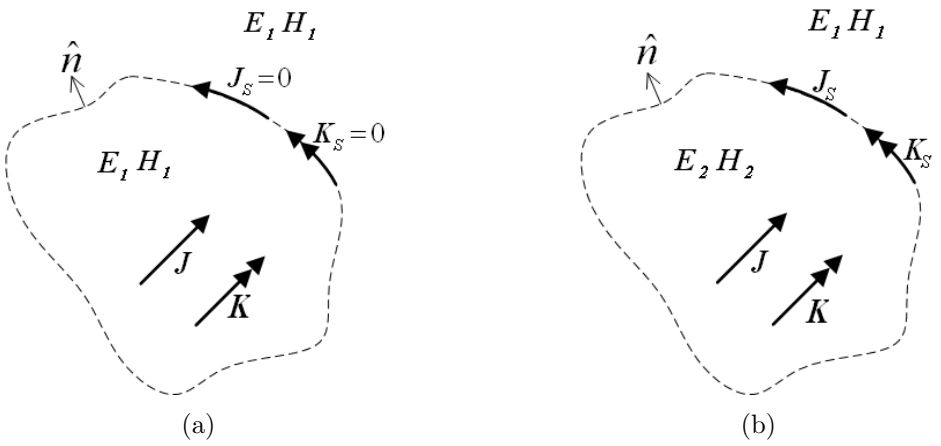

Figure 2.1: Surface Equivalence Principle. (a) Medium V same as medium V_∞. (b) Medium V different from medium V_∞

The surface electric and magnetic current densities are respectively defined as

$$\boldsymbol{J}_S = \hat{\boldsymbol{n}} \times (\boldsymbol{H}_1 - \boldsymbol{H}_2) \tag{2.10a}$$

$$\boldsymbol{K}_S = (\boldsymbol{E}_1 - \boldsymbol{E}_2) \times \hat{\boldsymbol{n}}, \tag{2.10b}$$

where the $\hat{\boldsymbol{n}}$ is the normal vector on the surface S pointing out of V. By using *Love's equivalence principle*, we let these equivalent surface current densities produce null fields in V, i.e. $\boldsymbol{E}_2 = 0$ and $\boldsymbol{H}_2 = 0$, and Eq. (2.10) becomes

$$\boldsymbol{J}_S = \hat{\boldsymbol{n}} \times \boldsymbol{H}_1 \tag{2.11a}$$

$$\boldsymbol{K}_S = \boldsymbol{E}_1 \times \hat{\boldsymbol{n}}. \tag{2.11b}$$

Now we assume that the volume V is source free and the entire volume $(V \cup V_\infty)$ is illuminated by incident waves $\boldsymbol{E}^{inc}$ and $\boldsymbol{H}^{inc}$, which are generated by impressed sources in medium V_∞. The fields in V_∞ are given by

$$\boldsymbol{E}_1 = \boldsymbol{E}^{inc} + \boldsymbol{E}^{sca} \tag{2.12a}$$

$$\boldsymbol{H}_1 = \boldsymbol{H}^{inc} + \boldsymbol{H}^{sca}, \tag{2.12b}$$

where $\boldsymbol{E}^{sca}$ and $\boldsymbol{H}^{sca}$ are the scattered fields produced by the equivalent current

densities given in Eq. (2.11). By using the source-field relationship that we obtain in Eq. (2.6), Eq. (2.12) can be written as

$$\boldsymbol{E}^{inc} - \eta_1 \mathcal{L}\boldsymbol{J}_S - \mathcal{M}\boldsymbol{K}_S = \begin{cases} \boldsymbol{E}_1(\boldsymbol{r}), & \boldsymbol{r} \in V_\infty \\ 0, & \boldsymbol{r} \in V; \end{cases} \tag{2.13}$$

$$\boldsymbol{H}^{inc} + \mathcal{M}\boldsymbol{J}_S - \frac{1}{\eta_1}\mathcal{L}\boldsymbol{K}_S = \begin{cases} \boldsymbol{H}_1(\boldsymbol{r}), & \boldsymbol{r} \in V_\infty \\ 0, & \boldsymbol{r} \in V. \end{cases} \tag{2.14}$$

By letting the $\boldsymbol{r}$ approach the artificial surface S and taking the cross product of $\widehat{\boldsymbol{n}}$ with Eqs. (2.13)–(2.14),

$$-\boldsymbol{K}_S + \widehat{\boldsymbol{n}} \times \eta_1 \mathcal{L}\boldsymbol{J}_S + \widehat{\boldsymbol{n}} \times \mathcal{M}\boldsymbol{K}_S = \widehat{\boldsymbol{n}} \times \boldsymbol{E}^{inc} \tag{2.15}$$

$$\boldsymbol{J}_S - \widehat{\boldsymbol{n}} \times \mathcal{M}\boldsymbol{J}_S + \widehat{\boldsymbol{n}} \times \frac{1}{\eta_1}\mathcal{L}\boldsymbol{K}_S = \widehat{\boldsymbol{n}} \times \boldsymbol{H}^{inc}. \tag{2.16}$$

Eqs. (2.15) and (2.16) are commonly known as electric field integral equation (EFIE) and magnetic field integral equation (MFIE), respectively. In general, Eqs. (2.15) and (2.16) belong to the class of surface integral equations (SIEs) as the unknown functions, $\boldsymbol{J}_S$ and $\boldsymbol{K}_S$, are distributed on the surface of a structure.

2.2.3 Volume Equivalence Principle

The volume equivalence principle (VEP) can be used to replace the inhomogeneous dielectric and magnetic materials present in electromagnetic problems with equivalent volume current densities. To derive the VEP, we consider a homogeneous background medium which is characterized by permeability μ_1 and permittivity ϵ_1 and contains primary sources $\boldsymbol{J}$ and $\boldsymbol{K}$. Let a region of inhomogeneity characterized by permittivity ϵ and permeability μ, both of which may be a function of position, presence in the space. The fields $\boldsymbol{E}$ and $\boldsymbol{H}$ in the vicinity of the inhomogeneity must satisfy Maxwell's equations

$$\boldsymbol{\nabla} \times \boldsymbol{E} = -j\omega\mu\boldsymbol{H} - \boldsymbol{K} \tag{2.17a}$$

$$\nabla \times \boldsymbol{H} = j\omega\epsilon\boldsymbol{E} + \boldsymbol{J}. \tag{2.17b}$$

By introducing the equivalent volume electric and magnetic current densities which are respectively defined as

$$\boldsymbol{K}_V = j\omega(\mu - \mu_1)\boldsymbol{H} \tag{2.18a}$$

$$\boldsymbol{J}_V = j\omega(\epsilon - \epsilon_1)\boldsymbol{E}, \tag{2.18b}$$

we can rewrite Eq. (2.17) as

$$\nabla \times \boldsymbol{E} = -j\omega\mu_1\boldsymbol{H} - \boldsymbol{K}_V - \boldsymbol{K} \tag{2.19a}$$

$$\nabla \times \boldsymbol{H} = j\omega\epsilon_1\boldsymbol{E} + \boldsymbol{J}_V + \boldsymbol{J}. \tag{2.19b}$$

If we denote the $\boldsymbol{E}^{inc}$ and $\boldsymbol{H}^{inc}$ as the fields generated by the primary sources in the absence of the inhomogeneity, then they satisfy the Maxwell's equations

$$\nabla \times \boldsymbol{E}^{inc} = -j\omega\mu_1\boldsymbol{H}^{inc} - \boldsymbol{K} \tag{2.20a}$$

$$\nabla \times \boldsymbol{H}^{inc} = j\omega\epsilon_1\boldsymbol{E}^{inc} + \boldsymbol{J}. \tag{2.20b}$$

Hence the scattered fields $\boldsymbol{E}^{sca}$ and $\boldsymbol{H}^{sca}$, i.e. the differences between the fields $\boldsymbol{E}$ and $\boldsymbol{E}^{inc}$, and $\boldsymbol{H}$ and $\boldsymbol{H}^{inc}$, will satisfy

$$\nabla \times \boldsymbol{E}^{sca} = -j\omega\mu_1\boldsymbol{H}^{sca} - \boldsymbol{K}_V \tag{2.21a}$$

$$\nabla \times \boldsymbol{H}^{sca} = j\omega\epsilon_1\boldsymbol{E}^{sca} + \boldsymbol{J}_V. \tag{2.21b}$$

The equivalent volume current densities have replaced the inhomogeneity and they only exist within the inhomogeneity. Since the inhomogeneity has been removed, hence these equivalent volume current densities are radiating in the homogeneous background medium.

By using Eq. (2.6), the total fields $\boldsymbol{E}$ and $\boldsymbol{H}$ can be expressed as

$$\boldsymbol{E} = \boldsymbol{E}^{inc} - \eta_1 \mathcal{L}\boldsymbol{J}_V - \mathcal{M}\boldsymbol{K}_V \tag{2.22}$$

$$\boldsymbol{H} = \boldsymbol{H}^{inc} + \mathcal{M}\boldsymbol{J}_V - \frac{1}{\eta_1}\mathcal{L}\boldsymbol{K}_V. \tag{2.23}$$

Substituting Eq. (2.18) into these equations, we obtain

$$\frac{j}{\omega(\epsilon - \epsilon_1)}\boldsymbol{J}_V - \eta_1 \mathcal{L}\boldsymbol{J}_V - \mathcal{M}\boldsymbol{K}_V = \boldsymbol{E}^{inc} \tag{2.24}$$

$$\frac{j}{\omega(\mu - \mu_1)}\boldsymbol{K}_V + \mathcal{M}\boldsymbol{J}_V - \frac{1}{\eta_1}\mathcal{L}\boldsymbol{K}_V = \boldsymbol{H}^{inc}. \tag{2.25}$$

In general, Eqs. (2.25) and (2.24) belong to the class of volume integral equations (VIEs) as the unknown functions $\boldsymbol{J}_V$ and $\boldsymbol{K}_V$ are distributed over the volume of a material object.

2.3 Method of Moments

The MoM is a numerical method for solving boundary-value problems in electromagnetics [11]. The principal idea of MoM is to reduce a functional equation into a matrix equation, and then solve the matrix equation on a computer. To illustrate the MoM's procedures, we consider the inhomogeneous equation

$$Lf = g \tag{2.26}$$

where L is a linear operator, f is the unknown function to be determined, and g is the known source or excitation. It is assumed that the solution to Eq. (2.26) is unique; that is, only one f is associated with a given g. Let $\tilde{f}$ be the approximate solution of Eq. (2.26) and can be expanded in a series of known functions $f_1, f_2, ..., f_N$ in the domain of L, as follows:

$$f \simeq \tilde{f} = \sum_{n=1}^{N} c_n f_n \tag{2.27}$$

where the c_n denote the unknown expansion coefficients to be determined. The f_n is normally referred as basis function or expansion function. For an exact solution, the N in Eq. (2.27) should be infinite. However for a practical problem, the solution f is normally approximated by a finite value of N. Since the $\tilde{f}$ is an approximate solution to Eq. (2.26), we can define the non-zero residual,

$$r = L\widetilde{f} - Lf = \sum_{n=1}^{N} c_n L f_n - g, \tag{2.28}$$

where the linearity of L is used. The residual is then forced to be orthogonal with a set functions, $t_1, t_2, ..., t_N$. And using the inner product, which is defined as

$$\langle a, b \rangle = \int a \cdot b^* \; d\Omega, \tag{2.29}$$

the above criteria can be expressed as

$$\langle t_m, r \rangle = 0, \qquad\qquad m = 1, 2, ..., N. \tag{2.30}$$

The t_m is known as testing function or weighting function. If the Galerkin's testing procedure is used, then the testing functions are chosen to be the same as the basis functions. Substituting Eq. (2.28) into Eq. (2.30), we obtain

$$\sum_{n=1}^{N} c_n \langle t_m, L f_n \rangle = \langle t_m, g \rangle, \quad m = 1, 2, ..., N; \tag{2.31}$$

or in matrix form

$$\overline{\boldsymbol{A}}\boldsymbol{x} = \boldsymbol{b} \tag{2.32}$$

where

$$\overline{\boldsymbol{A}} = \begin{pmatrix} \langle t_1, L f_1 \rangle & \cdots & \langle t_1, L f_N \rangle \\ \vdots & \ddots & \vdots \\ \langle t_N, L f_1 \rangle & \cdots & \langle t_N, L f_N \rangle \end{pmatrix} \tag{2.33}$$

$$\boldsymbol{x} = \begin{pmatrix} c_1 \\ \vdots \\ c_N \end{pmatrix}, \tag{2.34}$$

and

$$\boldsymbol{b} = \begin{pmatrix} \langle t_1, g \rangle \\ \vdots \\ \langle t_N, g \rangle \end{pmatrix}. \tag{2.35}$$

If the $\overline{\boldsymbol{A}}$ is a nonsingular matrix, then $\overline{\boldsymbol{A}}^{-1}$ exists. The $\boldsymbol{x}$ can be obtained by

$$\boldsymbol{x} = \overline{\boldsymbol{A}}^{-1}\boldsymbol{b} \tag{2.36}$$

and the solution to $\widetilde{f}$ can be obtained from Eq. (2.26). It is noted that the f_n should be linearly independent and be chosen such that the $\widetilde{f}$ can approximate f reasonably well.

In order to apply the MoM to solve the electromagnetic problems, the geometry of the scatterer is modeled using simple polygons. For surface scatterer, it is common to model the surface using triangular or quadrilateral patches. For volume scatterer, polygons such as tetrahedrons and cubes have been used. When modeling an arbitrarily shaped object, it is advantageous to use triangular patches for surface scatterer and tetrahedron cells for volume scatterer. Planar triangular patches have been widely used to model the geometry of the object. Curved triangular patches have also been used with the aim of reducing modeling error but additional processing time and memory are needed to process the curved geometry and the associated basis functions.

The basis functions can be mainly categorized into two types, entire domain basis functions and subdomain basis functions. The entire domain basis functions, as the name suggests, are defined on the entire computational domain. Using these basis functions to expand the unknown functions is analogous to a Fourier expansion or to a modal expansion. These types of functions yield a good convergence

of the method but are not versatile since the geometry needs to be regular in order to have the modes defined. It is not practical to apply the entire domain basis functions to solve 3-D problems but it does deliver good results in solving one-dimensional problems [79].

By dividing the computational domain into smaller subdomains, the subdomain basis functions are defined on each of the subdomains. The subdomain basis functions are relied on the proper meshing of the geometry, which can be triangular and rectangular (for surface scatterer), or tetrahedron and hexahedron (for volume scatterer). The term "elements" is used to denote a general type of subdomain, e.g. a wire segment, a surface patch, or a volumetric cell. For surfaces, we refer the subdomains as patches while for volumes, we call it cells. The subdomain basis functions are widely used in solving 3-D problems.

When using subdomain basis functions, it is also preferable that the basis functions are divergence-conforming. The divergence-conforming basis functions have been used to discretize the unknown equivalent current densities in solving electromagnetic scattering problems using the MoM. The divergence-conforming basis functions impose normal continuity of a vector quantity between neighboring elements and the enforced continuity avoids buildup of line charges at the boundary between adjacent patches.

In this thesis, the geometry of the scatterer will be discretized using triangular patches (for surface scatterer) and tetrahedron cells (for volume scatterer). In the following subsection, we will discuss the suitable divergence-conforming subdomain basis functions for triangular patches and tetrahedron cells.

2.3.1 Basis Functions For Planar Triangular Patches

Rao-Wilton-Glisson (RWG) basis functions [21] have been widely used as the basis functions for planar triangular patches. These surface vector basis functions are commonly used to expand the unknown surface current density of the surface inte-

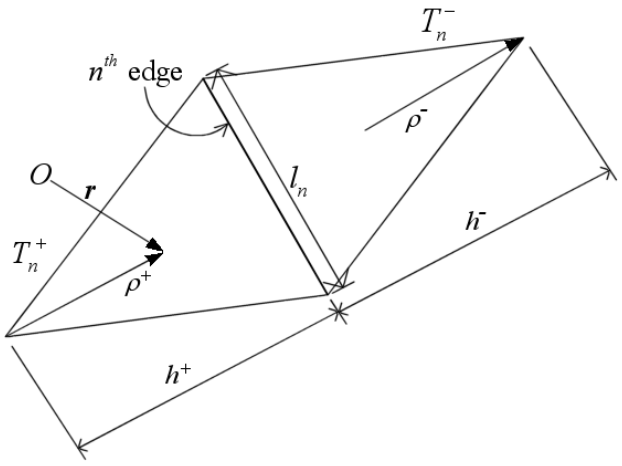

Figure 2.2: A Rao-Wilton-Glisson (RWG) basis function

gral equations. The RWG basis functions are derived from the famous rooftop basis functions which are defined on rectangular patches [20]. A RWG basis function is defined on the common edge of a pair of triangular patches as

$$\boldsymbol{f}_n(\boldsymbol{r}) = \begin{cases} \dfrac{l_n}{2A_n^+}\boldsymbol{\rho}_n^+, & \boldsymbol{r} \text{ in } T_n^+ \\ \dfrac{l_n}{2A_n^-}\boldsymbol{\rho}_n^-, & \boldsymbol{r} \text{ in } T_n^- \\ 0, & \text{otherwise} \end{cases}, \tag{2.37}$$

where l_n is the length of the n^{th} edge, $A^{\pm}$ represents the area of the triangles $T^{\pm}$, and $\boldsymbol{\rho}^+$ and $\boldsymbol{\rho}^-$ are vectors pointing away and toward the free vertex. An example of RWG basis functions is shown in Fig. 2.2. On every patch, only a maximum of three basis functions will exist, corresponding to the three edges. If any of the edges is used to define an open structure, then no basis functions will be defined on it.

Some of the features of these vector basis functions include those below.

- The $\boldsymbol{f}_n$ has no component normal to the boundary edges (excludes the common edge) of the surface formed by triangle pair T^+ and T^- and hence no line charges exist along the boundary edges.

- Constant normal component on the common edge because the normal com-

ponent of $\rho_n^{\pm}$ is just the height h of $T_n^{\pm}$ with n^{th} edge as the base. The $\rho_n^{\pm}$ is normalized by the h such that f_n normal to the n^{th} edge is unity. This has ensured the continuity of current density normal to the edge.

- The surface divergence of $\boldsymbol{f}_n$,

$$\boldsymbol{\nabla}_S \cdot \boldsymbol{f}_n = \pm \frac{1}{\rho_n^{\pm}} \frac{\partial}{\partial \rho_n^{\pm}} \left(\rho_n^{\pm} \frac{l_n}{2A_n^{\pm}} \rho_n^{\pm} \right) = \begin{cases} \dfrac{l_n}{A_n^+}, & \boldsymbol{r} \text{ in } T_n^+ \\ -\dfrac{l_n}{A_n^-}, & \boldsymbol{r} \text{ in } T_n^- \\ 0, & \text{otherwise.} \end{cases} \tag{2.38}$$

  The surface charge density is related to the $\boldsymbol{\nabla}_S \cdot \boldsymbol{f}_n$ through Eq. (2.9). Hence the charge density within each triangular patch is constant and the total charge associated with the triangle pair $T_n^{\pm}$ is zero.

In using the RWG basis function to solve the EFIE, Rao et. al. have applied the approximate Galerkin's procedure where the integral equation is tested at the centroid of the patches [21]. This method has been adopted in our implementation.

2.3.2 Basis Functions For Curved Triangular Patches

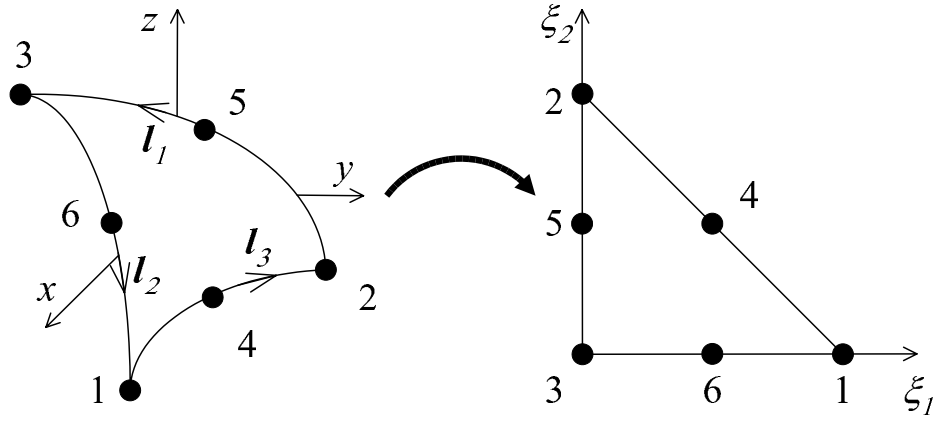

Figure 2.3: Mapping a curved triangular patch in $\boldsymbol{r}$ space (x, y, z) into $\boldsymbol{\xi}$ space (ξ_1, ξ_2).

In order to minimize the modeling error, the geometry of the scatterer is modeled using curved triangular patches. By using the second-order parametric trans-

formation, a curved triangular patch with six nodes can be mapped onto a planar right-angle triangular patch using the transformation [69]

$$\boldsymbol{r} = \sum_{i=1}^{6} L_i\left(\xi_1, \xi_2, \xi_3\right) \boldsymbol{r}_i, \tag{2.39}$$

where ξ_1, ξ_2 and ξ_3 are parametric coordinates and they satisfy the relation of $\xi_1 + \xi_2 + \xi_3 = 1$. The shape functions L_i $(i = 1, \cdots, 6)$ are given as

$$\begin{aligned} L_i &= \xi_i(2\xi_i - 1), \quad i = 1, 2, 3 \\ L_4 &= 4\xi_1\xi_2, \\ L_5 &= 4\xi_2\xi_3, \\ L_6 &= 4\xi_3\xi_1. \end{aligned} \tag{2.40}$$

The divergence-conforming basis functions $\boldsymbol{\Lambda}_n$ defined on the curvilinear triangular patches are given by [80] as

$$\boldsymbol{\Lambda}_\beta = \frac{|\boldsymbol{l}_\beta|}{\mathcal{J}}\left(\xi_{\beta+1}\boldsymbol{l}_{\beta-1} - \xi_{\beta-1}\boldsymbol{l}_{\beta+1}\right), \qquad \beta = 1, 2, 3 \tag{2.41}$$

where the indexing is performed in modulus of three and the Jacobian is defined as

$$\mathcal{J} = \widehat{n} \cdot \frac{\partial \boldsymbol{r}}{\partial \xi_1} \times \frac{\partial \boldsymbol{r}}{\partial \xi_2}. \tag{2.42}$$

The edge vectors, $\boldsymbol{l}_1$, $\boldsymbol{l}_2$ and $\boldsymbol{l}_3$, are shown in Fig. 2.3 and they are defined as

$$\begin{aligned} \boldsymbol{l}_1 &= -\frac{\partial \boldsymbol{r}}{\partial \xi_2}, \\ \boldsymbol{l}_2 &= \frac{\partial \boldsymbol{r}}{\partial \xi_1}, \\ \boldsymbol{l}_3 &= \frac{\partial \boldsymbol{r}}{\partial \xi_2} - \frac{\partial \boldsymbol{r}}{\partial \xi_1}. \end{aligned} \tag{2.43}$$

It is noted that an adjustment of sign is necessary to ensure the continuity of the normal components across adjacent elements.

2.3.3 Basis Functions For Tetrahedron Cells

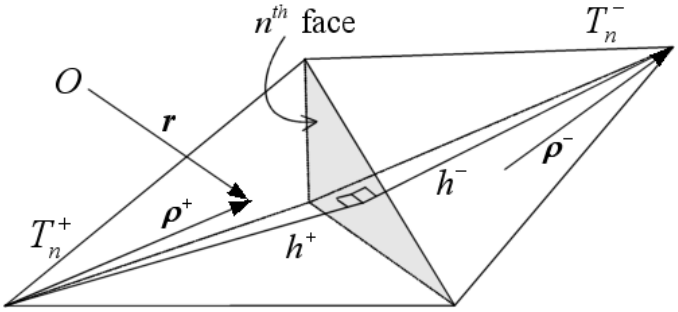

Figure 2.4: A Schaubert-Wilton-Glisson (SWG) basis function

The divergence-conforming vector basis functions for tetrahedron cells were introduced by Schaubert, Wilton and Glisson [29]. These vector basis functions can be considered as the 3-D extension of the 2-D surface vector basis functions [20, 21]. The Schaubert-Wilton-Glisson (SWG) basis functions have been used to expand the unknown electric flux density of the volume integral equation. A SWG basis function is defined on the common face of a pair of tetrahedron cells as shown below

$$\boldsymbol{f}_n(\boldsymbol{r}) = \begin{cases} \dfrac{A_n}{3V_n^+}\boldsymbol{\rho}_n^+, & \boldsymbol{r} \text{ in } T_n^+ \\ \dfrac{A_n}{3V_n^-}\boldsymbol{\rho}_n^-, & \boldsymbol{r} \text{ in } T_n^- \\ 0, & \text{otherwise} \end{cases} \tag{2.44}$$

where A_n is the area of the n^{th} face, $V^{\pm}$ represents the volume of the tetrahedron $T^{\pm}$, and $\boldsymbol{\rho}^+$ and $\boldsymbol{\rho}^-$ are vectors pointing away and toward the free vertex. An example of SWG basis functions is shown in Fig. 2.4. On every tetrahedral cell, only a maximum of four basis functions will exist, corresponding to the four faces of the cell. If any of the faces is used as the interface between the background medium and dielectric material, then a half basis function will be defined on it. A half SWG basis function is having zero height in one of the tetrahedron cells.

The features of these 3-D vector basis functions include:

- The $\boldsymbol{f}_n$ has no component normal to the boundary surfaces (excludes the common surface) of the volume formed by a tetrahedron pair T^+ and T^-.

- Constant normal component on the common surface because the normal component of $\rho_n^{\pm}$ is just the height h of $T_n^{\pm}$ with n^{th} face as the base. The $\rho_n^{\pm}$ is normalized by the h such that f_n normal to the n^{th} face is unity. This has ensured the continuity of electric flux density normal to the face.

- The divergence of $\boldsymbol{f}_n$,

$$\boldsymbol{\nabla} \cdot \boldsymbol{f}_n = \pm \frac{1}{(\rho_n^{\pm})^2} \frac{\partial}{\partial \rho_n^{\pm}} \left((\rho_n^{\pm})^2 \frac{A_n}{3V_n^{+}} \rho_n^{\pm} \right) = \begin{cases} \dfrac{A_n}{V_n^{+}}, & \boldsymbol{r} \text{ in } T_n^{+} \\ -\dfrac{A_n}{V_n^{-}}, & \boldsymbol{r} \text{ in } T_n^{-} \\ 0, & \text{otherwise.} \end{cases} \tag{2.45}$$

  The charge density in the cell is proportional to $\boldsymbol{\nabla} \cdot \boldsymbol{f}_n$ through Eqs. (2.9) and (2.18b). Hence the charge density within each tetrahedron is constant.

Schaubert et. al. have used the SWG basis functions to solve the electromagnetic scattering by dielectric scatterers formulated by volume EFIE [29]. They have applied approximate Galerkin's procedure where the integral equation is tested at the centroid of the tetrahedral cells.

Chapter 3

Adaptive Integral Method – A Fast Algorithm for Computational Electromagnetics

3.1 Introduction

The matrix equation generated by the conventional MoM can be solved by either a direct solver or an iterative solver. Direct solvers such as Gaussian elimination and lower-upper decomposition (LUD) methods have the computational complexity and storage requirement of $O(N^3)$ and $O(N^2)$, respectively. Alternatively, the matrix equation can be solved by iterative solvers such as Gauss-Seidal and conjugate gradient (CG) methods. All iterative solvers need to perform matrix-vector multiplication which requires $O(N^2)$ operations. Hence the total computation cost of an iterative solver is proportional to $O(N_{iter}N^2)$, where N_{iter} is the number of iterations and it is normally much smaller than N. The storage requirement for the iterative solver is also of $O(N^2)$. The computational complexity and storage requirement of the conventional MoM have made it prohibitively expensive to solve large-scale electromagnetic problems.

Adaptive Integral Method (AIM) is a grid based fast algorithm introduced by Bleszynski et. al. [47, 48] to overcome the weakness of the conjugate gradient-fast Fourier transform (CG-FFT) method. It has been successfully implemented in solving various large-scale electromagnetic problems [49–57]. It is implemented in the iterative solver to accelerate matrix-vector multiplication and to compress the dense impedance matrix in order to reduce the matrix storage requirement. Unlike the CG-FFT method, AIM can be applied to deal with arbitrarily shaped objects. In principle, the AIM can be applied to solve the problems which exhibit convolutional property. In this chapter, we will first explain the basis idea and follow by the detailed description of AIM in solving electromagnetic scattering problems. Next, the accuracy of the AIM will be examined and then the complexity of the AIM will also be investigated.

3.2 Basic Ideas

AIM accomplishes the reduction in computational complexity and matrix storage requirement by computing the far-zone interaction using a more effective method. The method is based on the physical considerations that the fields at a distance far away from the sources can be computed by using reduced amount of information on the source current distribution. Hence by satisfying certain criterion, the potentials at observation points distant away from a source currents distribution can be computed using a small number of weighted point sources. If the grid currents all lie on a uniform grid, then the computation of the potentials at the grid points due to grid currents is a discrete convolution which can be computed efficiently using the FFT.

In following the idea, thus the matrix vector multiplication, $\overline{\boldsymbol{Z}}\boldsymbol{I}$, can be accelerated using the following procedure of

1. projecting the basis function to the surrounding grid points,

2. computing the far-zone interaction or potentials using the fast Fourier trans-

form (FFT),

3. interpolating the potentials back to the basis functions, and

4. directly computing the near-zone interaction.

This process is summarized in Fig. 3.1.

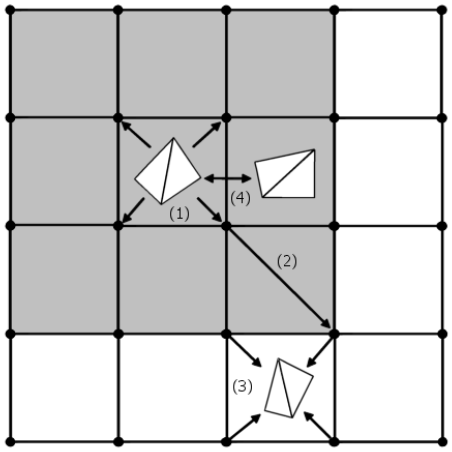

Figure 3.1: Pictorial representation of AIM to accelerate the matrix-vector multiplication. Near-zone interaction (within the grey area) are computed directly, while far-zone interaction are computed using the grids.

The AIM splits the matrix-vector multiplication into two parts, i.e. near-zone interaction and far-zone interaction, and mathematically

$$\overline{\boldsymbol{Z}}\boldsymbol{I} = \overline{\boldsymbol{Z}}^{\text{near}}\boldsymbol{I} + \overline{\boldsymbol{Z}}^{\text{far}}\boldsymbol{I} \tag{3.1}$$

where $\overline{\boldsymbol{Z}}^{\text{near}}$ denotes the near-zone interaction among the nearby elements within a threshold distance and $\overline{\boldsymbol{Z}}^{\text{far}}$ represents the far-zone interaction of the elements.

3.3 Detailed Description

The geometry of an arbitrarily shaped object has prevented the direct use of FFT to compute the convolution in the operators $\mathcal{L}$ and $\mathcal{M}$. In order to utilize FFT to

evaluate the convolution, it is imperative to transform or project the basis functions to the uniform rectangular grids.

We first enclose the arbitrarily shaped object in a rectangular region and then recursively subdivides it into a total of W small rectangular *cells* with every cell contains $(M+1)^3$ points. Fig. 3.2 illustrates two elements enclosed by cells with $(M+1)^3 = 27$ and $(M+1)^3 = 64$ grids, respectively. Each of the elements will only be assigned to one cell and we denote the $N_{cell}(p)$ as the total number of basis functions bounded by the p-th cell. The current density on each element will be projected to the grid points of its associated cell. If we denote $\gamma_n(\boldsymbol{r})$ to represent

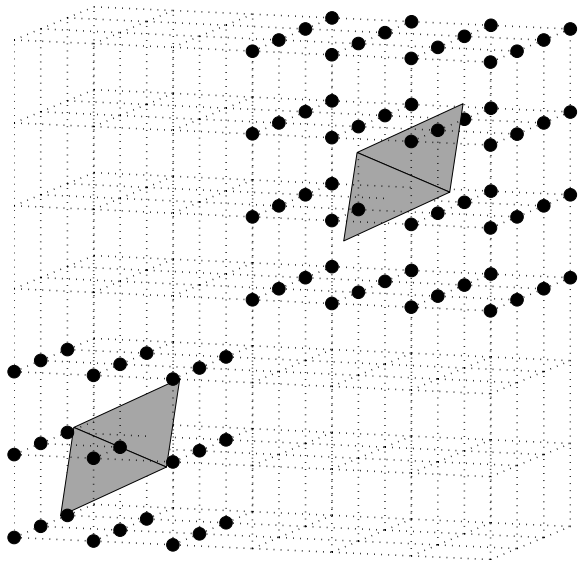

Figure 3.2: Projection of RWG basis functions to surrounding rectangular grids. The highlighted triangular basis function on the left is approximated by $(M+1)^3 = 27$ rectangular. The highlighted triangular basis function on the right is approximated by $(M+1)^3 = 64$.

any one the components of $\boldsymbol{f}_n$ and its derivatives ($\boldsymbol{\nabla}\cdot\boldsymbol{f}_n$ and $\boldsymbol{\nabla}\times\boldsymbol{f}_n$), we note that all the matrix elements discussed in Chapter 2 can be expressed in the following unified form

$$Z_{mn} = \int_{\Omega_m}\int_{\Omega_n} \gamma_m(\boldsymbol{r})\; G(\boldsymbol{r},\boldsymbol{r}')\; \gamma_n(\boldsymbol{r})\; d\Omega'\; d\Omega. \tag{3.2}$$

The transformation function, $\gamma_n(\boldsymbol{r})$ can be approximated as a linear combination

of Dirac delta functions,

$$\gamma_n(\boldsymbol{r}) \simeq \widehat{\gamma}_n(\boldsymbol{r}) = \sum_{u=1}^{(M+1)^3} \Lambda_{nu}\delta(\boldsymbol{r}-\boldsymbol{r}') \tag{3.3}$$

where M is the expansion order and Λ_{nu} denote the expansion coefficients of $\widehat{\gamma}_n(\boldsymbol{r})$. Λ_{nu} can be determined by using the multipole expansion which is based on the criterion that the coefficients Λ_{nu} produce the same multipole moments of the original basis function [48]. The expansion coefficients can be calculated using the following equation:

$$\begin{aligned}&\int_{\alpha_n} \gamma_n(\boldsymbol{r})(x-x_0)^{m1}(y-y_0)^{m2}(z-z_0)^{m3}\, dr \\ &= \sum_{u=1}^{(M+1)^3} (x_{nu}-x_0)^{m1}(y_{nu}-y_0)^{m2}(z_{nu}-z_0)^{m3}\Lambda_{nu}, \\ &\qquad\qquad \text{for } 0 \le \{m1, m2, m3\} \le M\end{aligned} \tag{3.4}$$

where the reference point $\boldsymbol{r}_0 = (x_0, y_0, z_0)$ is chosen as the center of the basis function. However the choice of the reference point is irrelevant as the expansion in Eq. (3.4) is valid for other points.

Once the transformation function has been determined, the matrix elements can be approximated as

$$Z_{mn} \simeq \widehat{Z}_{mn} = \sum_{v=1}^{(M+1)^3}\sum_{u=1}^{(M+1)^3} \Lambda_{mv} G(\boldsymbol{r}_v, \boldsymbol{r}'_u)\Lambda_{nu} \tag{3.5}$$

and the far-zone interaction of the matrix-vector multiplication in Eq. (3.1) can be written as

$$\overline{\boldsymbol{Z}}^{\text{far}} = \overline{\boldsymbol{\Lambda}}\ \overline{\boldsymbol{G}}\ \overline{\boldsymbol{\Lambda}}^T. \tag{3.6}$$

The $\overline{\boldsymbol{\Lambda}}$ represents the sparse basis transformation matrix of the elements which contains at most $(M+1)^3$ non-zero elements in every row. The $\overline{\boldsymbol{G}}$ is the Toeplitz matrix whose elements are the free-space Green's function evaluated at grid points. The Toeplitz property has enabled the use of FFT to compute the matrix-vector

multiplication efficiently. Hence we can represent the far-zone interaction by

$$\overline{\boldsymbol{Z}}^{\text{far}}\boldsymbol{I} = \overline{\boldsymbol{\Lambda}}\mathcal{F}^{-1}\left\{\mathcal{F}\left\{\overline{\boldsymbol{G}}\right\}\cdot\mathcal{F}\left\{\overline{\boldsymbol{\Lambda}}^{T}\boldsymbol{I}\right\}\right\} \tag{3.7}$$

where $\mathcal{F}\{\bullet\}$ and $\mathcal{F}^{-1}\{\bullet\}$ are the FFT and the inverse FFT, respectively.

The $\overline{\boldsymbol{Z}}^{\text{far}}$ has provided good approximation for the interaction among the elements that are far apart, but the grid currents cannot accurately approximate the near-zone interaction. However, we have included the inaccurate approximation of the near-zone interaction in Eq. (3.6). Hence the inaccurate contribution from grid currents needs to be removed from the near-zone interactions. The $\overline{\boldsymbol{Z}}^{\text{near}}$ can be constructed such that the inaccurate contribution from $\overline{\boldsymbol{Z}}^{\text{far}}$ will be removed and replaced with correct contribution. The elements of $\overline{\boldsymbol{Z}}^{\text{near}}$ can be computed with

$$Z_{mn}^{\text{near}} = \begin{cases} Z_{mn} - \widehat{Z}_{mn}, & \text{if } d_{mn} \leq d_{near} \\ 0, & \text{otherwise,} \end{cases} \tag{3.8}$$

where d_{mn} is the distance between the element m and n, and d_{near} is the near-zone range. Since an element has only a limited number of nearby neighbor elements, $\overline{\boldsymbol{Z}}^{\text{near}}$ is a sparse matrix.

By using the $\overline{\boldsymbol{Z}}^{\text{far}}$ and $\overline{\boldsymbol{Z}}^{\text{near}}$ obtained in Eqs. (3.7) and (3.8), the matrix-vector multiplication in (3.1) can be represented as

$$\overline{\boldsymbol{Z}}\boldsymbol{I} = \overline{\boldsymbol{Z}}^{\text{near}}\boldsymbol{I} + \overline{\boldsymbol{\Lambda}}\mathcal{F}^{-1}\left\{\mathcal{F}\left\{\overline{\boldsymbol{G}}\right\}\cdot\mathcal{F}\left\{\overline{\boldsymbol{\Lambda}}^{T}\boldsymbol{I}\right\}\right\}. \tag{3.9}$$

3.4 Accuracy and Complexity of the AIM

In order to investigate the accuracy of the AIM to approximate the far-zone interaction, a simple experiment has been conducted. Fig. 3.3 shows an infinitesimal thin ring used in this experiment where the surface of the ring is modeled using triangular patches. The radius of the ring is 3λ and the length of the isosceles

triangle is 0.071λ. The RWG basis functions have been used to expand the surface currents and to discretize the integral equation. By defining the relative error between matrix element Z_{mn} and the approximation $\widehat{Z}_{mn}$ as

$$\triangle Z_{mn} = \frac{|Z_{mn} - \widehat{Z}_{mn}|}{|Z_{mn}|}, \tag{3.10}$$

we compute the $\triangle Z_{mn}$ for the operators $\mathcal{L}$ and $\mathcal{M}$ discussed in Chapter 2. The $\triangle Z_{mn}$ is plotted as a function of the arc distance between elements for different expansion orders and grid sizes are shown in Fig. 3.4 and Fig. 3.5.

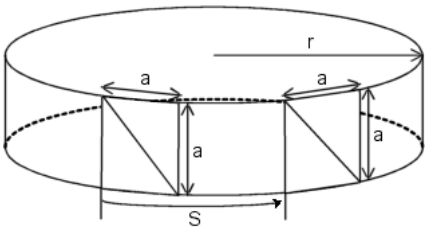

Figure 3.3: Experiment setup for the accuracy of AIM. The ring has a radius of 3λ and it is divided into 704 segments with $a = 0.071\lambda$

In both Fig. 3.4 and Fig. 3.5, we observe that the $\widehat{Z}_{mn}$ offers a good approximation to Z_{mn} when the current sources are far apart. The results also show that the expansion orders $M = 2$ and $M = 3$ produce approximation with a relative error $\leq 1\%$. The expansion $M = 3$ gives the best approximation however it also requires more CPU time and more storage compared to expansion $M = 2$. Throughout this thesis, we will use the expansion order $M = 2$ as the accuracy of 1% error is good enough for engineering applications. Besides, we also like to reserve the scarce computing resources for other purposes.

Now we will investigate the computational complexity and storage requirement of our AIM implementation. We will first consider the complexity of our AIM implementation in solving the surface integral equation (SIE). The matrix storage requirement and CPU time for matrix filling and matrix-vector multiplication are plotted in Fig. 3.6 and Fig. 3.7, respectively.

The asymptotic computational complexity and matrix storage requirement of

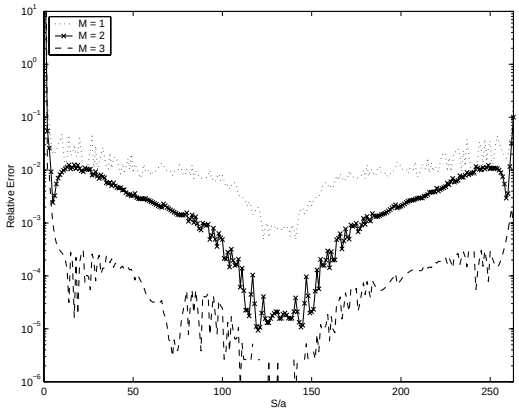

(a) Grid size = 0.01λ

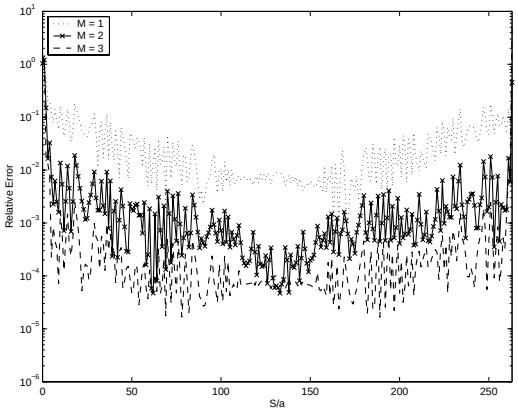

(b) Grid size = 0.03λ

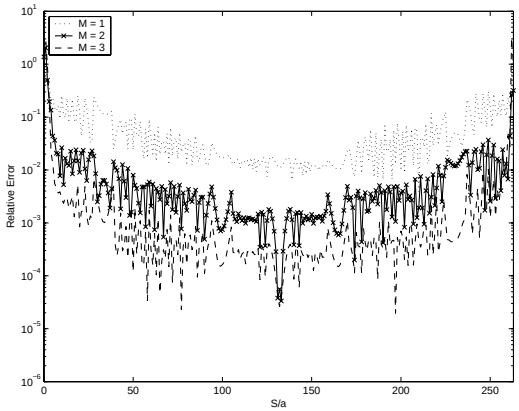

(c) Grid size = 0.05λ

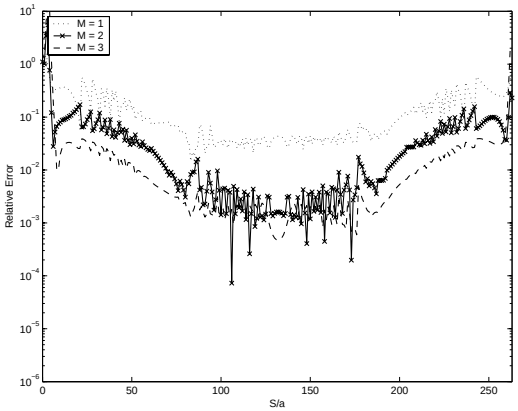

(d) Grid size = 0.07λ

Figure 3.4: The relative error of AIM for matrix elements of operator $\mathcal{L}$ using different expansion orders (M = 1, 2 and 3) and grid sizes.

AIM in solving SIE have been given by [48] without proof as of $O(N^{1.5})$ and $O(N^{1.5}\log N)$, respectively. In our implementation on a PC, the AIM exhibits $O(N^{1.15})$, $O(N)$ and $O(N^{1.5}\log N)$ patterns for the matrix storage, matrix filling times and matrix vector multiplication, respectively. The difference between our AIM implementation and the estimation given in [48] are most likely due to the size of the triangular patches being used, which is highly dependent on the mesher. In addition, the geometry of the structure will also produce different patterns and in this example, we have used a metallic sphere.

Next, we consider the complexity of our AIM implementation in solving the

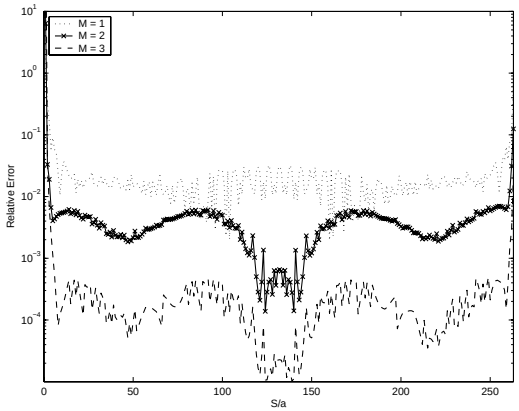

(a) Grid size = 0.01λ

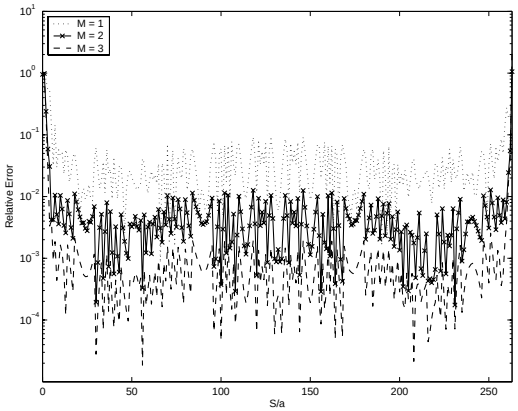

(b) Grid size = 0.03λ

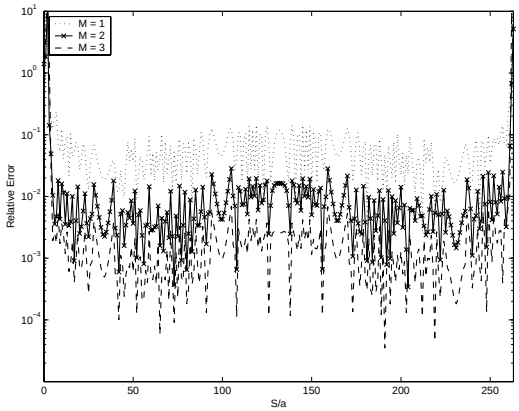

(c) Grid size = 0.05λ

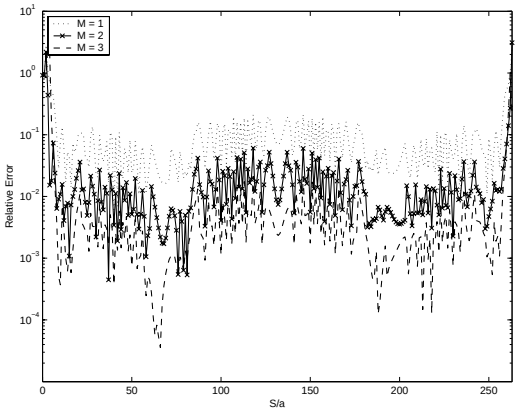

(d) Grid size = 0.07λ

Figure 3.5: The relative error of AIM for matrix elements of operator $\mathcal{M}$ using different expansion orders (M = 1, 2 and 3) and grid sizes.

volume integral equation (VIE). The matrix storage requirement and CPU time for matrix filling and matrix-vector multiplication are plotted in Fig. 3.8 and Fig. 3.9, respectively.

The asymptotic computational complexity and matrix storage requirement of AIM in solving VIE have been estimated as of $O(N)$ and $O(N \log N)$, respectively [48]. In our AIM implementation on PC, the matrix storage, matrix fill times and matrix-vector multiplication have exhibited $O(N^{1.2} \log N)$, $O(N^{1.2} \log N)$ and $O(N \log N)$, respectively. The difference between the our results with the estimation are most probably due to the sizes of the tetrahedron cells, which are highly

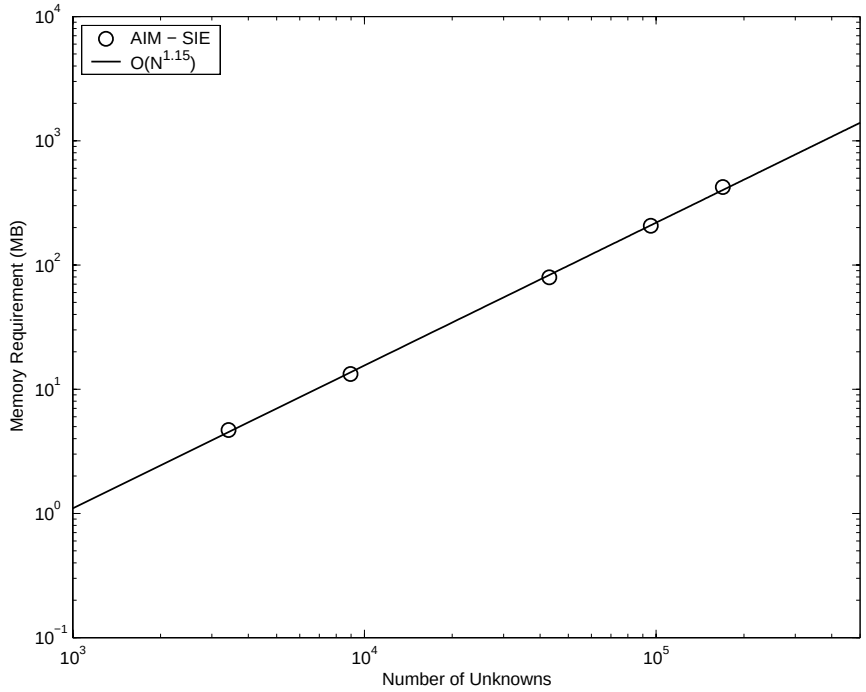

Figure 3.6: AIM memory requirement versus the number of unknowns for the surface integral equation.

dependent on the mesher being used. In this example, our test object is a dielectric sphere which is discretized by using the GiD [81].

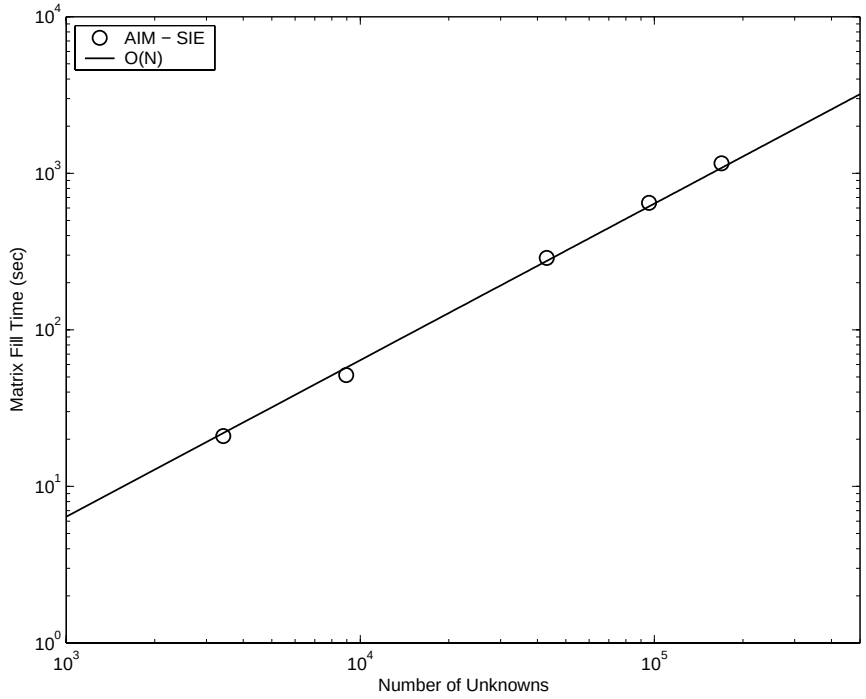

(a) Matrix filling

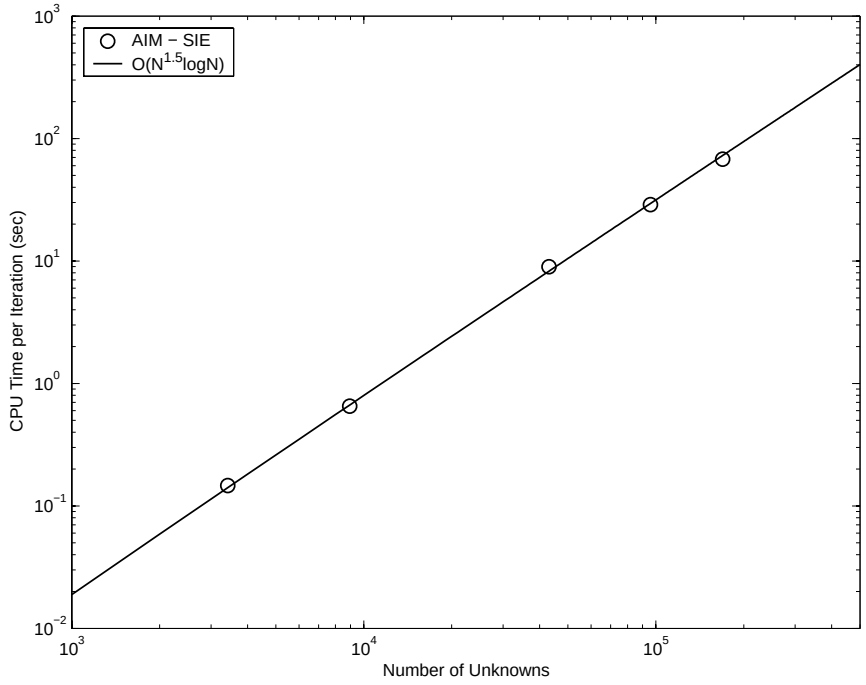

(b) Matrix-vector multiplication

Figure 3.7: AIM CPU time versus the number of unknowns for the surface integral equation. (a) Matrix filling. (b) Matrix-vector multiplication.

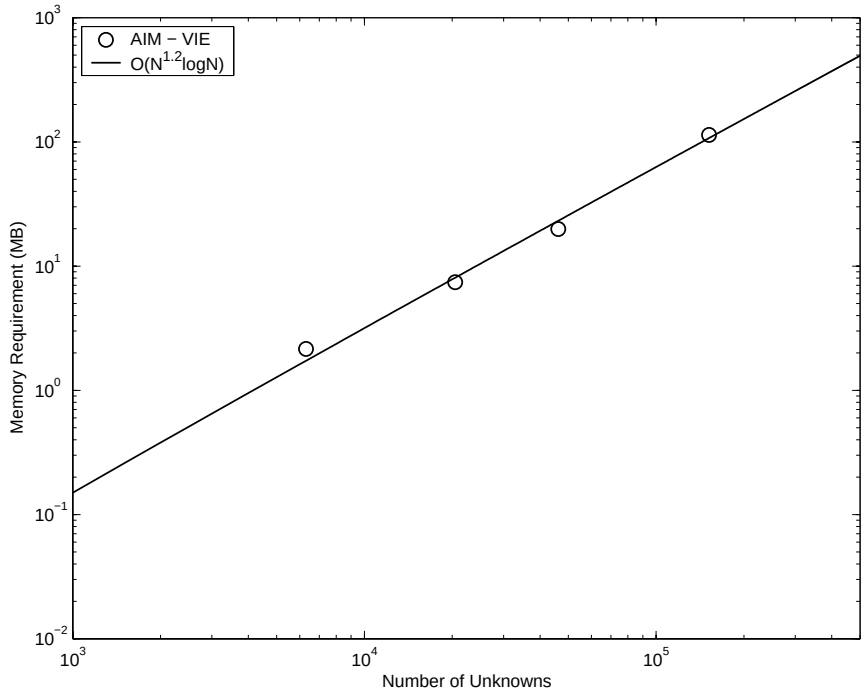

Figure 3.8: AIM memory requirement versus the number of unknowns for the volume integral equation.

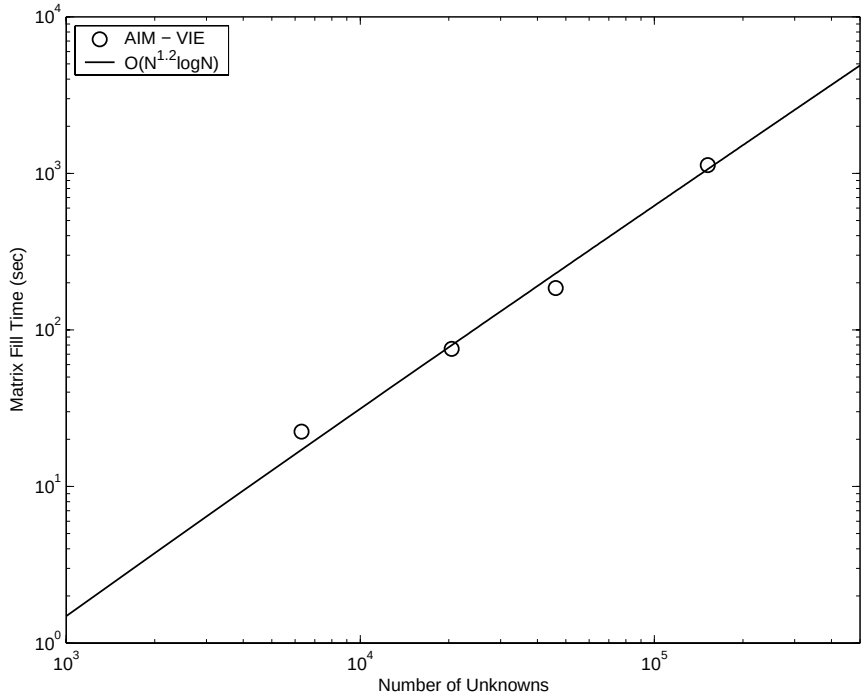

(a) Matrix filling

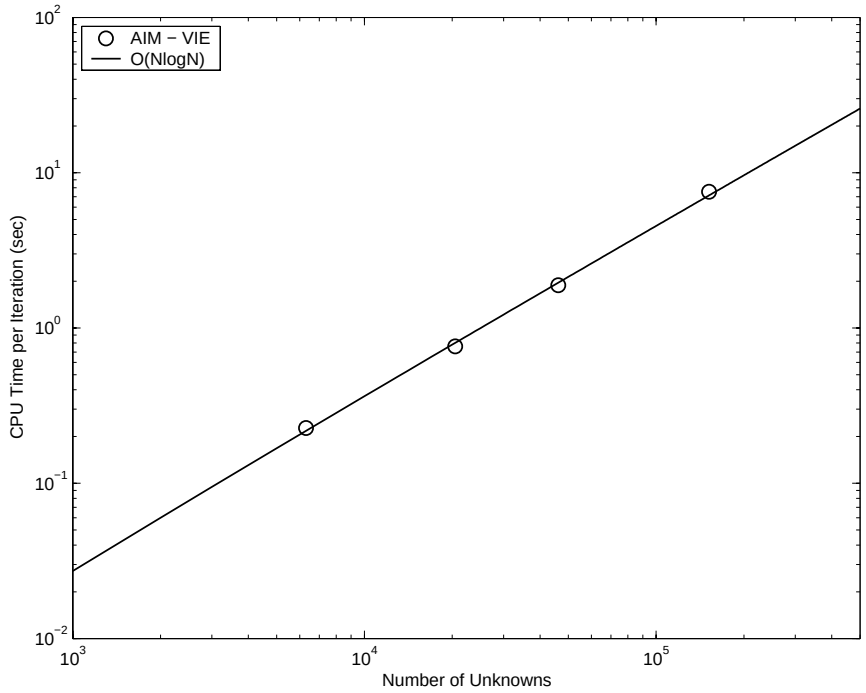

(b) Matrix-vector multiplication

Figure 3.9: AIM CPU time versus the number of unknowns for the volume integral equation. (a) Matrix filling. (b) Matrix-vector multiplication.

Chapter 4

Fast Solution to Scattering and Radiation Problems of Metallic Structures

4.1 Introduction

The most common material encountered in engineering application is metal. Metals are good conductors of electricity and have been used to construct antennas, transmission line, etc. The presence of metallic object will generate disturbance to the original field distributions, hence it is important to understand and analyze the electromagnetic scattering by metallic objects. In this chapter, we will first derive the integral equation that describes the electromagnetic problems of metallic structure. Then, we will use the MoM and AIM to analyze the electromagnetic scattering and radiation problems of electrically large metallic structures.

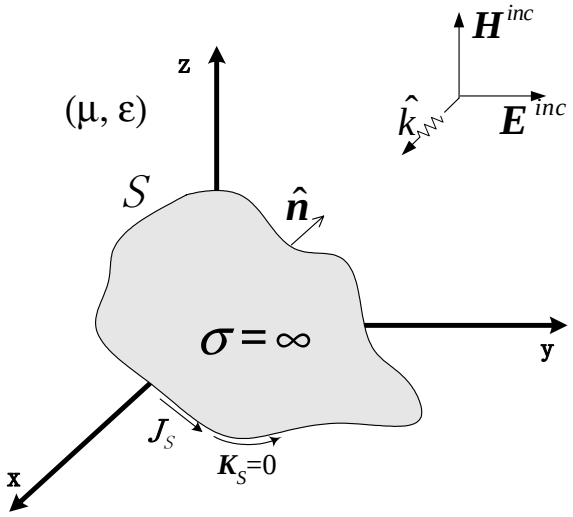

Figure 4.1: A perfect electric conductor embedded in an isotropic and homogeneous background and illuminated by incident plane waves

4.2 Formulation

Consider an arbitrarily shaped 3-D scatterer embedded in an isotropic homogeneous background medium with permittivity ϵ and permeability μ as shown in Fig. 4.1. We assume the scatterer is made of perfect electric conductor (PEC), whose conductivity $\sigma = \infty$. The scatterer is illuminated by an incident wave $\boldsymbol{E}^{inc}$, which is excited by impressed sources in the background media.

If we construct an artificial closed surface S outside the scatterer, we can invoke the surface equivalence principle and let the equivalent current densities flow on the surface S. Then we allow the artificial surface to shrink until it coincides with the surface of the PEC. By considering the boundary conditions on the surface of PEC, we have

- The tangential components of total electric field vanish on the surface; and
- The tangential components of total magnetic field are equal to the surface current density.

Mathematically the boundary conditions can be expressed as

$$\widehat{\boldsymbol{n}} \times \boldsymbol{E} = 0 \tag{4.1}$$

$$\widehat{\boldsymbol{n}} \times \boldsymbol{H} = \boldsymbol{J}_S, \tag{4.2}$$

where the $\boldsymbol{E}$ and $\boldsymbol{H}$ are the total electric and magnetic fields on the surface S. From Eq. (2.11), the equivalent magnetic current density, $\boldsymbol{K}_S$, is equal to the tangential components of total electrical field, hence

$$\boldsymbol{K}_S = 0. \tag{4.3}$$

Since the fields inside the metallic structure are zero, we can remove the metallic structure and fill the region with the background medium. Hence the $\boldsymbol{J}_S$ is radiating in the unbounded background medium. The scattered electric and magnetic fields can be determined from Eq. (2.4) as

$$\boldsymbol{E}^{sca} = -\eta \mathcal{L} \boldsymbol{J}_S \tag{4.4}$$

$$\boldsymbol{H}^{sca} = \mathcal{M} \boldsymbol{J}_S. \tag{4.5}$$

The total fields in Eqs. (4.1) and (4.2) comprise the incident and scattered fields. Hence substituting Eqs. (4.4) and (4.5) into Eqs. (4.1) and (4.2), we obtain

$$\widehat{\boldsymbol{n}} \times \boldsymbol{E}^{inc} = \widehat{\boldsymbol{n}} \times \eta \mathcal{L} \boldsymbol{J}_S \tag{4.6}$$

$$\widehat{\boldsymbol{n}} \times \boldsymbol{H}^{inc} = \boldsymbol{J}_S - \widehat{\boldsymbol{n}} \times \mathcal{M} \boldsymbol{J}_S. \tag{4.7}$$

Eqs. (4.6) and (4.7) are commonly referred to as electric field integral equation (EFIE) and magnetic field integral equation (MFIE), respectively, for PEC. It is noted that either EFIE or MFIE can be applied to solve the scattering problem of a closed surface PEC but the MFIE cannot be applied to treat an infinitesimally thin open structure object.

Using the EFIE or MFIE alone to solve the scattering problem of a closed surface structure will encounter interior resonance problem at specific resonance frequencies [82, 83]. The interior resonance problem will cause slow convergence and normally lead to incorrect solutions. This problem can be alleviated by using the combined field integral equation (CFIE) formulation [16]. The CFIE produces an unique solution at all frequencies and also produces better condition matrix equation compared to EFIE or MFIE. The CFIE can be obtained by linearly combining the EFIE and MFIE such that

$$\text{CFIE} = \alpha\text{EFIE} + (1-\alpha)\eta\text{MFIE}, \tag{4.8}$$

where α is a real number and $0 \leq \alpha \leq 1$. Notice that when $\alpha = 1$ and $\alpha = 0$, the Eq. (4.8) is reduced to the EFIE and the MFIE , respectively. Hence both EFIE and MFIE can be considered as the special cases of CFIE.

4.3 Method of Moments

The geometry of the PEC can be modeled using triangular or rectangular patches. The divergence-conforming subdomain basis functions are suitable for approximating the unknown surface current density. Here, we have discretized the surface of the metallic structure using triangular patches. If we denote the basis functions as $\boldsymbol{f}_n$, then the surface current density, $\boldsymbol{J}_S$, can be expanded as

$$\boldsymbol{J}_S = \sum_{n=1}^{N} I_n \boldsymbol{f}_n, \tag{4.9}$$

where the I_n denotes the unknown current coefficients. By using the Galerkin's testing procedure, the integral equation can be converted into a matrix equation

$$\overline{\boldsymbol{Z}}\boldsymbol{I} = \boldsymbol{V}, \tag{4.10}$$

where $\overline{\boldsymbol{Z}}$, $\boldsymbol{I}$ and $\boldsymbol{V}$ denote the impedance matrix, the vector of current coefficients, and the excitation vector, respectively. The excitation vector can be evaluated by

$$V_m = \int_{S_m} \boldsymbol{f}_m \cdot \left[\alpha \boldsymbol{E}^{inc}(\boldsymbol{r}) + (1-\alpha)\eta \boldsymbol{H}^{inc}(\boldsymbol{r})\right] dS \tag{4.11}$$

while the elements of the impedance matrix can be computed using

$$\begin{aligned} Z_{mn} \;=\; & \int_{S_m} \boldsymbol{f}_m \cdot \left[\alpha jk\eta \int_{S_n} \left(\boldsymbol{f}_n + \frac{\boldsymbol{\nabla}\boldsymbol{\nabla}' \cdot \boldsymbol{f}_n}{k^2}\right) G(\boldsymbol{r}, \boldsymbol{r}')\, dS' + \right. \\ & \left. (1-\alpha)\,\eta \left(\frac{1}{2}\boldsymbol{f}_n - \boldsymbol{\nabla} \times \oint_{S_n} \boldsymbol{f}_n G(\boldsymbol{r}, \boldsymbol{r}') dS'\right)\right] dS \end{aligned} \tag{4.12}$$

where $\oint_S$ is the Cauchy principal value.

4.4 AIM Implementation

We will use the AIM that has been discussed in Chapter 3 to accelerate the matrix-vector multiplication in the iterative solver. In order to use the AIM, the scatterer is first placed in a rectangular region and recursively subdivided into a total of W cells and each of the basis functions f_n is bounded by a cell which comprises $(M+1)^3 = 27$ grids. Let N_t denotes the total number of basis functions and $N_c(w)$ denote the number of basis functions enclosed by the w-th cell. In the initialization stage, the projection matrix of the current densities $\overline{\boldsymbol{\Lambda}}$ and the Green's function matrix $\overline{\boldsymbol{G}}$ are computed and stored. During the matrix-vector multiplication, the current density is first projected onto the grid points. Then the Fourier transform of the far-zone interactions is computed and subsequently transferred to the respective testing functions. Lastly, the corrections to the near-zone interactions are added to the output. The complete AIM algorithm for PEC objects is given in Algorithm 1 in pseudocode form.

/*Initialization */
Compute $\widetilde{\overline{\boldsymbol{G}}} = \mathrm{FFT}(\overline{\boldsymbol{G}})$
Compute $\overline{\boldsymbol{\Delta}} = \overline{\boldsymbol{Z}} - \overline{\boldsymbol{\Lambda}}\,\overline{\boldsymbol{G}}\,\overline{\boldsymbol{\Lambda}}^T$
/* Projection step */
Set $\widehat{\boldsymbol{I}} = 0$
for each cell $p = 1$ *to* W **do**
  for each basis function f_q in cell p, $q = 1$ *to* $N_c(p)$ **do**
    $\widehat{I}(p) = \widehat{I}(p) + [\Lambda(p,q)]^T I_q(p)$
  end
end
/* Far-zone interaction */
Compute $\widetilde{\boldsymbol{I}} = \mathrm{FFT}(\widehat{\boldsymbol{I}})$
Compute $\widetilde{\boldsymbol{P}} = \widetilde{\boldsymbol{G}} \cdot \widetilde{\boldsymbol{I}}$
Compute $\widehat{\boldsymbol{P}} = \mathrm{FFT}^{-1}(\widetilde{\boldsymbol{P}})$
Set $\boldsymbol{V} = 0$
for each cell $p = 1$ *to* W **do**
  for each basis function f_q in cell p, $q = 1$ *to* $N_c(p)$ **do**
    $V_q(p) = V_q(p) + \Lambda(p,q)\widehat{P}(p)$
  end
end
/* Near-zone interaction */
for each basis function f_p with $p = 1$ *to* N_t **do**
  for each basis function f_q with, $q = 1$ *to* $N_{nz}(p)$ **do**
    $V_q(p) = V_q(p) + \Delta(p,q)I_q(p)$
  end
end

Algorithm 1: AIM algorithm for solving electromagnetic scattering problems of PEC objects.

By using the AIM, the impedance matrix $\overline{\boldsymbol{Z}}$ is mathematically split into two components, i.e. $\overline{\boldsymbol{Z}}^{\mathrm{near}}$ and $\overline{\boldsymbol{Z}}^{\mathrm{far}}$. The far-zone interaction $\overline{\boldsymbol{Z}}^{\mathrm{far}}\boldsymbol{I}$ is approximated with the aid of FFT while the sparse near-zone matrix, $\overline{\boldsymbol{Z}}^{\mathrm{near}}$ is computed and stored in memory. An example of $\overline{\boldsymbol{Z}}^{\mathrm{near}}$ is shown in Fig. 4.2. It is generated by a metallic sphere having a radius of 1λ at 150 MHz. The total number of unknowns for this problem is 630 and the total non-zero entries of $\overline{\boldsymbol{Z}}^{\mathrm{near}}$ is 41,454. Hence the matrix storage requirement of $\overline{\boldsymbol{Z}}^{\mathrm{near}}$ is just about 10% of the full MoM matrix.

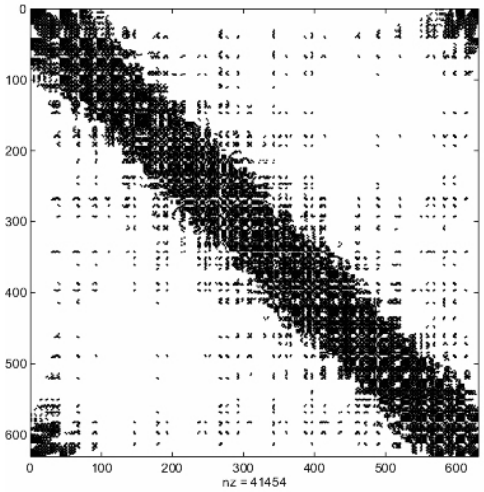

Figure 4.2: Sparsity pattern of $\overline{\boldsymbol{Z}}^{\text{near}}$ for a closed surface metallic object.

4.5 Numerical Examples

In this section, we will provide several examples to demonstrate the accuracy and the capability of our AIM implementation to solve electromagnetic problems of perfectly electric conducting objects. All the computations in this section are carried out on a general Pentium IV personal computer and the generalized minimal residual (GMRES) [84] iterative solver is used.

The first example we present is to serve as validation of the accuracy of our code. The first example is the scattering of a conducting sphere with a radius of 1 m. The bistatic radar cross sections (RCSs) of VV− and HH−polarizations at 500 MHz are computed using 11,172 unknowns and shown in Fig. 4.3. The solutions obtained by the Mie series are also shown for comparison. A good agreement is observed between the results. Next we show the convergence plot of EFIE, MFIE, and CFIE methods for solving the Example 1 in Fig. 4.4. We observe that the CFIE converges faster than both EFIE and MFIE. In the following examples, we will apply CFIE formulation to a closed surface scatterer and apply EFIE formulation to an open structure scatterer.

The second example we consider is the scattering of a NASA almond [85]. The

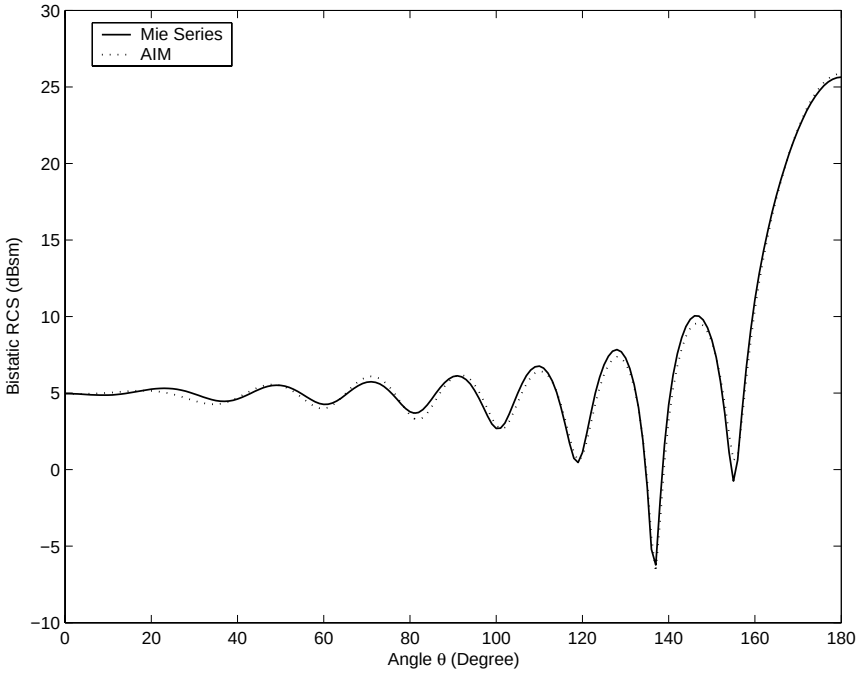

(a) VV−polarization

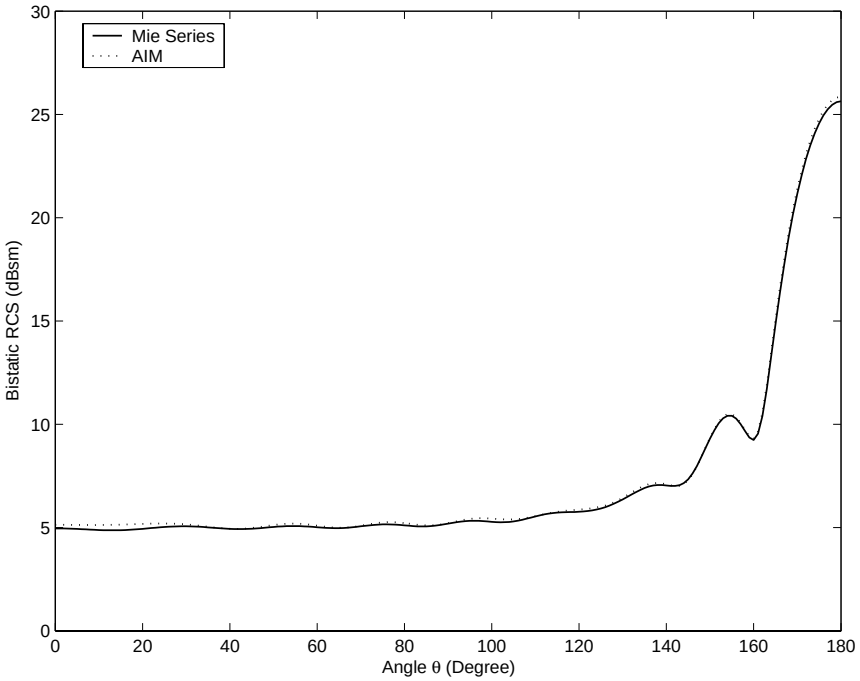

(b) HH−polarization

Figure 4.3: Bistatic RCSs of a metallic sphere with a radius of 1 m at 500 MHz. (a) VV−polarization. (b) HH−polarization.

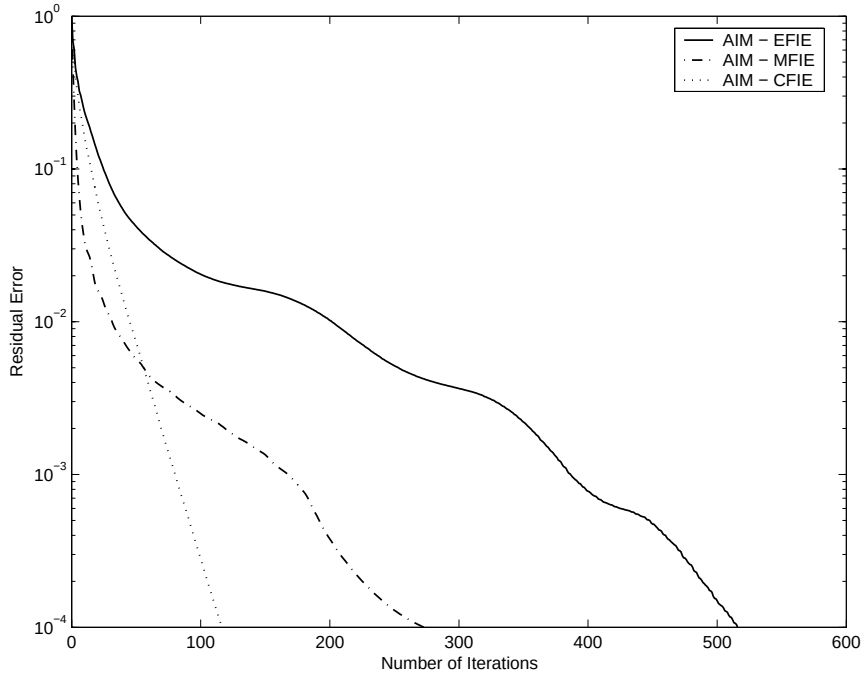

Figure 4.4: The convergence plot of EFIE, MFIE and CFIE with AIM for computing the bistatic RCS of a metallic sphere of 1 m radius at 500 MHz.

mathematical description of the almond surface is as follows:

$$
\begin{aligned}
&\text{for } -0.41667 < t < 0 \text{ and } -\pi < \phi < \pi \\
&\quad x = 0.2523744t \quad \text{m} \\
&\quad y = 0.0487923\sqrt{1-\left(\tfrac{t}{0.46667}\right)^2}\cos\phi \quad \text{m} \\
&\quad z = 0.0162640\sqrt{1-\left(\tfrac{t}{0.46667}\right)^2}\sin\phi \quad \text{m;} \\
&\text{for } 0 < t < 0.58333 \text{ and } -\pi < \phi < \pi \\
&\quad x = 0.2523744t \quad \text{m} \\
&\quad y = 1.2198390\left(\sqrt{1-\left(\tfrac{t}{2.08335}\right)^2} - 0.96\right)\cos\phi \quad \text{m} \\
&\quad z = 0.4066130\left(\sqrt{1-\left(\tfrac{t}{2.08335}\right)^2} - 0.96\right)\sin\phi \quad \text{m.}
\end{aligned}
$$

The geometry of the almond is shown in Fig. 4.5. The monostatic RCSs for VV−polarization at 7 GHz are computed and shown in Fig. 4.5. The corresponding maximum dimensions of the almond are $5.89\lambda \times 1.14\lambda \times 0.38\lambda$ and the discretization using triangular patches results in 9,750 unknowns. The computed results

agree well with the measured results especially at the tips.

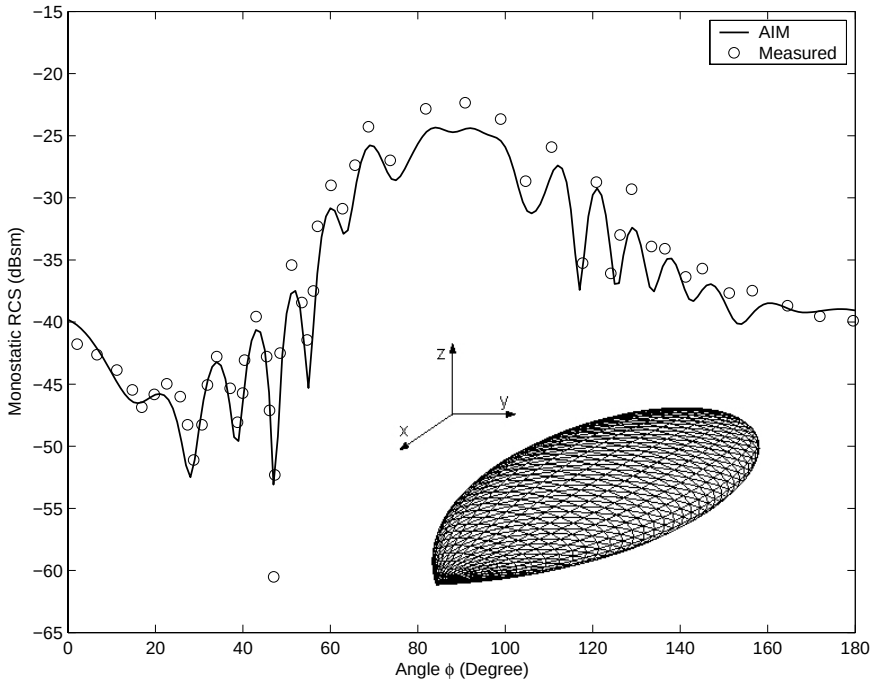

Figure 4.5: Monostatic RCSs for VV−polarization of a NASA almond at 7 GHz.

The third example is the scattering of a generic airplane[1]. The induced surface current is shown in Fig. 4.6. The monostatic RCSs for the VV− and HH−polarizations at 300 MHz and 1 GHz are computed with 6,459 and 62,619 unknowns, respectively. The results are shown in Fig. 4.7.

In the following examples, we will consider the application of AIM in computing the radiation patterns of antennas [57, 86]. The fourth examples is a metallic horn antenna. The dimensions of the pyramidal horn antenna are shown in Fig. 4.8. In this example, the pyramidal horn antenna is excited by an infinitesimal dipole placed inside the waveguide. The induced surface current is shown in Fig. 4.9. The radiation patterns in $E-$ and $H-$planes are shown in Fig. 4.10(a) and Fig. 4.10(b), respectively. We have observed a good agreement between the computed results and the measured results [87].

Next we consider the radiation patterns of a parabolic reflector. The parabolic

[1]The mesh of the generic airplane is provided by Dr. Li Er-Ping, Institute of High Performance Computing, Singapore.

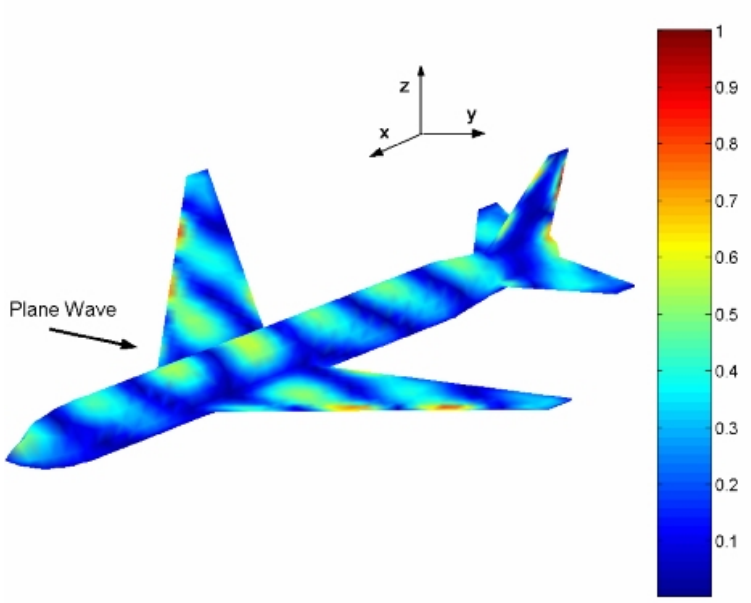

Figure 4.6: The normalized induced surface current on a generic airplane. The airplane is illuminated by a plane wave incident from the direction indicated by the arrow.

reflector is having a diameter of 5λ and the focus-to-diameter (F/D) ratio of the reflector is 0.375. The reflector is excited by an ideal dipole placed at the focus and backed by a circular disk. The induced surface current is shown in Fig. 4.11 and the respectively radiation patterns in $E-$ and $H-$planes are shown in Fig. 4.12(a) and Fig. 4.12(b). The computed results are compared with the measured results [87] and a good agreement is observed.

The sixth example we consider is a rectangular horn-fed parabolic reflector with different F/D ratios. The parabolic reflector is assumed to have the F/D ratios of 0.3, 0.375 and 0.4, and their respective diameters are 21λ, 17λ and 16λ. The aperture dimensions and height of the rectangular horn for feeding are $1.2\lambda \times 1.6\lambda$ and 3.5λ, respectively. The discretizations of these configurations have resulted in 126,948, 78,975 and 69,379 unknowns, respectively. The computed $E-$ and $H-$planes radiation patterns are shown in Fig. 4.13 for different F/D ratios.

The last example we present here is the radiation of a dipole on top of a generic car. The dipole is placed on top of the car, the induced current are shown in

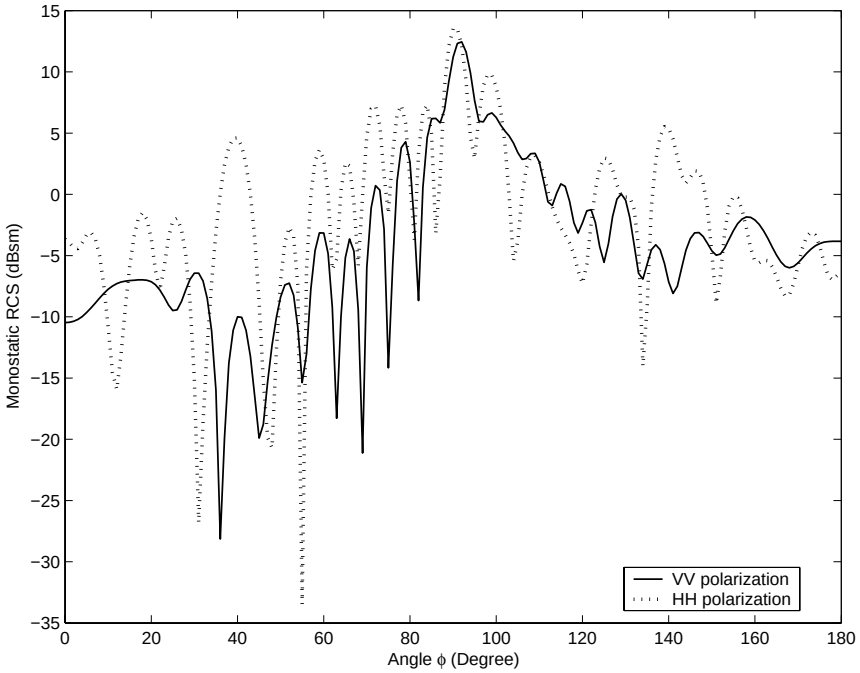

(a) 300 MHz

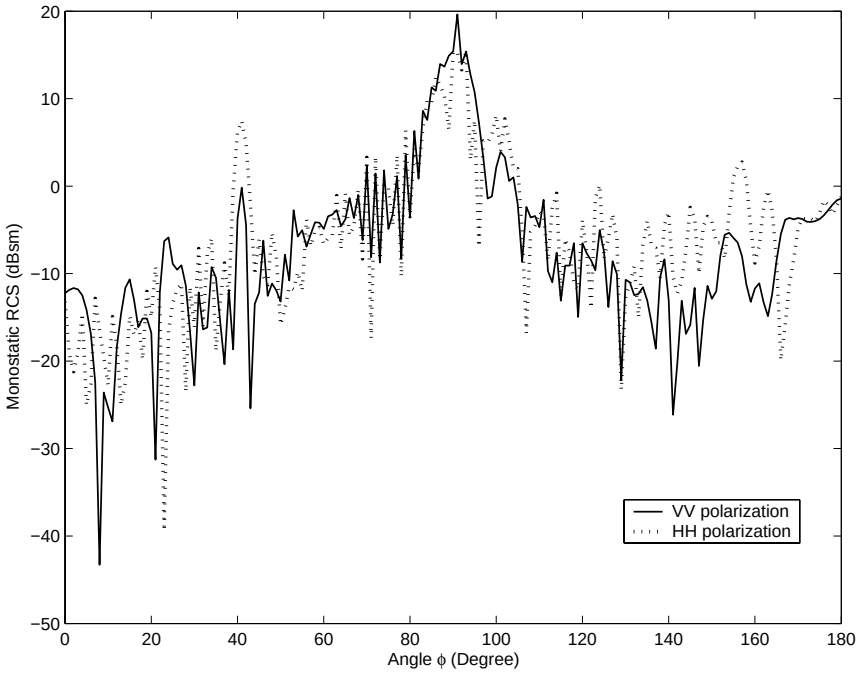

(b) 1 GHz

Figure 4.7: Monostatic RCSs of a generic airplane in XY plane. (a) 300 MHz. (b) 1 GHz.

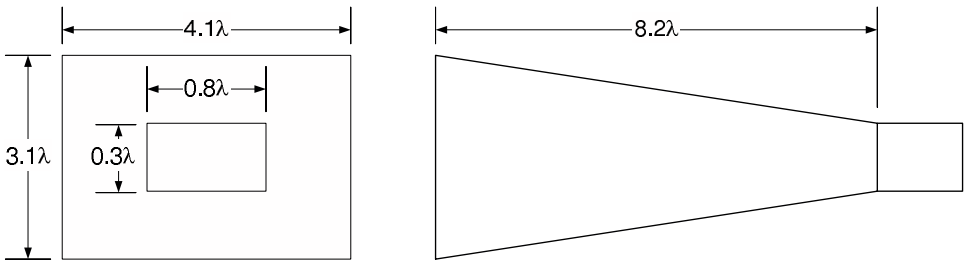

Figure 4.8: Dimension of the example pyramidal horn antenna.

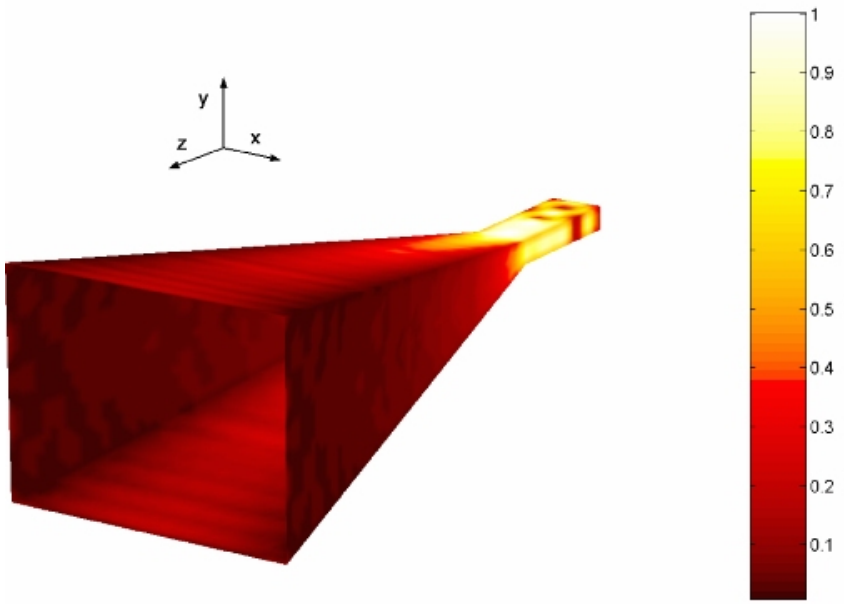

Figure 4.9: The normalized induced surface current on the pyramidal horn antenna excited by an infinitesimal dipole.

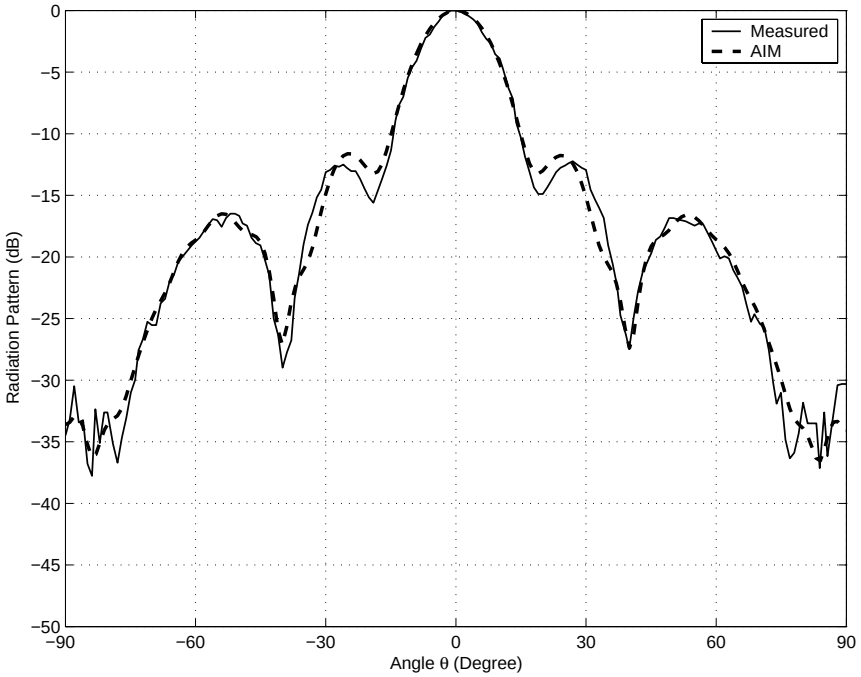

(a) $E-$plane

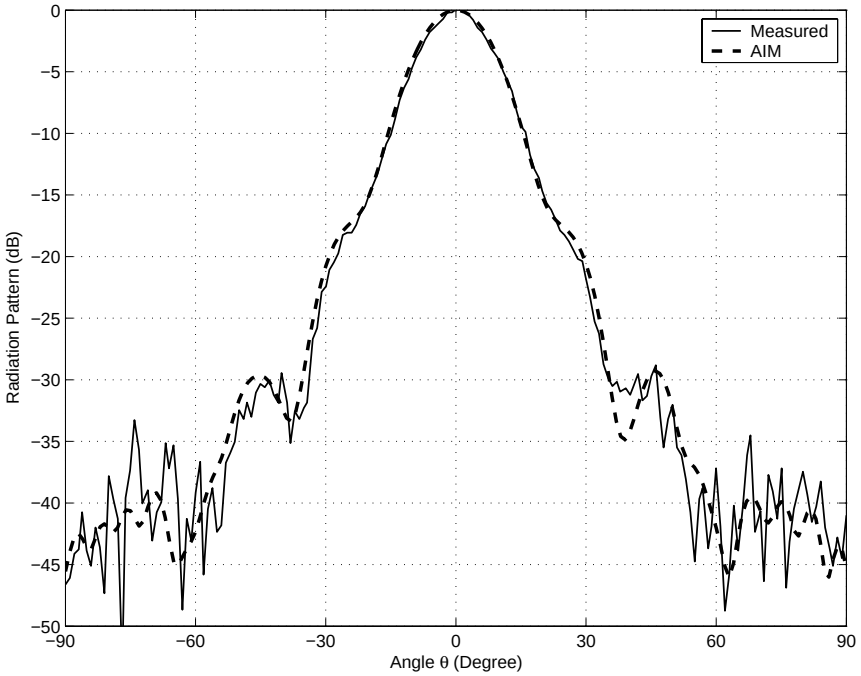

(b) $H-$plane

Figure 4.10: Radiation patterns of the pyramidal horn antenna. (a) $E-$plane. (b) $H-$plane.

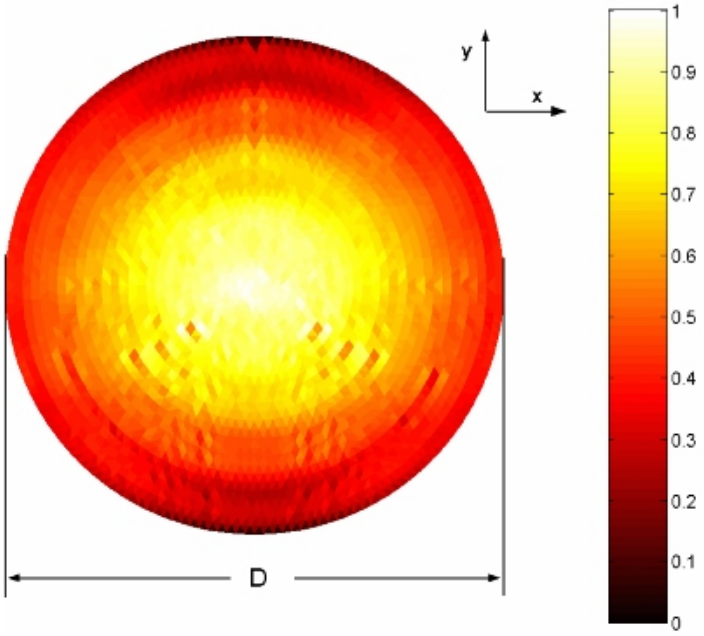

Figure 4.11: The normalized induced surface current on the parabolic reflector excited by an infinitesimal dipole backed with a circular plate.

Fig. 4.14. The radiation pattern in $XZ-$ and $YZ-$planes are shown in Fig. 4.15(a) and Fig. 4.15(b), respectively.

In Table 4.1, we compare the total memory consumed by the AIM and the estimated memory for the conventional MoM in computing these examples. From Table 4.1, we observe that the saving in memory requirement due to the AIM is more than 95%. We also find that although the memory requirement for the conventional MoM in some examples is far beyond the capability of a PC, but these examples could be easily handled by the AIM.

The CPU time consumed by AIM to compute these examples is shown in Table 4.2 and the estimated CPU time for MoM is also given for comparison purpose. We find that the saving in time is significant especially for electromagnetic problems with a large number of unknowns. Through these examples, we observe that the AIM has effectively reduced the CPU time needed for solving electromagnetic scattering problems of large-scale metallic structures.

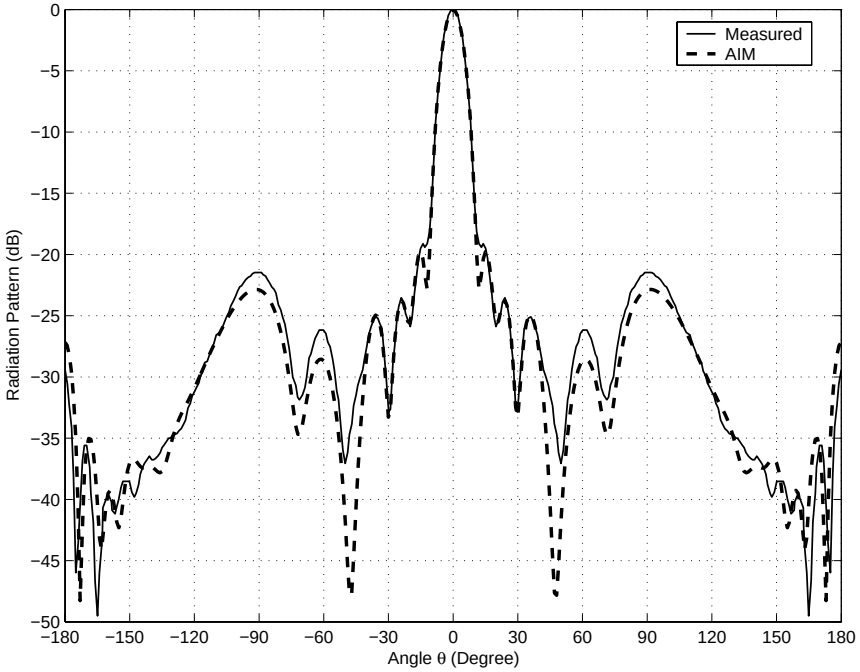

(a) $E-$plane

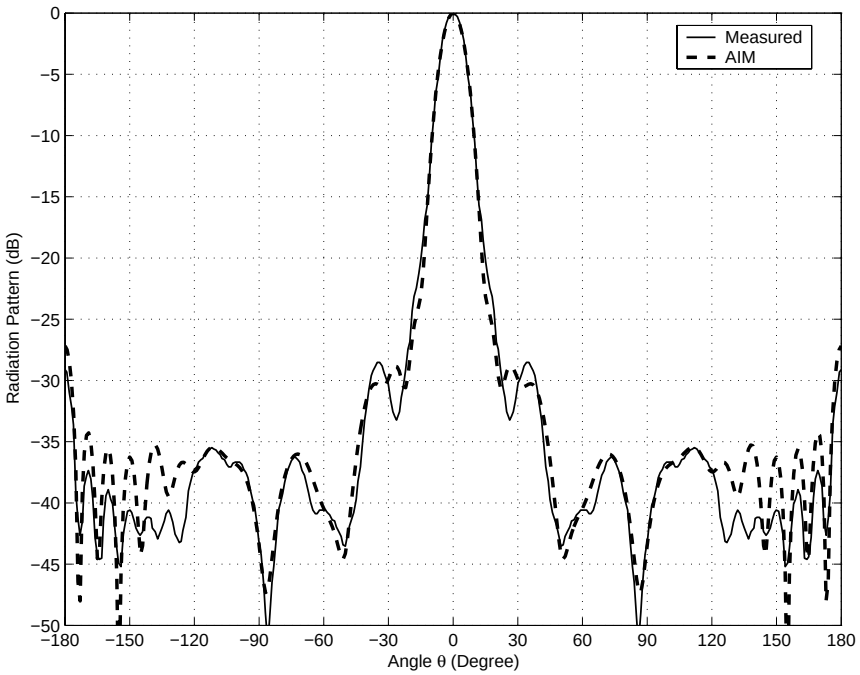

(b) $H-$plane

Figure 4.12: Radiation patterns of the parabolic reflector. (a) $E-$plane. (b) $H-$plane.

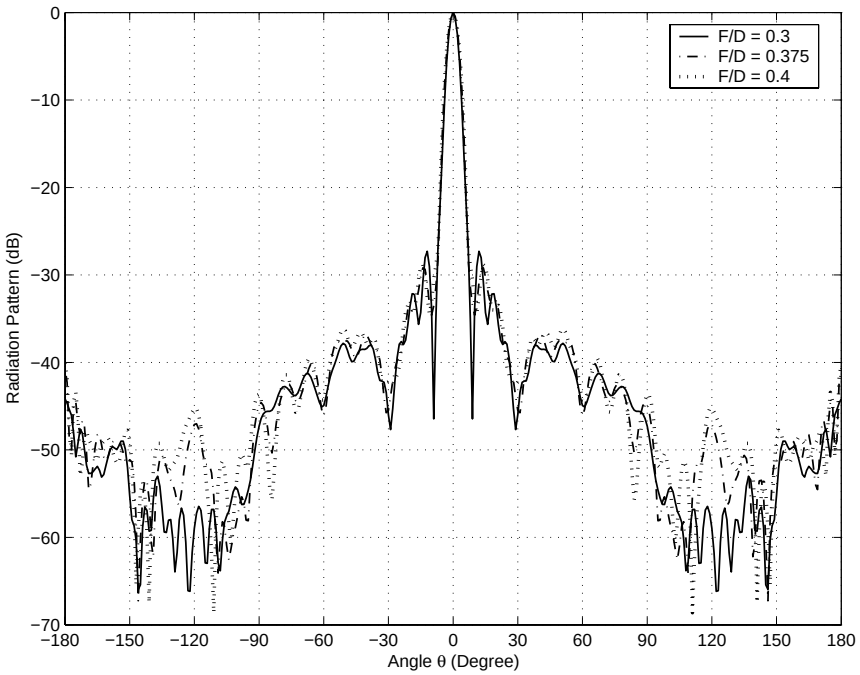

(a) $E-$plane

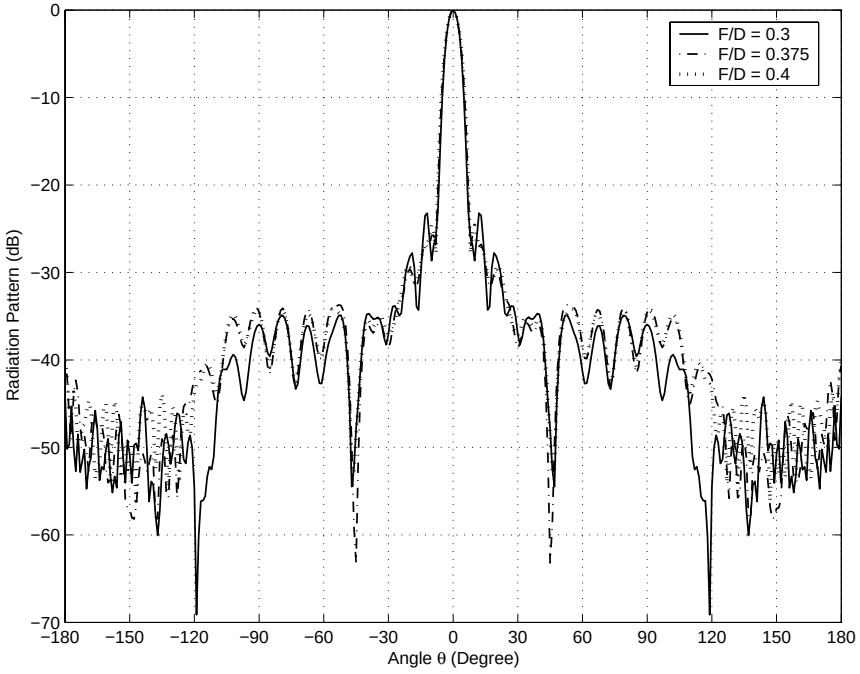

(b) $H-$plane

Figure 4.13: Radiation patterns of the horn fed parabolic reflector with different F/D ratios. (a) $E-$plane. (b) $H-$plane.

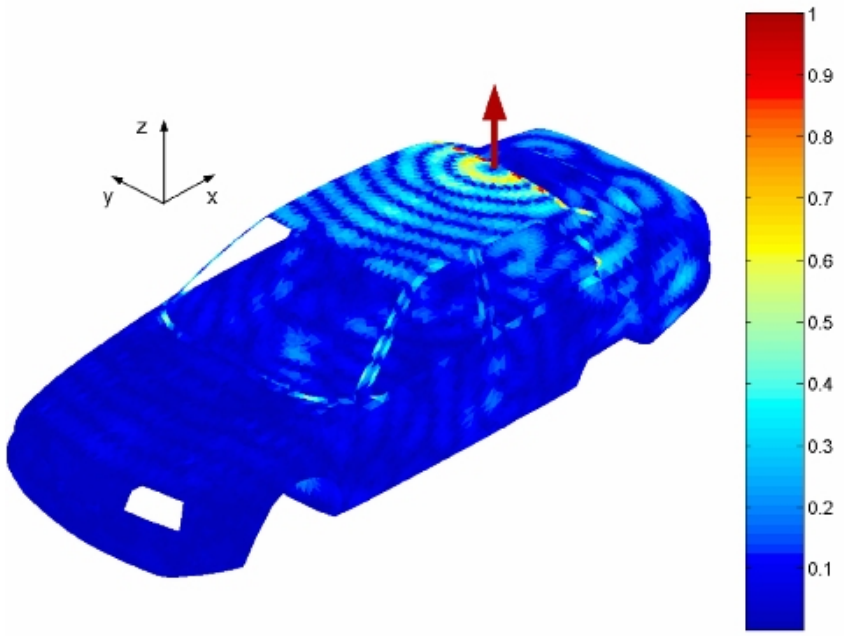

Figure 4.14: The normalized surface current induced on the generic car excited by an infinitesimal dipole placed on top of the car.

Table 4.1: Comparison of memory requirement between the AIM and the MoM in solving electromagnetic problems of metallic structures.

Example	Unknowns, N	AIM, M_{AIM}(MB)	MoM, M_{MoM}(GB)	M_{AIM}/M_{MoM}
Metallic sphere	11,172	15.33	0.93	1.61%
NASA almond	9,750	21.50	0.71	2.97%
Generic airplane (300 MHz)	6,459	13.95	0.31	4.38%
Generic airplane (1 GHz)	62,619	199.98	29.21	0.67%
Horn antenna	15,101	32.78	1.70	1.88%
Reflector	7,157	12.76	0.38	3.28%
Reflector F/D = 0.4	69,379	175.26	35.86	0.48%
Reflector F/D = 0.375	78,975	198.61	46.47	0.42%
Reflector F/D = 0.3	126,948	318.85	120.07	0.26%
Generic car	30,336	63.14	6.86	0.90%

Note: 1 KB = 1,024 Bytes, 1 MB = 1,024 KB and 1 GB = 1,024 MB

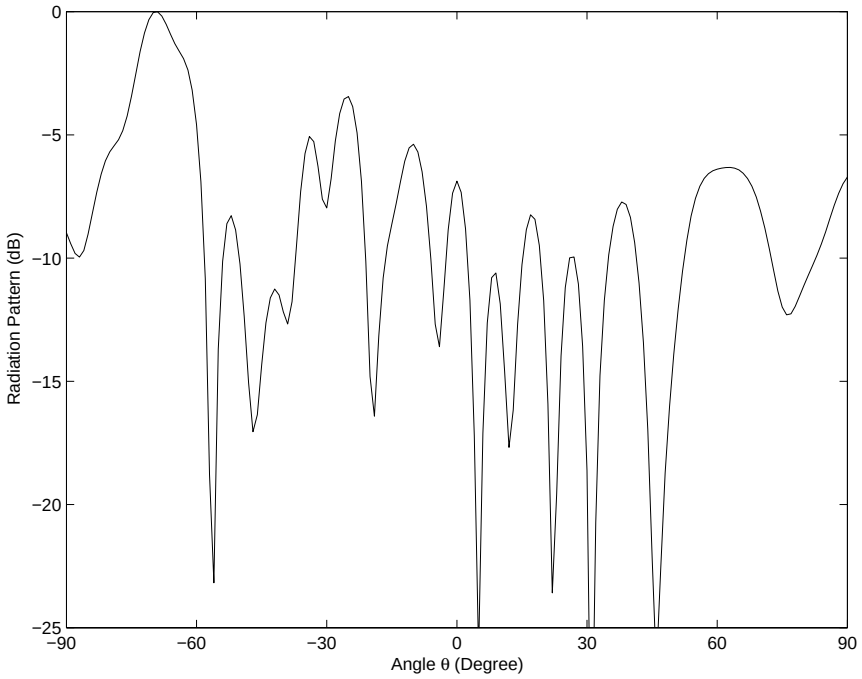

(a) $XZ-$plane

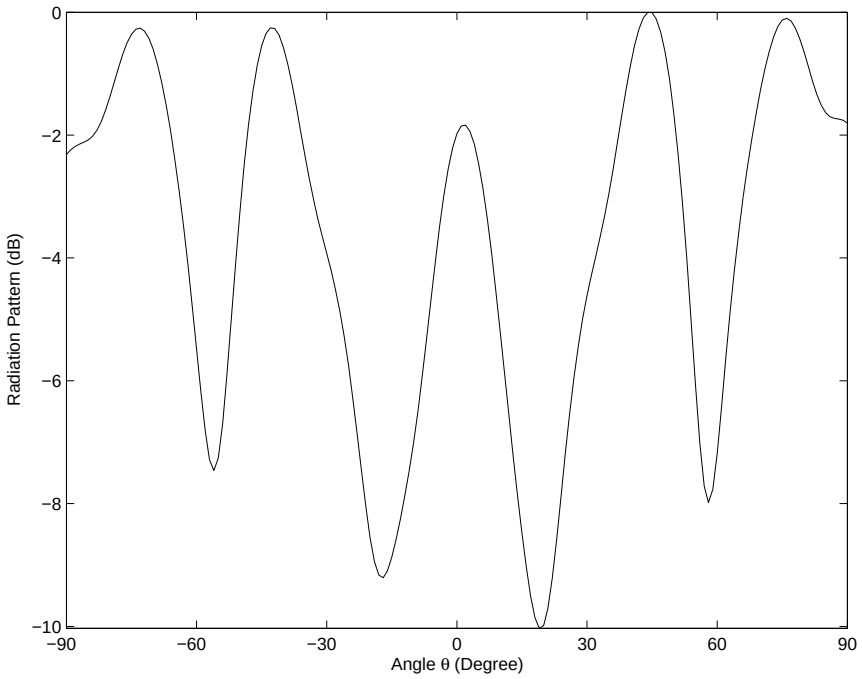

(b) $YZ-$plane

Figure 4.15: Radiation patterns of a dipole placed on top of a generic car. (a) $XZ-$plane. (b) $YZ-$plane.

Table 4.2: Comparison of CPU time between the AIM and the MoM in solving electromagnetic problems of metallic structures.

Example	Unknowns, N	AIM, T_{AIM}(sec)	Estimated MoM, T_{MoM}(sec)
Metallic sphere	11,172	41	120
NASA almond	9,750	106	334
Generic airplane (300 MHz)	6,459	53	77
Generic airplane (1 GHz)	62,619	3,137	7,670
Horn antenna	15,101	702	1,032
Reflector	7,157	148	161
Reflector F/D = 0.4	69,379	15,426	21,777
Reflector F/D = 0.375	78,975	19,800	31,136
Reflector F/D = 0.3	126,948	30,189	78,516
Generic car	30,336	6,025	8,813

Chapter 5

Fast Solution to Scattering Problems of Dielectric Objects

5.1 Introduction

The scattering problem of dielectric scatterer can be formulated using the surface integral equation (SIE) method [26, 27] or the volume integral equation (VIE) method [5, 7, 29]. The choice of the type of integral equations to be used is normally dependent on the inhomogeneity of the dielectric material. For a piecewise homogeneous dielectric material, it is advantageous to formulate the scattering problem using surface integral equation as the discretization process will produce less unknowns. However if the inhomogeneity of the dielectric material is complex, then the VIE is preferred as the SIE is required to be formulated in every inhomogeneous region.

In this chapter, the scattering problem of dielectric scatterer will be first solved by using the SIE method. The AIM algorithm will be modified to solve the resultant matrix equation [54]. Next, we will use the VIE method to characterize the scattering problem of dielectric scatterers with complex inhomogeneity. The original AIM algorithm will be modified in order to cope with the volume source.

5.2 Surface Integral Equation Method

By using the surface equivalence principle, it is possible to establish a set of integral equations to describe the scattering problem of dielectric objects in an unbounded medium. In this section, we will first carry out the formulation for piecewise dielectric object and then follow by the formulation for mixed dielectric objects.

5.2.1 Formulation for Piecewise Dielectric Object

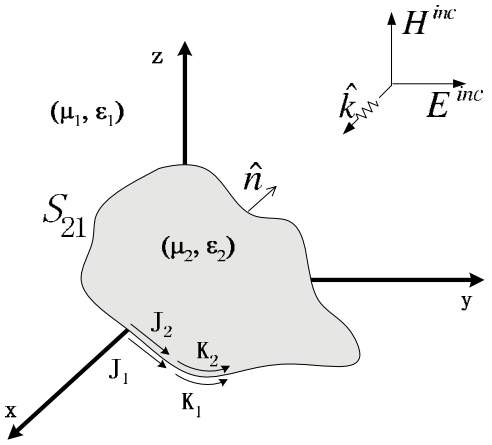

Figure 5.1: Geometry of a dielectric scatterer embedded in an isotropic homogeneous medium.

Consider the electromagnetic scattering problem of a 3-D arbitrarily shaped piecewise homogeneous dielectric object as shown in Fig. 5.1. The dielectric material of the object is characterized by the permeability, μ_2, and permittivity, ϵ_2. The scatterer is embedded in an unbounded medium characterized by (μ_1, ϵ_1), and is illuminated by an incident wave $\boldsymbol{E}^{inc}$.

We first construct an artificial closed surface S_{21} which is coincident with the surface of the scatterer. By using the surface equivalence principle, the equivalent electric and magnetic current densities flow on the surface are given by Eq. (2.11),

$$\boldsymbol{J}_1 = \hat{\boldsymbol{n}} \times \boldsymbol{H}_1 \tag{5.1}$$

$$\boldsymbol{K}_1 = \boldsymbol{E}_1 \times \hat{\boldsymbol{n}}, \tag{5.2}$$

where the $\boldsymbol{E}_1$ and $\boldsymbol{H}_1$ are the respective total electric and magnetic fields in medium 1. The scattered fields produced by the equivalent current densities are

$$\boldsymbol{E}^{sca} = -\eta_1 \mathcal{L}_1 \boldsymbol{J}_1 - \mathcal{M}_1 \boldsymbol{K}_1 \tag{5.3}$$

$$\boldsymbol{H}^{sca} = \mathcal{M}_1 \boldsymbol{J}_1 - \frac{1}{\eta_1} \mathcal{L}_1 \boldsymbol{K}_1, \tag{5.4}$$

where $\eta_i = \sqrt{\mu_i/\epsilon_i}$. The operators $\mathcal{L}_i$ and $\mathcal{M}_i$ are defined as

$$\mathcal{L}_i \boldsymbol{X} = jk_i \int_\Omega \boldsymbol{X} G_i + \frac{1}{k_i^2} \boldsymbol{\nabla}\boldsymbol{\nabla} \cdot (\boldsymbol{X} G_i)\, d\Omega' \tag{5.5}$$

$$\mathcal{M}_i \boldsymbol{X} = \boldsymbol{\nabla} \times \int_\Omega \boldsymbol{X} G_i \, d\Omega' \tag{5.6}$$

where $k_i = \omega\sqrt{\mu_i \epsilon_i}$ and the Green's function is given by

$$G_i = \frac{e^{-jk_i|\boldsymbol{r}-\boldsymbol{r'}|}}{4\pi|\boldsymbol{r}-\boldsymbol{r'}|}. \tag{5.7}$$

Knowing that the total fields comprise incident and scattered fields, we substitute Eqs. (5.3)–(5.4) into the Eqs. (5.1)–(5.2) to obtain the respective EFIE and MFIE below:

$$-\boldsymbol{K}_1 + \widehat{\boldsymbol{n}} \times \eta_1 \mathcal{L}_1 \boldsymbol{J}_1 + \widehat{\boldsymbol{n}} \times \mathcal{M}_1 \boldsymbol{K}_1 = \widehat{\boldsymbol{n}} \times \boldsymbol{E}^{inc} \tag{5.8}$$

$$\boldsymbol{J}_1 - \widehat{\boldsymbol{n}} \times \mathcal{M}_1 \boldsymbol{J}_1 + \widehat{\boldsymbol{n}} \times \frac{1}{\eta_1} \mathcal{L}_1 \boldsymbol{K}_1 = \widehat{\boldsymbol{n}} \times \boldsymbol{H}^{inc}. \tag{5.9}$$

Next, we can setup a second equivalence relationship inside the dielectric scatterer. The mathematical surface is coincident with the interior surface of the scatterer and the equivalent current densities are given by

$$\boldsymbol{J}_2 = (-\widehat{\boldsymbol{n}}) \times \boldsymbol{H}_2 \tag{5.10}$$

$$\boldsymbol{K}_2 = \boldsymbol{E}_2 \times (-\widehat{\boldsymbol{n}}) \tag{5.11}$$

where $\widehat{\boldsymbol{n}}$ is the normal vector pointing into medium 1. The second equivalence

replicates the original fields in medium 2 and produce null fields throughout the medium 1. By considering the scattered fields produced by the second set of equivalent current densities, we can obtain the EFIE and MFIE for the interior region

$$-\boldsymbol{K}_2 - \widehat{\boldsymbol{n}} \times \eta_2 \mathcal{L}_2 \boldsymbol{J}_2 - \widehat{\boldsymbol{n}} \times \mathcal{M}_2 \boldsymbol{K}_2 = 0 \tag{5.12}$$

$$\boldsymbol{J}_2 + \widehat{\boldsymbol{n}} \times \mathcal{M}_2 \boldsymbol{J}_2 - \widehat{\boldsymbol{n}} \times \frac{1}{\eta_2} \mathcal{L}_2 \boldsymbol{K}_2 = 0. \tag{5.13}$$

By considering the continuity of the tangential components of total electric field and magnetic field across the boundary, the two sets of equivalent current densities are related by

$$\boldsymbol{J}_2 = -\boldsymbol{J}_1 \tag{5.14}$$

$$\boldsymbol{K}_2 = -\boldsymbol{K}_1. \tag{5.15}$$

If we denote

$$\boldsymbol{J}_{21} = \boldsymbol{J}_1 = -\boldsymbol{J}_2 \tag{5.16}$$

$$\boldsymbol{K}_{21} = \boldsymbol{K}_1 = -\boldsymbol{K}_2, \tag{5.17}$$

we can combine the two sets of equivalence and produce the coupled field integral equation. The coupled EFIE and MFIE are

$$\widehat{\boldsymbol{n}} \times (\eta_1 \mathcal{L}_1 + \eta_2 \mathcal{L}_2) \boldsymbol{J}_{21} + \widehat{\boldsymbol{n}} \times (\mathcal{M}_1 + \mathcal{M}_2) \boldsymbol{K}_{21} = \widehat{\boldsymbol{n}} \times \boldsymbol{E}^{inc} \tag{5.18}$$

$$-\widehat{\boldsymbol{n}} \times (\mathcal{M}_1 + \mathcal{M}_2) \boldsymbol{J}_{21} + \widehat{\boldsymbol{n}} \times (\frac{1}{\eta_1} \mathcal{L}_1 + \frac{1}{\eta_2} \mathcal{L}_2) \boldsymbol{K}_{21} = \widehat{\boldsymbol{n}} \times \boldsymbol{H}^{inc}. \tag{5.19}$$

This formulation is commonly known as Poggio-Miller-Chang-Harrington-Wu-Tsai (PMCHWT) formulation [22–24]. This formulation is free of interior resonance and thus yields accurate and stable solutions.

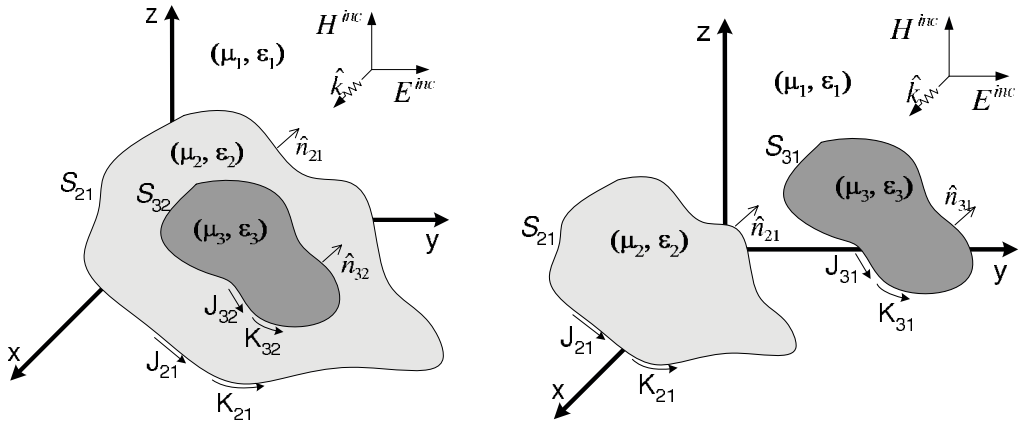

(a) Coated dielectric object (b) Discrete dielectric objects

Figure 5.2: Geometry of two dielectric scatterers in an isotropic homogeneous medium.

5.2.2 Formulation for Mixed Dielectric Objects

In this section, we can use the results obtained earlier to characterize the electromagnetic scattering problem for mixed dielectric objects. For this problem, we will consider two sets of configuration, i.e. coated object and discrete objects, as shown in Fig. 5.2(a) and Fig. 5.2(b). We will only derive the formulation for the coated object and the formulation for the discrete objects can be easily deduced from it.

Fig. 5.2(a) depicts an arbitrarily shaped 3-D dielectric scatterer coated by another dielectric material immersed in a homogeneous medium with permittivity ϵ_1 and permeability μ_1. The scatterer and coating material have different material properties characterized respectively by (μ_2, ϵ_2) and (μ_3, ϵ_3). The interface between media i and j is denoted as S_{ji}. The unit vector normal to S_{ji} and pointing toward the medium i is denoted as $\hat{\boldsymbol{n}}_{ji}$.

Unlike the single dielectric scatterer, we need to apply the surface equivalence principle on every surface. Hence the equivalent surface electric and magnetic current densities are defined as

$$\boldsymbol{J}_{ji} = \hat{\boldsymbol{n}}_{ji} \times \boldsymbol{H}_i \text{ on } S_{ji} \tag{5.20}$$

$$\boldsymbol{K}_{ji} = \boldsymbol{E}_i \times \hat{\boldsymbol{n}}_{ji} \text{ on } S_{ji}. \tag{5.21}$$

Here we do not define the corresponding second set of equivalent current densities, as they are identical to the first set of equivalent current densities, except that they differ by a sign.

By using the PMCHWT formulation, the coupled EFIE and MFIE on the surface S_{21} can be written as

$$\begin{aligned}
\hat{\boldsymbol{n}}_{21} \times \boldsymbol{E}^{inc} &= \hat{\boldsymbol{n}}_{21} \times (\eta_1 \mathcal{L}_1 + \eta_2 \mathcal{L}_2) \boldsymbol{J}_{21} + \hat{\boldsymbol{n}}_{21} \times (\mathcal{M}_1 + \mathcal{M}_2) \boldsymbol{K}_{21} \\
&\quad - \hat{\boldsymbol{n}}_{21} \times \eta_2 \mathcal{L}_2 \boldsymbol{J}_{32} - \hat{\boldsymbol{n}}_{21} \times \mathcal{M}_2 \boldsymbol{K}_{32} \qquad (5.22) \\
\hat{\boldsymbol{n}}_{21} \times \boldsymbol{H}^{inc} &= -\hat{\boldsymbol{n}}_{21} \times (\mathcal{M}_1 + \mathcal{M}_2) \boldsymbol{J}_{21} + \hat{\boldsymbol{n}}_{21} \times (\frac{1}{\eta_1} \mathcal{L}_1 + \frac{1}{\eta_2} \mathcal{L}_2) \boldsymbol{K}_{21} \\
&\quad + \hat{\boldsymbol{n}}_{21} \times \mathcal{M}_2 \boldsymbol{J}_{32} - \hat{\boldsymbol{n}}_{21} \times \frac{1}{\eta_2} \mathcal{L}_2 \boldsymbol{K}_{32}. \qquad (5.23)
\end{aligned}$$

Similarly, the coupled EFIE and MFIE on the surface S_{32} can be written as

$$\begin{aligned}
0 &= \hat{\boldsymbol{n}}_{32} \times (\eta_2 \mathcal{L}_2 + \eta_3 \mathcal{L}_3) \boldsymbol{J}_{32} + \hat{\boldsymbol{n}}_{32} \times (\mathcal{M}_2 + \mathcal{M}_3) \boldsymbol{K}_{32} \\
&\quad - \hat{\boldsymbol{n}}_{32} \times \eta_2 \mathcal{L}_2 \boldsymbol{J}_{21} - \hat{\boldsymbol{n}}_{32} \times \mathcal{M}_2 \boldsymbol{K}_{21} \qquad (5.24) \\
0 &= -\hat{\boldsymbol{n}}_{32} \times (\mathcal{M}_2 + \mathcal{M}_3) \boldsymbol{J}_{32} + \hat{\boldsymbol{n}}_{32} \times (\frac{1}{\eta_2} \mathcal{L}_2 + \frac{1}{\eta_3} \mathcal{L}_3) \boldsymbol{K}_{32} \\
&\quad + \hat{\boldsymbol{n}}_{32} \times \mathcal{M}_2 \boldsymbol{J}_{21} - \hat{\boldsymbol{n}}_{32} \times \frac{1}{\eta_2} \mathcal{L}_2 \boldsymbol{K}_{21}. \qquad (5.25)
\end{aligned}$$

If we repeat the same procedure for the discrete scatterers as shown in Fig. 5.2(b), we can obtain

$$\begin{aligned}
\hat{\boldsymbol{n}}_{21} \times \boldsymbol{E}^{inc} &= \hat{\boldsymbol{n}}_{21} \times (\eta_1 \mathcal{L}_1 + \eta_2 \mathcal{L}_2) \boldsymbol{J}_{21} + \hat{\boldsymbol{n}}_{21} \times (\mathcal{M}_1 + \mathcal{M}_2) \boldsymbol{K}_{21} \\
&\quad + \hat{\boldsymbol{n}}_{21} \times \eta_1 \mathcal{L}_1 \boldsymbol{J}_{31} + \hat{\boldsymbol{n}}_{21} \times \mathcal{M}_1 \boldsymbol{K}_{31} \qquad (5.26) \\
\hat{\boldsymbol{n}}_{21} \times \boldsymbol{H}^{inc} &= -\hat{\boldsymbol{n}}_{21} \times (\mathcal{M}_1 + \mathcal{M}_2) \boldsymbol{J}_{21} + \hat{\boldsymbol{n}}_{21} \times (\frac{1}{\eta_1} \mathcal{L}_1 + \frac{1}{\eta_2} \mathcal{L}_2) \boldsymbol{K}_{21} \\
&\quad - \hat{\boldsymbol{n}}_{21} \times \mathcal{M}_1 \boldsymbol{J}_{31} + \hat{\boldsymbol{n}}_{21} \times \frac{1}{\eta_1} \mathcal{L}_1 \boldsymbol{K}_{31} \qquad (5.27) \\
\hat{\boldsymbol{n}}_{31} \times \boldsymbol{E}^{inc} &= \hat{\boldsymbol{n}}_{31} \times (\eta_1 \mathcal{L}_1 + \eta_3 \mathcal{L}_3) \boldsymbol{J}_{31} + \hat{\boldsymbol{n}}_{31} \times (\mathcal{M}_1 + \mathcal{M}_1) \boldsymbol{K}_{31} \\
&\quad + \hat{\boldsymbol{n}}_{31} \times \eta_1 \mathcal{L}_1 \boldsymbol{J}_{21} + \hat{\boldsymbol{n}}_{31} \times \mathcal{M}_1 \boldsymbol{K}_{21} \qquad (5.28) \\
\hat{\boldsymbol{n}}_{31} \times \boldsymbol{H}^{inc} &= -\hat{\boldsymbol{n}}_{31} \times (\mathcal{M}_1 + \mathcal{M}_3) \boldsymbol{J}_{31} + \hat{\boldsymbol{n}}_{31} \times (\frac{1}{\eta_1} \mathcal{L}_1 + \frac{1}{\eta_3} \mathcal{L}_3) \boldsymbol{K}_{31}
\end{aligned}$$

$$-\widehat{\boldsymbol{n}}_{31}\times\mathcal{M}_1\boldsymbol{J}_{21}+\widehat{\boldsymbol{n}}_{31}\times\frac{1}{\eta_1}\mathcal{L}_1\boldsymbol{K}_{21}. \tag{5.29}$$

5.2.3 Method of Moments

In this section, we will only discuss the discretization of mixed dielectric scatterer as it is a more general case compared to the single dielectric scatterer. The coupled integral equations derived in the previous sections are discretized using the RWG basis functions. The equivalent surface electric and magnetic current densities $\boldsymbol{J}_{ji}$ and $\boldsymbol{K}_{ji}$ ($j = 2$ or 3) are expanded as follows:

$$\boldsymbol{J}_{ji}=\sum I_{n_{j-1}}\boldsymbol{f}_{n_{j-1}} \tag{5.30}$$

$$\boldsymbol{K}_{ji}=\sum M_{n_{j-1}}\boldsymbol{f}_{n_{j-1}}. \tag{5.31}$$

Substituting Eqs. (5.30–5.31) into Eqs. (5.22–5.25) and (5.26–5.29), and applying the Galerkin's testing procedure, we convert the integral equations to a linear equation system written as

$$\begin{pmatrix} \overline{\boldsymbol{Z}}^{E_1I_1} & \overline{\boldsymbol{C}}^{E_1M_1} & \theta\overline{\boldsymbol{Z}}^{E_1I_2} & \theta\overline{\boldsymbol{C}}^{E_1M_2} \\ \overline{\boldsymbol{D}}^{H_1I_1} & \overline{\boldsymbol{Y}}^{H_1M_1} & \theta\overline{\boldsymbol{D}}^{H_1I_2} & \theta\overline{\boldsymbol{Y}}^{H_1M_2} \\ \theta\overline{\boldsymbol{Z}}^{E_2I_1} & \theta\overline{\boldsymbol{C}}^{E_2M_1} & \overline{\boldsymbol{Z}}^{E_2I_2} & \overline{\boldsymbol{C}}^{E_2M_2} \\ \theta\overline{\boldsymbol{D}}^{H_2I_1} & \theta\overline{\boldsymbol{Y}}^{H_2M_1} & \overline{\boldsymbol{D}}^{H_2I_2} & \overline{\boldsymbol{Y}}^{H_2M_2} \end{pmatrix} \begin{pmatrix} \boldsymbol{I}_1 \\ \boldsymbol{M}_1 \\ \boldsymbol{I}_2 \\ \boldsymbol{M}_2 \end{pmatrix} = \begin{pmatrix} \boldsymbol{E}_1 \\ \boldsymbol{H}_1 \\ \delta\boldsymbol{E}_2 \\ \delta\boldsymbol{H}_2 \end{pmatrix} \tag{5.32}$$

where the ($\boldsymbol{I}_1$, $\boldsymbol{M}_1$) and ($\boldsymbol{I}_2$,$\boldsymbol{M}_2$) are the coefficients of the equivalent electric and magnetic current densities on S_{2i} and S_{3i}, respectively. The elements of the sub-matrices, for $u \neq v$, are defined as

$$Z_{mn}^{E_uI_v}=-\int\limits_{T_{m_u}}\boldsymbol{f}_{m_u}(\mathbf{r})\cdot\left(j\omega\mu_a\boldsymbol{P}_{n_v}^a+\frac{j}{\omega\epsilon_a}\boldsymbol{Q}_{n_v}^a\right)dS_{m_u} \tag{5.33a}$$

$$Y_{mn}^{H_uM_v}=-\int\limits_{T_{m_u}}\boldsymbol{f}_{m_u}(\mathbf{r})\cdot\left(j\omega\epsilon_a\boldsymbol{P}_{n_v}^a+\frac{j}{\omega\mu_a}\boldsymbol{Q}_{n_v}^a\right)dS_{m_u} \tag{5.33b}$$

$$C_{mn}^{E_uM_v}=-\int\limits_{T_{m_u}}\boldsymbol{f}_{m_u}(\mathbf{r})\cdot\left(\boldsymbol{\nabla}\times\boldsymbol{P}_{n_v}^a\right)dS_{m_u} \tag{5.33c}$$

$$D_{mn}^{H_u I_v} = -C_{mn}^{E_u M_v}; \tag{5.33d}$$

and for $u = v$, as:

$$Z_{mn}^{E_u I_u} = \int\limits_{T_{m_u}} \boldsymbol{f}_{m_u}(\mathbf{r}) \cdot \Big(j\omega\mu_b \boldsymbol{P}_{n_u}^b + \frac{j}{\omega\epsilon_b} \boldsymbol{Q}_{n_u}^b + j\omega\mu_{u+1} \boldsymbol{P}_{n_u}^{u+1} + \frac{j}{\omega\epsilon_{u+1}} \boldsymbol{Q}_{n_u}^{u+1} \Big)\, dS_{m_u} \tag{5.34a}$$

$$Y_{mn}^{H_u M_u} = \int\limits_{T_{m_u}} \boldsymbol{f}_{m_u}(\mathbf{r}) \cdot \Big(j\omega\epsilon_b \boldsymbol{P}_{n_u}^b + \frac{j}{\omega\mu_b} \boldsymbol{Q}_{n_u}^b + j\omega\epsilon_{u+1} \boldsymbol{P}_{n_u}^{u+1} + \frac{j}{\omega\mu_{u+1}} \boldsymbol{Q}_{n_u}^{u+1} \Big)\, dS_{m_u} \tag{5.34b}$$

$$C_{mn}^{E_u M_u} = \int\limits_{T_{m_u}} \boldsymbol{f}_{m_u}(\mathbf{r}) \cdot \Big(\boldsymbol{\nabla} \times \boldsymbol{P}_{n_u}^b + \boldsymbol{\nabla} \times \boldsymbol{P}_{n_u}^{u+1} \Big)\, dS_{m_u} \tag{5.34c}$$

$$D_{mn}^{H_u I_u} = -C_{mn}^{E_u M_u}; \tag{5.34d}$$

where

$$\boldsymbol{P}_{n_v}^u = \int\limits_{T_{n_v}} \boldsymbol{f}_{n_v}(\mathbf{r}') G_u(\mathbf{r}, \mathbf{r}')\, dS_{n_v} \tag{5.35}$$

$$\boldsymbol{Q}_{n_v}^u = \boldsymbol{\nabla} \int\limits_{T_{n_v}} \boldsymbol{\nabla}_s' \cdot \boldsymbol{f}_{n_v}(\mathbf{r}') G_u(\mathbf{r}, \mathbf{r}')\, dS_{n_v}; \tag{5.36}$$

while the symbols, μ_a and ϵ_a, denote the permeability and permittivity in medium a, respectively. The elements of the excitation electric and magnetic fields are expressed as

$$E_{u,m} = \int\limits_{T_{m_u}} \boldsymbol{f}_{m_u} \cdot \boldsymbol{E}^{inc} dS_{m_u} \tag{5.37a}$$

$$H_{u,m} = \int\limits_{T_{m_u}} \boldsymbol{f}_{m_u} \cdot \boldsymbol{H}^{inc} dS_{m_u}. \tag{5.37b}$$

For cases shown in Fig. 5.2(a) and Fig. 5.2(b), we let ($\delta = 0$, $\theta = 1$, $a = 2$, $b = u$) and ($\delta = 1$, $\theta = -1$, $a = 1$, $b = 1$) , respectively.

The scattering by the single dielectric scatterer can be considered as the special case of mixed dielectric scatterer. The matrix equation can be directly obtained

from Eq. (5.32) as

$$\begin{pmatrix} \overline{\boldsymbol{Z}}^{E_1 I_1} & \overline{\boldsymbol{C}}^{E_1 M_1} \\ \overline{\boldsymbol{D}}^{H_1 I_1} & \overline{\boldsymbol{Y}}^{H_1 M_1} \end{pmatrix} \begin{pmatrix} \boldsymbol{I}_1 \\ \boldsymbol{M}_1 \end{pmatrix} = \begin{pmatrix} \boldsymbol{E}_1 \\ \boldsymbol{H}_1 \end{pmatrix}. \tag{5.38}$$

5.2.4 AIM Implementation

The AIM algorithm given in Chapter 2 needs some modifications in order to solve the scattering problems of dielectric objects. Additional FFTs have to be carried out to account for the equivalent current densities radiating in different media. We first assume that there are a total of R media containing current densities. The dielectric scatterer is placed in a rectangular region in every medium, which will be recursively subdivided into smaller cells. A total number of W_r cells will be generated if the subdivision of the rectangular region is taken place in medium r. Each of the basis functions $\boldsymbol{f}_n$ is bounded by a cell which comprises $(M+1)^3 = 27$ grid points. Let $N_{t,r}$ denote the total number of unknowns in medium r and $N_{c,r}(w)$ denote the number of basis functions enclosed by the w_r-th cell.

In the initialization stage, the projection matrices of the current densities in all media, $\overline{\boldsymbol{\Lambda}}_r$, are computed and stored. The Green's function matrices for all media, $\overline{\boldsymbol{G}}_r$, are also computed and stored. During the matrix-vector multiplication, the current densities contained in the same medium will be projected onto the same grid points. The projection procedure is repeated for the current densities radiating in other medium. The Fourier transform of the far-zone interactions for all media are computed and subsequently transferred to the respective testing functions. Lastly, the corrected near-zone interactions of different media are added to the output. The complete algorithm is shown in Algorithm 2 in pseudocode form.

/*Initialization */
for each medium $r = 1$ *to* R **do**
  Compute $\widetilde{\boldsymbol{G}}_r = \mathrm{FFT}(\overline{\boldsymbol{G}}_r)$
  Compute $\overline{\boldsymbol{\Delta}}_r = \overline{\boldsymbol{Z}} - \overline{\boldsymbol{\Lambda}}_r\, \overline{\boldsymbol{G}}_r\, \overline{\boldsymbol{\Lambda}}_r^T$
end
/* Projection step */
for each medium $r = 1$ *to* R **do**
  Set $\widehat{\boldsymbol{I}}_r = 0$
  for each cell $p = 1$ *to* W_r **do**
    for each basis function q in cell p, $q = 1$ *to* $N_{c,r}(p)$ **do**
      $\widehat{I}_r(p) = \widehat{I}_r(p) + [\Lambda_r(p,q)]^T I_{q,r}(p)$
    end
  end
end
/* Far-zone interaction */
for each medium $r = 1$ *to* R **do**
  Compute $\widetilde{\boldsymbol{I}}_r = \mathrm{FFT}(\widehat{\boldsymbol{I}}_r)$
  Compute $\widetilde{\boldsymbol{P}}_r = \widetilde{\boldsymbol{G}}_r \cdot \widetilde{\boldsymbol{I}}_r$
  Compute $\widehat{\boldsymbol{P}}_r = \mathrm{FFT}^{-1}(\widetilde{\boldsymbol{P}}_r)$
end
for each medium $r = 1$ *to* R **do**
  Set $\boldsymbol{V}_r = 0$
  for each cell $p = 1$ *to* W_r **do**
    for each basis function q in cell p, $q = 1$ *to* $N_{c,r}(p)$ **do**
      $V_{q,r}(p) = V_{q,r}(p) + \Lambda_r(p,q)\widehat{P}_r(p)$
    end
  end
end
/* Near-zone interaction */
for each medium $r = 1$ *to* R **do**
  for each basis function $p = 1$ *to* $N_{t,r}$ **do**
    for each basis function q with, $q = 1$ *to* $N_{nz,r}(p)$ **do**
      $V_{q,r}(p) = V_{q,r}(p) + \Delta_r(p,q) I_{q,r}(p)$
    end
  end
end

Algorithm 2: AIM algorithm for solving electromagnetic scattering problems of dielectric objects characterized using the SIE.

By using the modified AIM algorithm, we can generate the near-zone matrix $\overline{\boldsymbol{Z}}^{\mathrm{near}}$ with sparsity pattern as shown in Fig. 5.3. The sparsity patterns shown in Fig. 5.3(a) and Fig. 5.3(b) are generated using a dielectric sphere and a coated

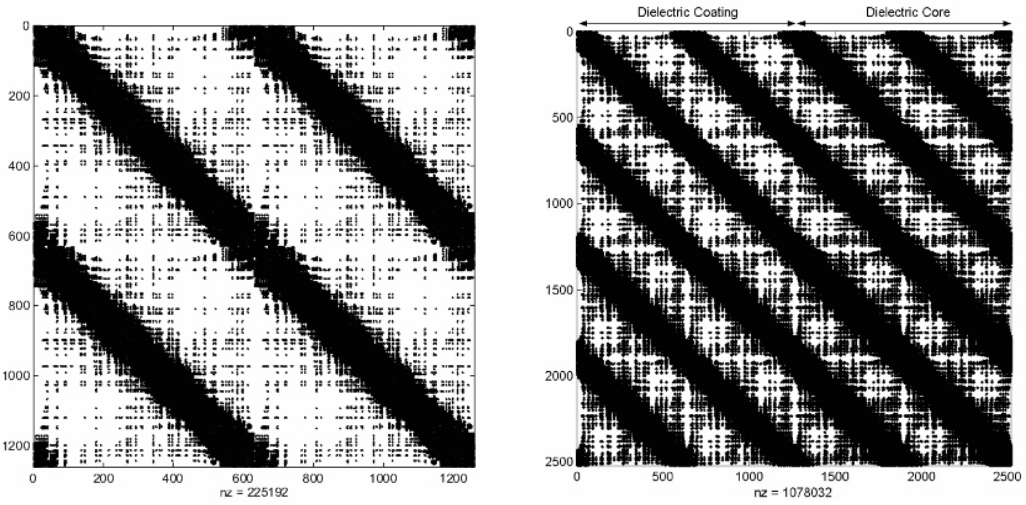

(a) Single dielectric object (b) Mixed dielectric objects

Figure 5.3: Sparsity patterns of $\overline{\boldsymbol{Z}}^{\text{near}}$ for dielectric scatterer using SIE – direct implementation.

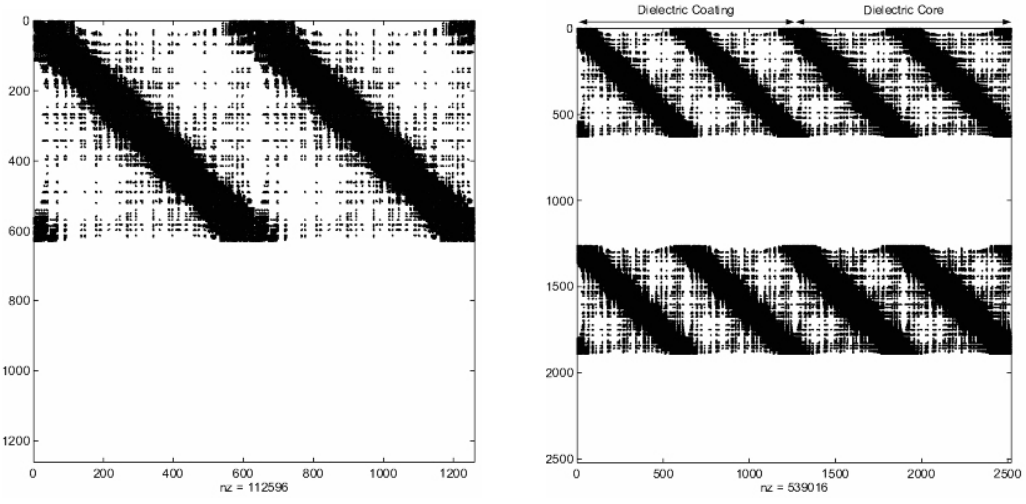

(a) Single dielectric object (b) Mixed dielectric objects

Figure 5.4: Sparsity patterns of $\overline{\boldsymbol{Z}}^{\text{near}}$ for dielectric scatterer using SIE – efficient implementation.

dielectric sphere, respectively. However, by inspecting the matrix again, we find that the sub-matrices $Y_{mn}^{H_u M_v}$ and $D_{mn}^{H_u I_v}$ need not be stored as they can be computed using sub-matrices $Z_{mn}^{E_u I_v}$ and $C_{mn}^{E_u M_v}$, respectively. Hence some savings in memory can be achieved. Fig. 5.4 shows the sparsity patterns of $\overline{\boldsymbol{Z}}^{\text{near}}$ using a more efficient implementation.

5.2.5 Numerical Results

In this section, we will present several examples to demonstrate the applicability of our AIM implementation to solve the scattering problems of mixed dielectric objects formulated using the SIE method. The first two examples are considered to validate the accuracy of AIM in solving single dielectric object and mixed dielectric objects.

The first example we consider is a dielectric sphere. The sphere has a radius of 1 m and a relative permittivity of $\epsilon_r = 1.6 - j0.4$. The bistatic RCSs of VV− and HH−polarizations are computed with 30,360 unknowns and shown in Fig. 5.5. The solutions obtained from the Mie series are also plotted for comparison. A good agreement is observed between the results.

The second example is a coated dielectric sphere. The radius of the core is 0.9 m and the thickness of the coating material is 0.1 m. The relative permittivity for the core and coating material are respectively $\epsilon_{r1} = 1.4 - j0.3$ and $\epsilon_{r2} = 1.6 - j0.8$. The bistatic RCSs for VV− and HH−polarizations are computed with 60,720 unknowns and shown in Fig. 5.6. A good agreement is also observed between our results and the solutions obtained from the Mie series.

The third example analyzed is the scattering by two dielectric spheres with different radii. The spheres are only radiatively closely coupled and the relative permittivities of the spheres are respectively $1.75 - j0.3$ and $2.25 - j0.5$. The bistatic RCSs for VV− and HH−polarizations are shown in Fig. 5.7. The RCSs of the spheres with radius of 0.4λ are compared with those in [28] and a good

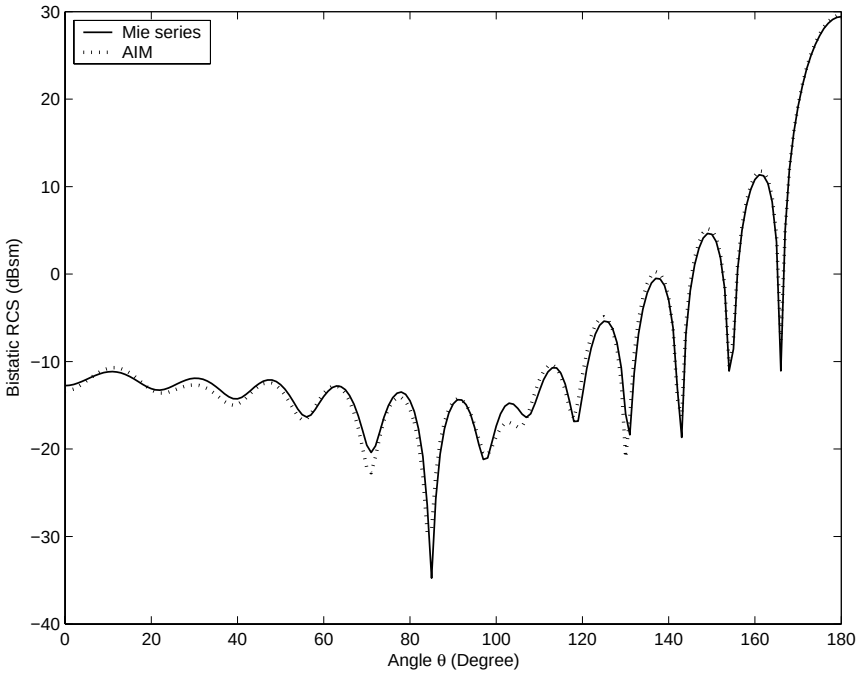

(a) VV−polarization

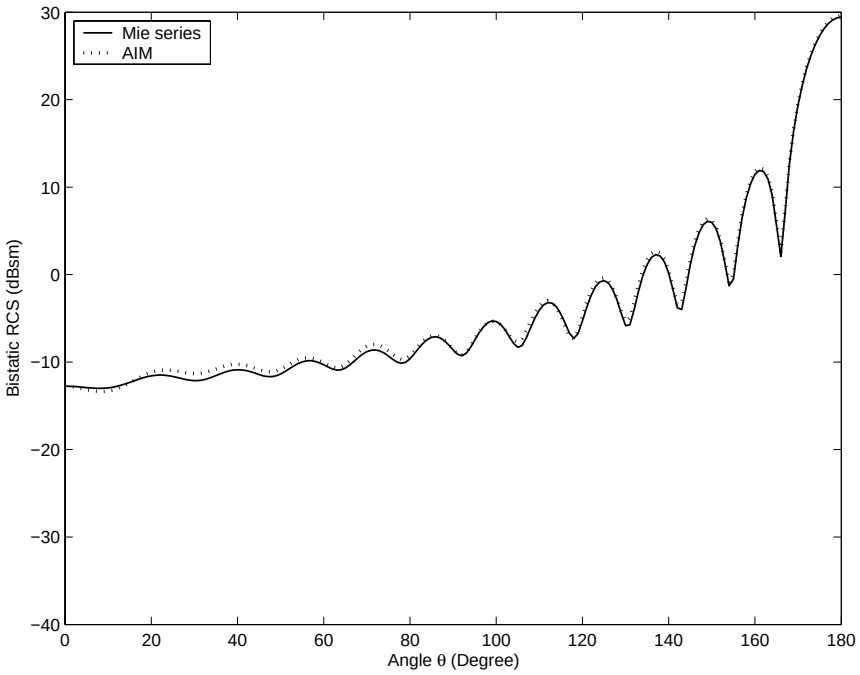

(b) HH−polarization

Figure 5.5: Bistatic RCSs of a dielectric sphere of radius 1 m at 700 MHz. (a) VV−polarization. (b) HH−polarization.

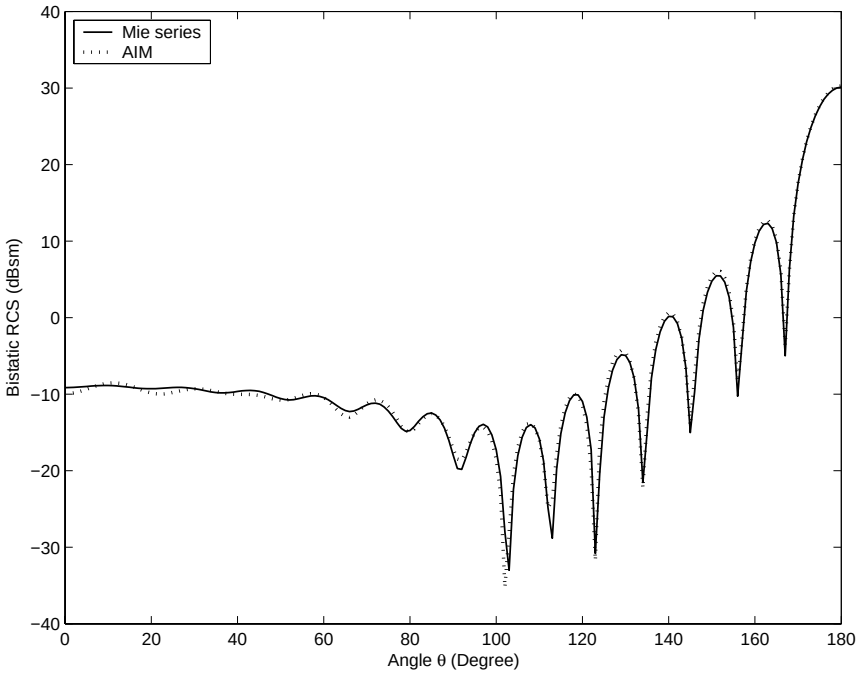

(a) VV−polarization

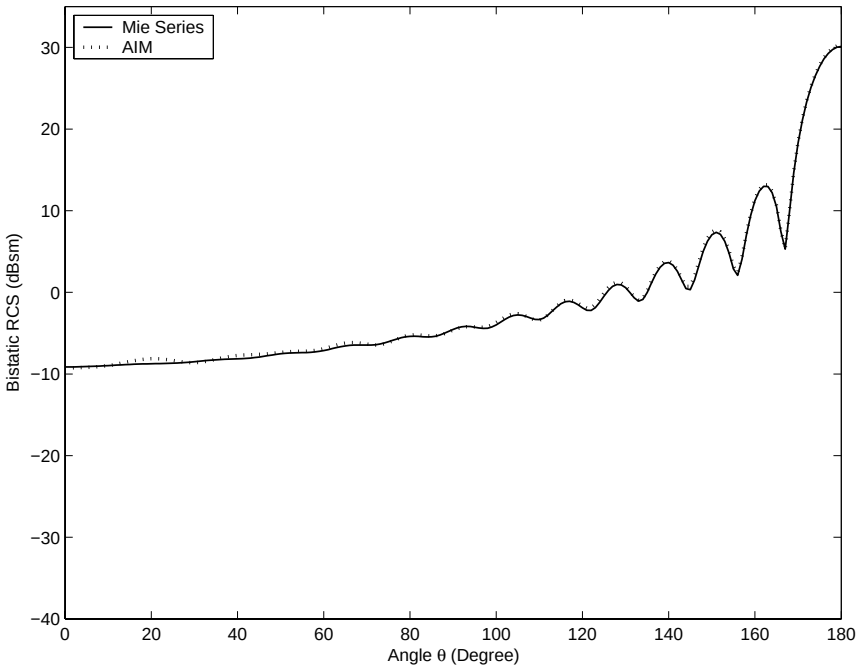

(b) HH−polarization

Figure 5.6: Bistatic RCSs of a coated dielectric sphere ($a_1 = 0.9$ m, $\epsilon_{r1} = 1.4 - j0.3$; $a_2 = 1$ m, $\epsilon_{r2} = 1.6 - j0.8$) at 750 MHz. (a) VV−polarization. (b) HH−polarization.

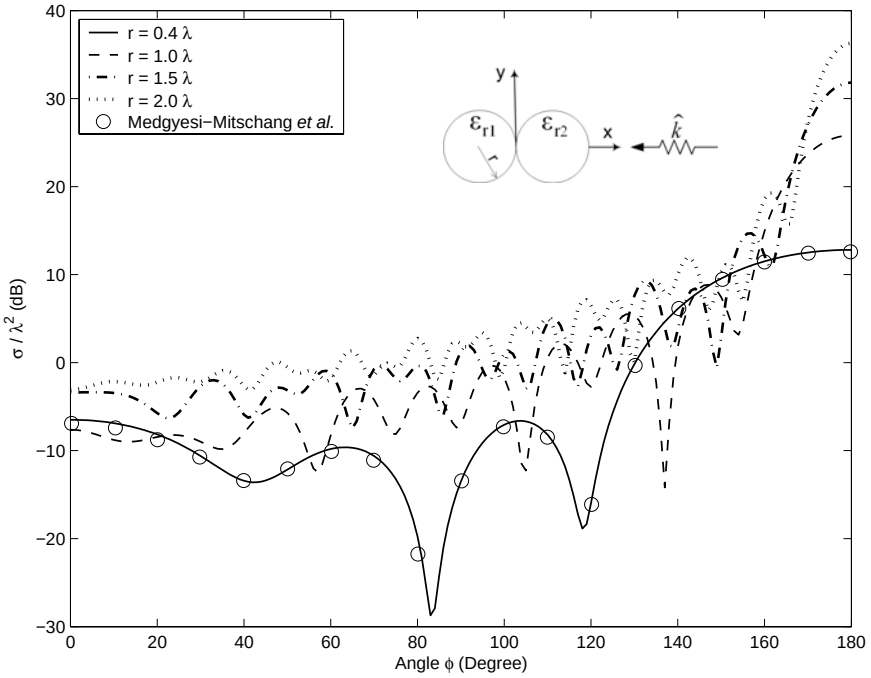

(a) VV−polarization

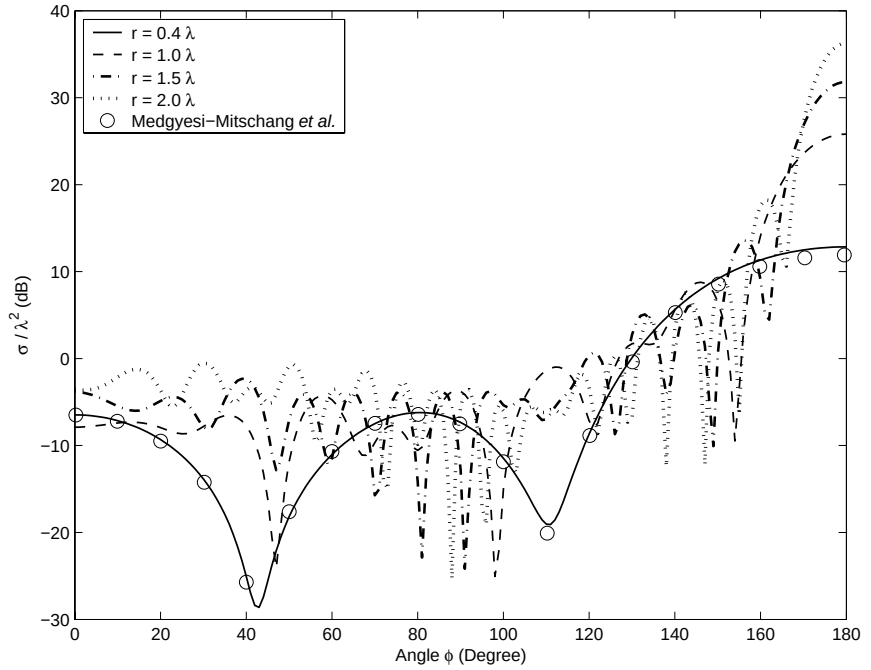

(b) HH−polarization

Figure 5.7: Bistatic RCSs of two dielectric spheres ($\epsilon_{r1} = 1.75 - j0.3$, and $\epsilon_{r2} = 2.25 - j0.5$) with different radii. (a) VV−polarization. (b) HH−polarization.

agreement is observed.

The fourth example is the scattering by nine agglomerated spheres, of which five spheres have relative permittivity $\epsilon_{r1} = 1.75 - j0.3$ and four spheres have relative permittivity $\epsilon_{r2} = 2.25 - j0.5$. Resulted from 90,060 unknowns, the bistatic RCSs for VV− and HH−polarizations are obtained and shown in Fig. 5.8.

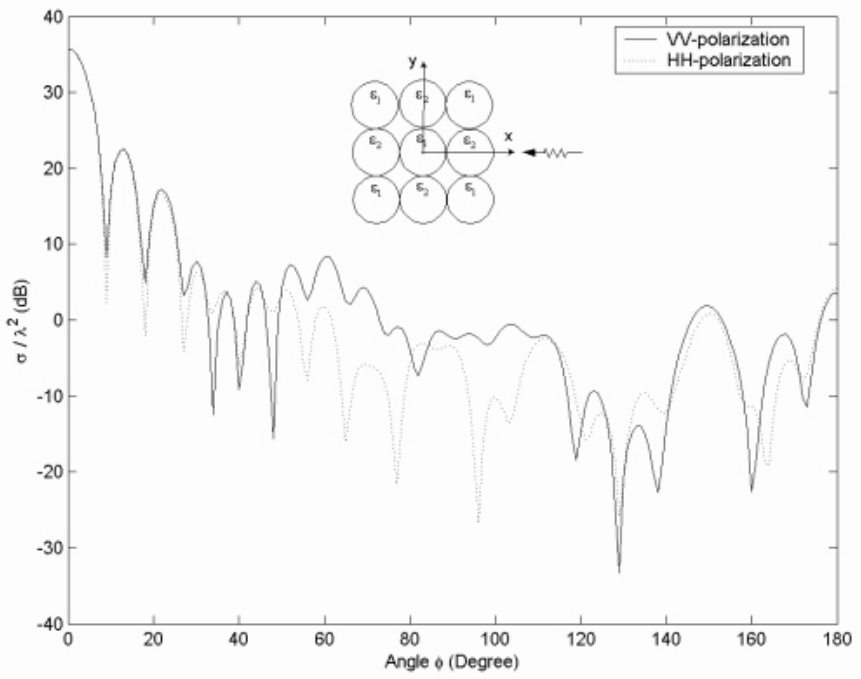

Figure 5.8: Bistatic RCSs of nine dielectric spheres, each of diameter 2λ ($\epsilon_{r1} = 1.75 - j0.3$, and $\epsilon_{r2} = 2.25 - j0.5$).

The last example we consider here is a dielectric airplane. The generic airplane model used in this example is identical to the one used in Chapter 4, except the relative permittivity $\epsilon_r = 1.44$. The monostatic RCSs for VV− and HH−polarizations are computed with 12,918 unknowns and shown in Fig. 5.9.

The comparisons between the memory used by the AIM and the estimated memory for the conventional MoM in computing the numerical examples are tabulated in Table 5.1. We find that the saving of memory is more than 90%. We also notice that more savings can be achieved when we deal with the problems with a large number of unknowns such as in Examples 2, 3 and 4. The comparisons between the CPU time used by the AIM and the estimated CPU time for the conventional

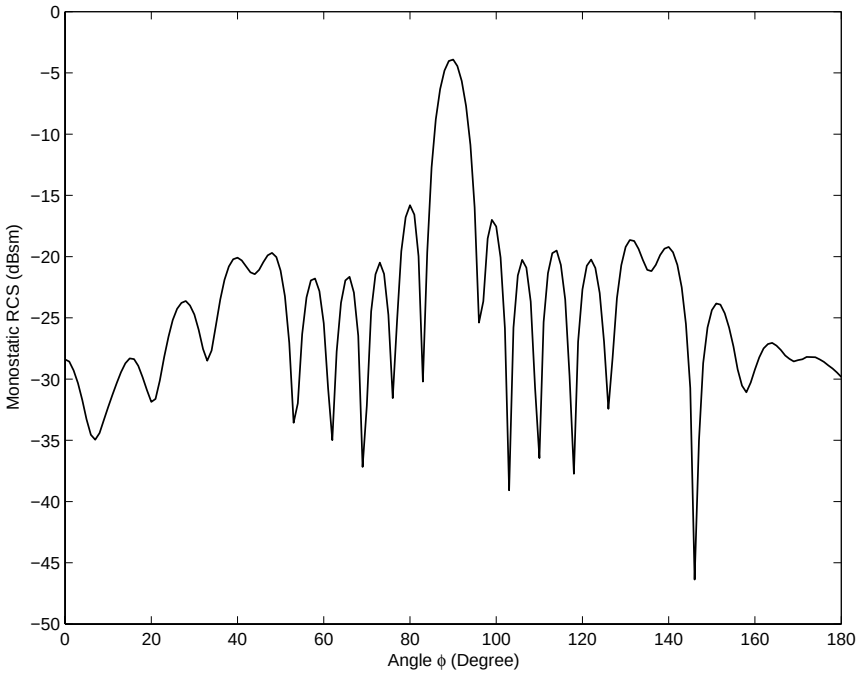

(a) VV−polarization

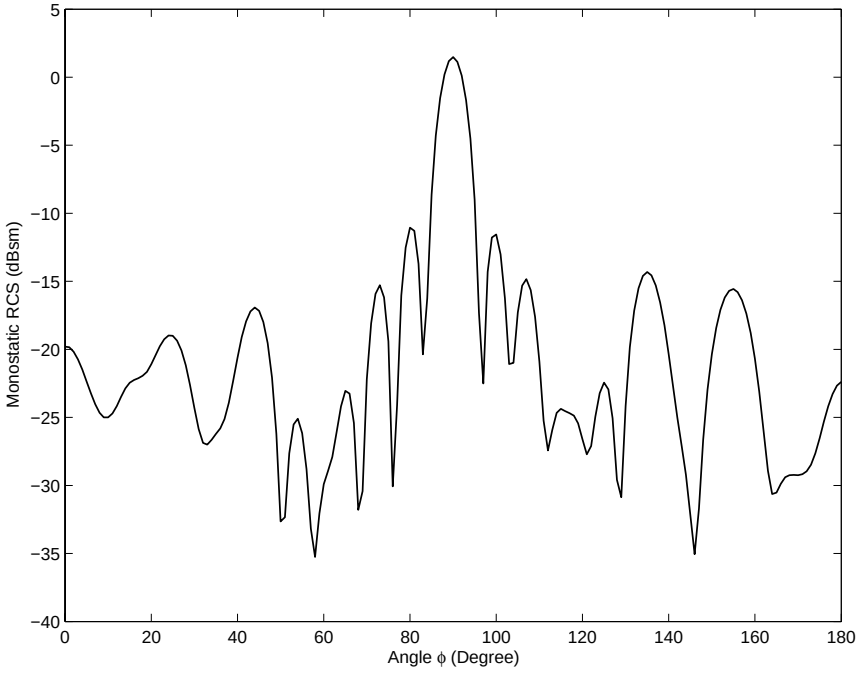

(b) HH−polarization

Figure 5.9: Monostatic RCSs of a generic dielectric airplane ($\epsilon_r = 1.6 - j0.4$). (a) VV−polarization. (b) HH−polarization.

MoM in computing the examples are shown in Table 5.2. The AIM used less CPU time to obtain the solutions of the examples and the time saving is significant for examples with a large number of unknowns such as in Examples 3 and 4.

Table 5.1: Comparison of memory requirement between the AIM and the MoM in solving electromagnetic scattering problems of dielectric objects characterized using the SIE.

Example	Unknowns, N	AIM, M_{AIM}(MB)	MoM, M_{MoM}(GB)	M_{AIM}/M_{MoM}
Dielectric sphere	30,360	145.44	6.87	2.07%
Coated dielectric sphere	60,720	164.38	27.47	0.58%
2 dielectric spheres ($r = 2\lambda$)	90,144	297.02	60.54	0.48%
9 dielectric spheres	90,060	277.49	60.43	0.45%
Dielectric airplane	12,918	114.34	1.24	8.98%

Note: 1 KB = 1,024 Bytes, 1 MB = 1,024 KB and 1 GB = 1,024 MB

Table 5.2: Comparison of CPU times between the AIM and the MoM in solving electromagnetic scattering problems of dielectric objects characterized using the SIE.

Example	Unknowns, N	AIM, T_{AIM}(sec.)	Estimated MoM, T_{MoM}(sec)
Dielectric sphere	30,360	929	1,250
Coated dielectric sphere	60,720	3,885	5,174
2 dielectric spheres ($r = 2\lambda$)	90,144	5,050	19,112
9 dielectric spheres	90,060	6,881	17,617
Dielectric airplane	12,918	1,062	1,109

5.3 Volume Integral Equation Method

The alternative method to solve the scattering problem of dielectric scatterer is to formulate the problem using the VIE method. The formulation of VIE is simple but it requires more computing resources to solve the formulated equation. The VIE is recommended when the target is a dielectric scatterer with complex material properties.

5.3.1 Formulation

Let us consider again the arbitrarily shaped 3-D dielectric scatterer in Fig. 5.1. We denote the volume enclosed by S_{21} as V and assume that it is inhomogeneous. To simplify the problem, the volume V is assumed to be non-magnetic, i.e. the permeability $\mu_2 = \mu_1$. The inhomogeneity of the dielectric material in V is described by the complex dielectric constant $\epsilon_2 = \epsilon(\boldsymbol{r}) - j\sigma(\boldsymbol{r})/\omega$ where $\epsilon(\boldsymbol{r})$ and $\sigma(\bar{r})$ are permittivity and conductivity, respectively, at $\boldsymbol{r}$.

By invoking the volume equivalence principle in the dielectric region V, the equivalent volume current densities

$$\boldsymbol{J}_V = j\omega\left(\epsilon_2 - \epsilon_1\right)\boldsymbol{E} \tag{5.39}$$

$$\boldsymbol{K}_V = j\omega\left(\mu_2 - \mu_1\right)\boldsymbol{H} = 0, \tag{5.40}$$

where $\boldsymbol{E}$ and $\boldsymbol{H}$ are the total electric and magnetic fields, respectively. The scattered electric field $\boldsymbol{E}^{sca}$ produced by the induced volume current density are given by

$$\boldsymbol{E}^{sca}(\boldsymbol{r}) = -\eta_1 \mathcal{L}_1 \boldsymbol{J}_V. \tag{5.41}$$

Substituting Eq. (5.41) into (5.39), we obtain

$$\boldsymbol{E}^{inc}(\boldsymbol{r}) = \frac{1}{j\omega(\epsilon_2 - \epsilon_1)}\boldsymbol{J}_V + \eta_1 \mathcal{L}_1 \boldsymbol{J}_V. \tag{5.42}$$

5.3.2 Method of Moments

In solving the VIE using the MoM, the equivalent current density is not directly used as the unknown quantity to be determined. Instead, the electric flux density $\boldsymbol{D}$ is used as the unknown quantity. It is used because the continuity of the normal components of $\boldsymbol{D}$ can be ensured by using proper basis functions.

The volume of dielectric material is discretized into tetrahedral elements. Tetra-

hedral elements are used because of their flexibility to model arbitrarily shaped 3-D object. In addition, it is convenient to use tetrahedral elements to represent the inhomogeneity of the volume. The basis functions suitable for tetrahedral elements are the SWG basis functions [29]. The features of SWG basis functions, such as the continuity of the electric flux density normal to the interior face, make them suitable to be implemented in the volume integral equation.

In the volume, the electric flux density $\boldsymbol{D}$ is expanded using the SWG basis functions $\boldsymbol{f}_n$ as

$$\boldsymbol{D} = \epsilon_2(\boldsymbol{r})\,\boldsymbol{E} = \sum_{n=1}^{N_V} I_n \boldsymbol{f}_n \tag{5.43}$$

where the I_n denotes the coefficients for the basis functions. By use of Eq. (5.39), the induced volume current is expressed below:

$$\boldsymbol{J}_V = j\omega \sum_{n=1}^{N_V} \frac{\epsilon_2(\boldsymbol{r}) - \epsilon_1}{\epsilon_2(\boldsymbol{r})} I_n \boldsymbol{f}_n = j\omega \sum_{n=1}^{N_V} \kappa(\boldsymbol{r})\, I_n \boldsymbol{f}_n \tag{5.44}$$

where $\kappa(\boldsymbol{r}) = (\epsilon_2(\boldsymbol{r}) - \epsilon_1)/\epsilon_2(\boldsymbol{r})$ is the contrast ratio [29].

By applying the Galerkin's testing procedure, the discretized integral equation can be converted into a matrix equation as

$$\overline{\boldsymbol{Z}}\boldsymbol{I} = \boldsymbol{\mathcal{V}} \tag{5.45}$$

where the vectors $\boldsymbol{I}$ represents the coefficients of volume current density. The excitation vector $\boldsymbol{\mathcal{V}}$ can be computed using

$$\mathcal{V}_m = \int_{V_m} \boldsymbol{f}_m \cdot \boldsymbol{E}^{inc}(\boldsymbol{r}')\, dV' \tag{5.46}$$

while the elements of the impedance matrix $\overline{\boldsymbol{Z}}$ can be computed using

$$\begin{aligned} Z_{mn} = & \int_{V_m} \frac{\boldsymbol{f}_m \cdot \boldsymbol{f}_n}{\epsilon_2} dV - \omega k_1 \eta_1 \int_{V_m} \boldsymbol{f}_m \cdot \left[\int_{V_n} \kappa \boldsymbol{f}_n g(\boldsymbol{r}, \boldsymbol{r}') dV' + \right. \\ & \left. \frac{\boldsymbol{\nabla}}{k_1^2} \int_{V_n} \boldsymbol{\nabla}' \cdot (\kappa \boldsymbol{f}_n)\, g(\boldsymbol{r}, \boldsymbol{r}') dV' \right] dV. \end{aligned} \tag{5.47}$$

The κ is a constant value within the tetrahedron and it can be taken out from the integration. Besides, we can also rewrite

$$\nabla \cdot (\kappa \boldsymbol{f}_n) = \kappa \nabla \cdot \boldsymbol{f}_n + \nabla \kappa \cdot \boldsymbol{f}_n \tag{5.48}$$

and the second term is given by [29] as

$$\boldsymbol{\nabla} \kappa \cdot \boldsymbol{f}_n = \begin{cases} I_n \left(\kappa_n^+ - \kappa_n^- \right), & \text{on the common facet;} \\ 0, & \text{elsewhere.} \end{cases} \tag{5.49}$$

5.3.3 AIM Implementation

In the VIE formulation, the coefficients of the electric flux density (or the related equivalent volume current density) are the unknowns to be determined. The volume scatterer is first contained in a rectangular region and then recursively subdivided into a total of W cells. Every basis function is bounded by a cell which comprises $(M+1)^3 = 27$ grid points. Let N_t^V denotes the total number of volume basis functions, and $N_c^V(w)$ denote the total number of volume basis functions contained in the w-th cell.

In the initialization stage, the projection matrix of equivalent volume current density, $\overline{\boldsymbol{\Lambda}}$, is computed and stored. However it is noted that the projection scheme for VIE is different from the projection scheme for SIE, which the equivalent volume current density is projected together with the contrast ratio, κ. Since the equivalent current density radiates only in the background medium, only one Green's function matrix is required. During the matrix-vector multiplication, the current density will be first projected to the surrounding grid points. Then the far-zone interactions are computed by convolving the grid currents with the Green's function matrix and subsequently transferred back to the respective testing functions. Lastly, the corrected near-zone interactions are added to the output. The complete modified AIM algorithm for the VIE is shown in Algorithm 3.

/*Initialization */
Compute $\widetilde{\overline{\boldsymbol{G}}} = \mathrm{FFT}(\overline{\boldsymbol{G}})$
Compute $\overline{\boldsymbol{\Delta}} = \overline{\boldsymbol{Z}} - \overline{\boldsymbol{\Lambda}}\ \overline{\boldsymbol{G}}\ \overline{\boldsymbol{\Lambda}}^T$
/* Projection step */
Set $\widehat{\boldsymbol{I}} = 0$
for each cell $p = 1$ *to* W **do**
  for each basis function f_q in cell p, $q = 1$ *to* $N_c(p)$ **do**
    $\widehat{I}(p) = \widehat{I}(p) + [\Lambda(p,q)]^T I_q(p)$
  end
end
/* Far-zone interaction */
Compute $\widetilde{\boldsymbol{I}} = \mathrm{FFT}(\widehat{\boldsymbol{I}})$
Compute $\widetilde{\boldsymbol{P}} = \widetilde{\boldsymbol{G}} \cdot \widetilde{\boldsymbol{I}}$
Compute $\widehat{\boldsymbol{P}} = \mathrm{FFT}^{-1}(\widetilde{\boldsymbol{P}})$
Set $\boldsymbol{\mathcal{V}} = 0$
for each cell $p = 1$ *to* W **do**
  for each basis function f_q in cell p, $q = 1$ *to* $N_c(p)$ **do**
    $\mathcal{V}_q(p) = \mathcal{V}_q(p) + \Lambda(p,q)\widehat{P}(p)$
  end
end
/* Near-zone interaction */
for each basis function $f_p = 1$ *to* N_t **do**
  for each basis function f_q^V with, $q = 1$ *to* $N_{nz}(p)$ **do**
    $\mathcal{V}_q(p) = \mathcal{V}_q(p) + \Delta(p,q) I_q^V(p)$
  end
end

Algorithm 3: AIM algorithm for solving electromagnetic scattering problems of dielectric objects characterized using the VIE.

Fig. 5.10(a) depicts the near-zone matrix $\overline{\boldsymbol{Z}}^{\mathrm{near}}$ generated by the modified AIM for the scattering problem formulated characterized using the VIE method. The sparsity pattern is generated using a dielectric sphere. In order to clearly show the saving achieved by the AIM, we show the reordered $\overline{\boldsymbol{Z}}^{\mathrm{near}}$ in Fig. 5.10(b). We observe that the $\overline{\boldsymbol{Z}}^{\mathrm{near}}$ for the VIE method is more densely populated than the $\overline{\boldsymbol{Z}}^{\mathrm{near}}$ generated by the SIE method.

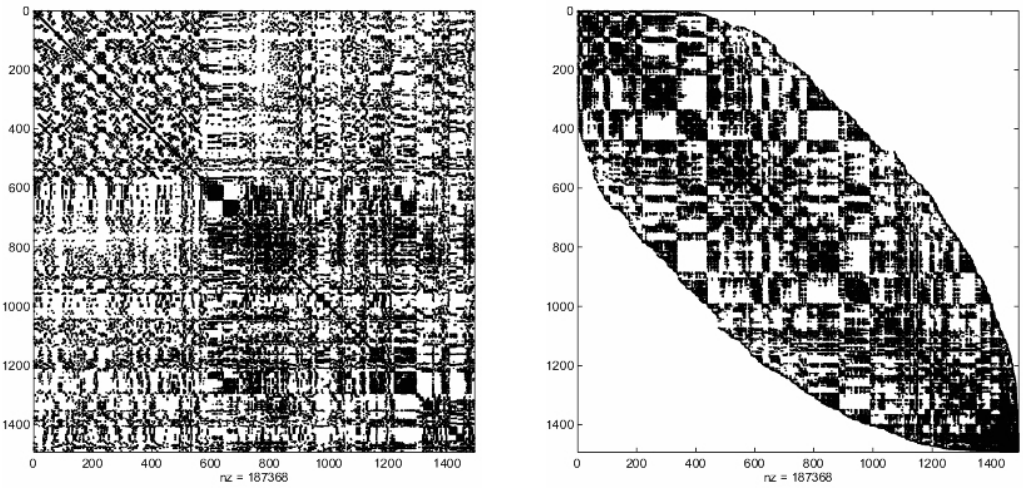

(a) Actual sparsity pattern (b) Reordered sparsity pattern

Figure 5.10: Sparsity patterns of $\overline{\boldsymbol{Z}}^{\text{near}}$ for dielectric scatterer using the VIE.

5.3.4 Numerical Results

In this section, three numerical examples will be presented to demonstrate the applicability of our AIM implementation to solve the scattering problem of dielectric objects formulated using the VIE method. The first example is to validate the accuracy of our AIM code in solving scattering problems of dielectric objects. Thus we consider a dielectric spherical shell. The spherical shell has an inner radius of 0.8 m and a thickness of 0.2 m. The relative permittivity of the dielectric material is $\epsilon_r = 1.6 - j0.8$. The bistatic RCSs of VV−polarization are computed with 28,498 unknowns and shown in Fig. 5.11. The solutions obtained from the Mie series are also plotted for comparison. A good agreement is observed between the results.

The second example is a dielectric sphere consisting of four dielectric materials. The dielectric sphere is shown in Fig. 5.12 where the radius of the core, $r_i = 1.0$ m and the thickness of the coating material is 0.2 m. The relative permittivities of the dielectric materials are $\epsilon_{r1} = 4.0 - j1.0$, $\epsilon_{r2} = 2.0 - j1.0$, $\epsilon_{r3} = 2.0$ and $\epsilon_{r4} = 1.44 - j0.6$. The bistatic RCSs of VV− and HH− polarizations are computed with 18,528 unknowns and shown in Fig. 5.13. The bistatic RCSs of VV−polarization are compared with the result in [88] and a good agreement is observed.

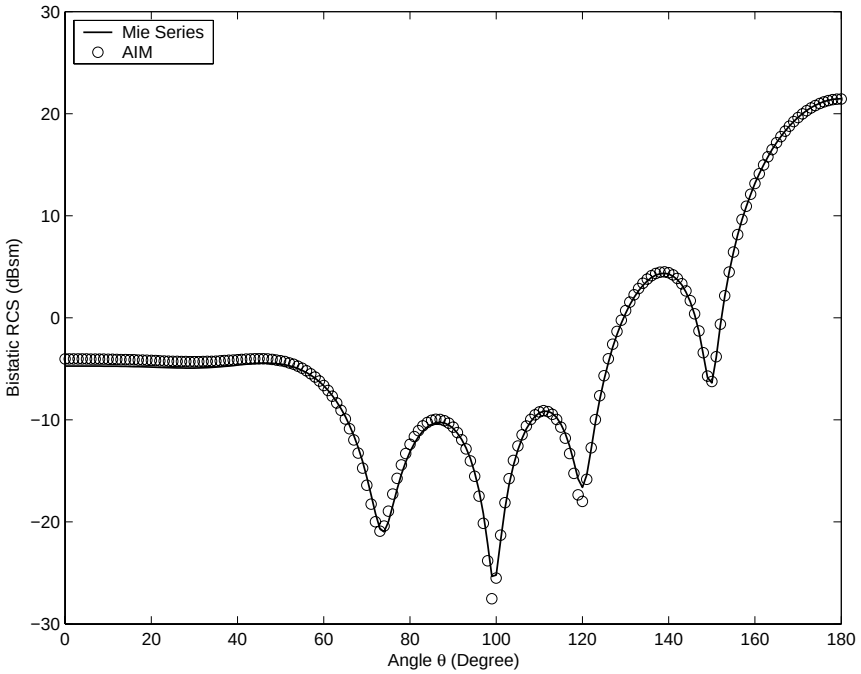

Figure 5.11: Bistatic RCSs of a dielectric spherical shell with inner radius 0.8 m and thickness of 0.2 m at 300 MHz.

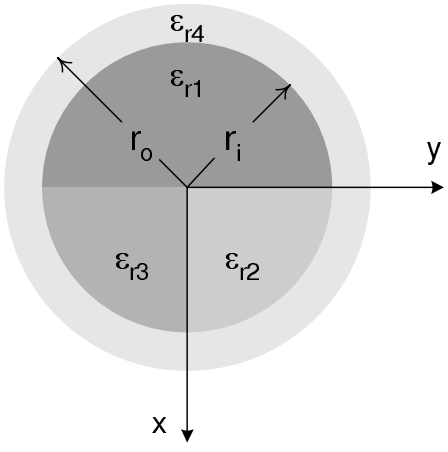

Figure 5.12: A coated dielectric sphere with four different dielectric materials (r_i = 0.8 m, r_o = 1.0 m, $\epsilon_{r1} = 4.0 - j1.0$, $\epsilon_{r2} = 2.0 - j1.0$, $\epsilon_{r3} = 2.0$ and $\epsilon_{r4} = 1.44 - j0.6$).

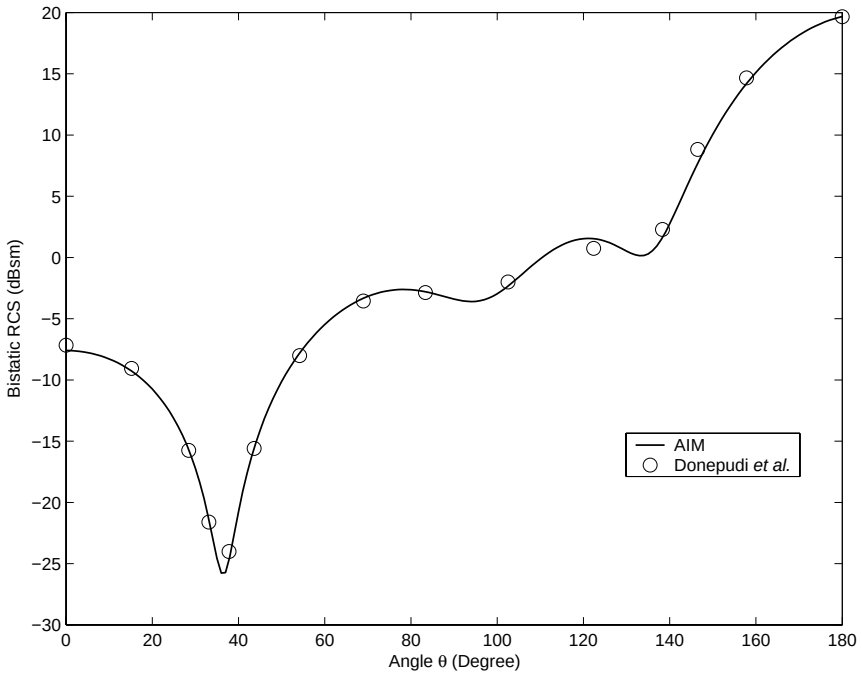

(a) VV−polarization

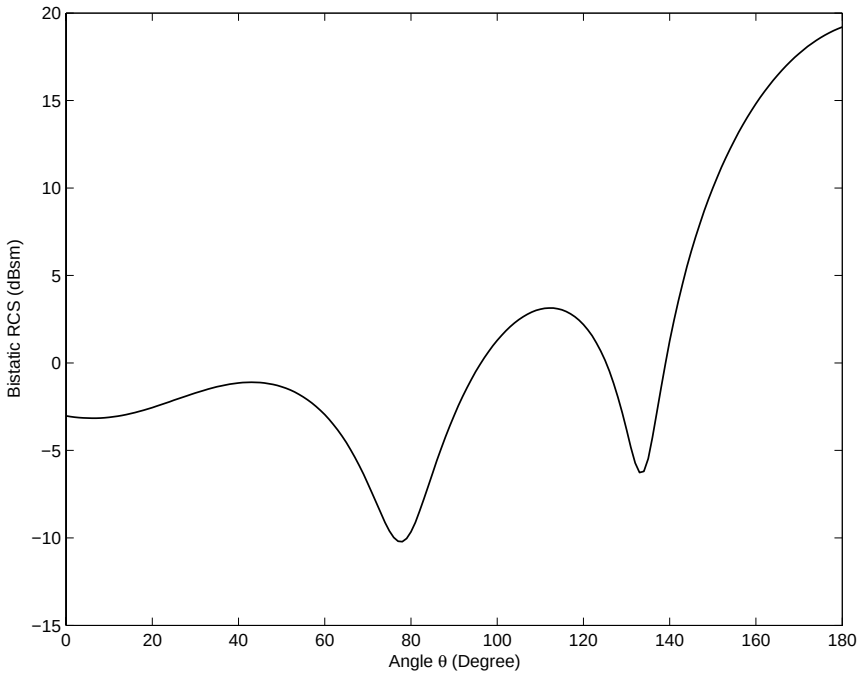

(b) HH−polarization

Figure 5.13: Bistatic RCSs of a coated dielectric sphere with four different dielectric materials at 300 MHz. (a) VV−polarization. (b) HH−polarization.

The last example analyzed is the scattering of a periodic dielectric slab. The geometry of the dielectric slab is shown in Fig. 5.14 where $h = 1.4324$ m, $d_1 = d_2 = 0.4181$ m and $L = 5.02$ m. The relative permittivities are $\epsilon_{r1} = 2.56$ and $\epsilon_{r2} = 1.44$. The bistatic RCSs for VV− and HH−polarizations are computed with 176,187 unknowns and shown in Fig. 5.15. The bistatic RCSs of HH−polarization are compared with the result published in [89] and a good agreement is observed.

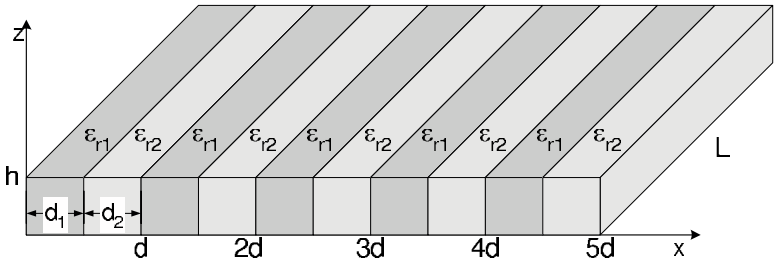

Figure 5.14: A five-period periodic dielectric slab ($h = 1.4324$ m, $d_1 = d_2 = 0.4181$ m, $L = 5.02$ m, $\epsilon_{r1} = 2.56$ and $\epsilon_{r2} = 1.44$).

The comparisons between the memory used by the AIM and the estimated memory for the conventional MoM in computing the numerical examples are tabulated in Table 5.3. We find that the saving of memory is more than 90%. We observe that without the AIM, it is almost impossible to solve scattering problem of dielectric objects characterized using the VIE due to the huge memory requirement. We also observe that solving the scattering problem by using the VIE will involve a huge number of unknowns, even for a simple structure such as Example 1. Hence we shall avoid to use VIE for piecewise homogeneous material objects as the VIE requires more matrix storage as compared to the SIE.

The comparisons between the CPU time taken by the AIM to compute the examples and the estimated CPU time by the MoM are shown in Table 5.4. Similarly to the examples in the previous section, we also find that the time saving is great for a problem with a large number of unknowns, especially in Example 3. We have so far achieved saving in memory requirement and CPU time in solving scattering problems of dielectric object characterized by the VIE.

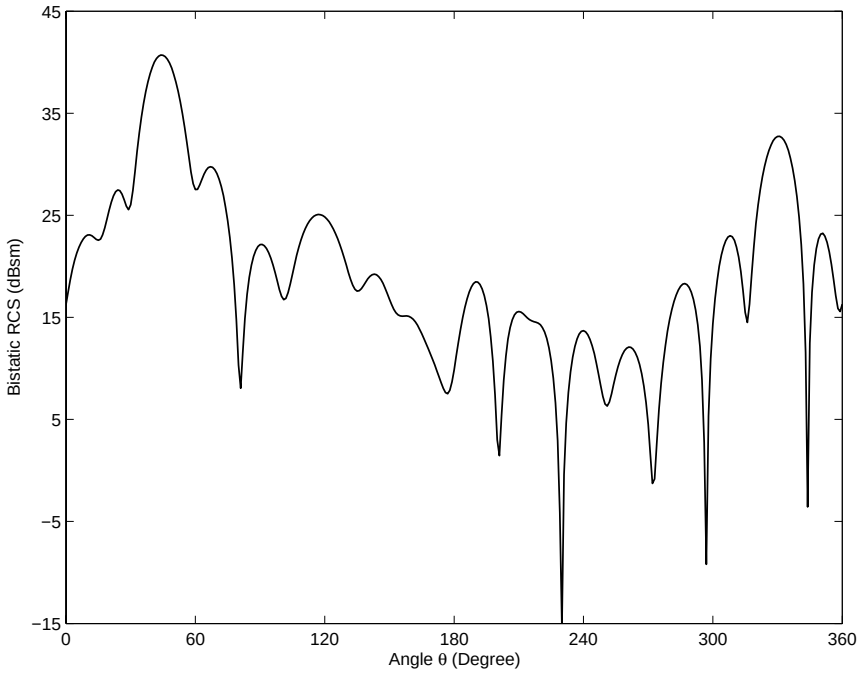

(a) VV−polarization

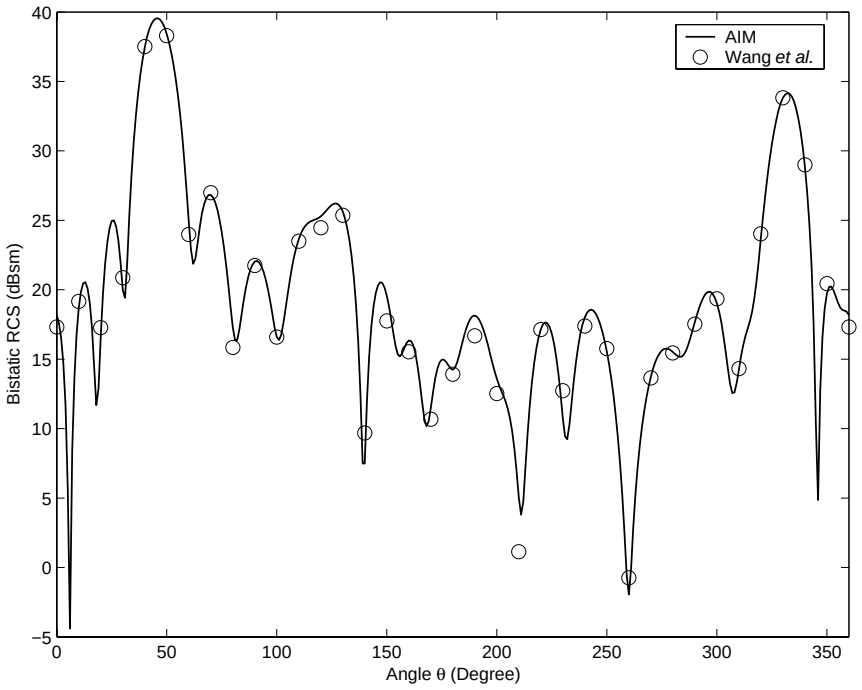

(b) HH−polarization

Figure 5.15: Bistatic RCS of a periodic dielectric slab with relative permittivities $\epsilon_{r1} = 2.56$, and $\epsilon_{r2} = 1.44$. (a) VV−polarization. (b) HH−polarization.

Table 5.3: Comparison of memory requirement between the AIM and the MoM in solving electromagnetic scattering problems of dielectric objects characterized using the VIE.

Example	Unknowns, N	AIM, M_{AIM}(MB)	MoM, M_{MoM}(GB)	M_{AIM}/M_{MoM}
Dielectric spherical shell	28,498	117.08	6.05	1.89%
Coated dielectric sphere	18,528	192.27	2.56	7.34%
Periodic dielectric slab	176,187	536.88	231.28	0.23%

Note: 1 KB = 1,024 Bytes, 1 MB = 1,024 KB and 1 GB = 1,024 MB

Table 5.4: Comparison of CPU time between the AIM and the MoM in solving electromagnetic scattering problems of dielectric objects characterized using the VIE.

Example	Unknowns, N	AIM, T_{AIM}(sec)	Estimated MoM, T_{MoM}(sec)
Dielectric spherical shell	28,498	62	400
Coated dielectric sphere	18,528	156	297
Periodic dielectric slab	176,187	1,920	137,826

Chapter 6

Fast Solution to Scattering Problems of Composite Dielectric and Conducting Objects

6.1 Introduction

The scattering problem of composite dielectric and conducting objects can be formulated using the surface integral equation (SIE) method [28, 33] or the hybrid volume-surface integral equation (VSIE) method [34, 35]. The scattering by conducting objects is usually characterized using the SIE, but the choice of using SIE or VIE for dielectric object depends on its inhomogeneity. For an object with arbitrary inhomogeneity, solving the scattering problem using the VIE method will be more advantageous than the SIE method, as the latter requires the integral equations to be formulated in every dielectric region. However, if the object consists of only piecewise homogeneous dielectric materials, then the SIE formulation is generally preferred.

As mentioned in the previous chapter, solving scattering problem involving of dielectric objects is very costly. However the AIM can be used to alleviate the huge

matrix storage requirement and high computational complexity problems facing by the conventional MoM. In this chapter, the AIM solution to scattering problems of composite conducting and dielectric objects will be presented. We will first carry out the formulation by using the SIE method and solve the resultant matrix equation by AIM [54]. Subsequently, we will use the AIM to analyze the scattering problem characterized using the VSIE method [55].

6.2 Surface Integral Equation Method

6.2.1 Formulation

In this section, we will consider two sets of configurations, i.e. coated object and discrete objects. We will only carry out the formulation for coated object and subsequently deduce the formulation for discrete objects. Consider a coated object with a metallic core as shown in Fig. 6.1(a) and the material properties of the coating layer are characterized respectively by permittivity ϵ_2 and permeability μ_2. The coated object is embedded in an isotropic and homogeneous background medium which is characterized by material properties ϵ_1 and μ_1. The interface between media i and j is denoted as S_{ji}. The unit vector normal to S_{ji} and pointing toward the medium i is denoted as $\widehat{\boldsymbol{n}}_{ji}$. The coated object is illuminated by an incident wave $\boldsymbol{E}^{inc}$, which is generated by impressed source in the background medium.

To describe the problem, a mathematical surface is constructed on the surface of the coating material. By using the surface equivalence principle, the equivalent electric and magnetic current densities flowing on the fictitious surface are

$$\boldsymbol{J}_{21} = \widehat{\boldsymbol{n}} \times \boldsymbol{H}_1 \tag{6.1}$$

$$\boldsymbol{K}_{21} = \boldsymbol{E}_1 \times \widehat{\boldsymbol{n}}, \tag{6.2}$$

where the $\boldsymbol{E}_1$ and $\boldsymbol{H}_1$ are respectively the total electric and magnetic fields in the

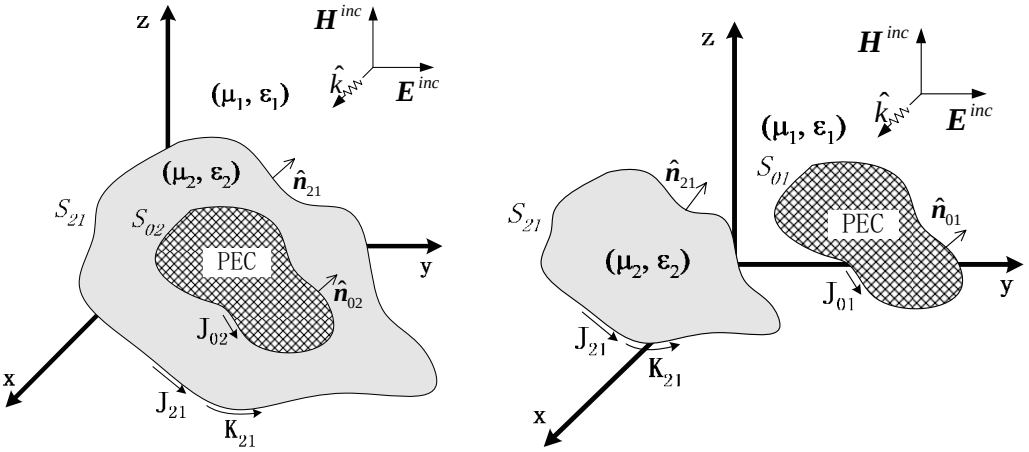

(a) Coated object (b) Discrete objects

Figure 6.1: Geometry of a dielectric and perfectly conducting scatterers embedded in an isotropic homogeneous medium.

background medium. We also construct another mathematical surface that coincides with the surface of the metallic core, S_{02}. By invoking the surface equivalence principle and using the boundary conditions on the conductor, the second set of equivalent current densities can be obtained as

$$\boldsymbol{J}_{02} = \widehat{\boldsymbol{n}} \times \boldsymbol{H}_2 \tag{6.3}$$

$$\boldsymbol{K}_{02} = \boldsymbol{E}_2 \times \widehat{\boldsymbol{n}} = 0. \tag{6.4}$$

Outside the S_{21}, the first set of equivalent current densities are radiating in an unbounded background medium, hence the source-field relationship can be obtained by using Eq. (2.6),

$$-\boldsymbol{K}_{21} + \widehat{\boldsymbol{n}}_{21} \times \eta_1 \mathcal{L}_1 \boldsymbol{J}_{21} + \widehat{\boldsymbol{n}}_{21} \times \mathcal{M}_1 \boldsymbol{K}_{21} = \widehat{\boldsymbol{n}}_{21} \times \boldsymbol{E}^{inc} \tag{6.5}$$

$$\boldsymbol{J}_{21} - \widehat{\boldsymbol{n}}_{21} \times \mathcal{M}_1 \boldsymbol{J}_{21} + \widehat{\boldsymbol{n}}_{21} \times \frac{1}{\eta_1} \mathcal{L}_1 \boldsymbol{K}_{21} = \widehat{\boldsymbol{n}}_{21} \times \boldsymbol{H}^{inc}. \tag{6.6}$$

Inside the S_{21}, both sets of equivalent current densities are radiating in an unbounded medium characterized by (μ_2, ϵ_2), hence we have

$$\boldsymbol{K}_{21} + \widehat{\boldsymbol{n}}_{21} \times \eta_2 \mathcal{L}_2 \boldsymbol{J}_{21} + \widehat{\boldsymbol{n}}_{21} \times \mathcal{M}_2 \boldsymbol{K}_{21} = \widehat{\boldsymbol{n}}_{21} \times \eta_2 \mathcal{L}_2 \boldsymbol{J}_{02} \tag{6.7}$$

$$-\boldsymbol{J}_{21} - \widehat{\boldsymbol{n}}_{21} \times \mathcal{M}_2 \boldsymbol{J}_{21} + \widehat{\boldsymbol{n}}_{21} \times \frac{1}{\eta_2} \mathcal{L}_2 \boldsymbol{K}_{21} = -\widehat{\boldsymbol{n}}_{21} \times \mathcal{M}_2 \boldsymbol{J}_{02}. \quad (6.8)$$

And on the surface of the S_{02}, we have

$$\widehat{\boldsymbol{n}}_{02} \times \eta_2 \mathcal{L}_2 \boldsymbol{J}_{02} = \widehat{\boldsymbol{n}}_{02} \times \eta_2 \mathcal{L}_2 \boldsymbol{J}_{21} + \widehat{\boldsymbol{n}}_{02} \times \mathcal{M}_2 \boldsymbol{K}_{21} \quad (6.9)$$

$$\boldsymbol{J}_{02} - \widehat{\boldsymbol{n}}_{02} \times \mathcal{M}_2 \boldsymbol{J}_{02} = -\widehat{\boldsymbol{n}}_{02} \times \mathcal{M}_2 \boldsymbol{J}_{21} + \widehat{\boldsymbol{n}}_{02} \times \frac{1}{\eta_2} \mathcal{L}_2 \boldsymbol{K}_{21}. \quad (6.10)$$

By using the PMCHWT formulation [22–24], the EFIE and MFIE in Eqs. (6.5)–(6.8) can be combined to become

$$\begin{aligned} \widehat{\boldsymbol{n}}_{21} \times \boldsymbol{E}^{inc} &= \widehat{\boldsymbol{n}}_{21} \times (\eta_1 \mathcal{L}_1 + \eta_2 \mathcal{L}_2) \boldsymbol{J}_{21} + \widehat{\boldsymbol{n}}_{21} \times (\mathcal{M}_1 + \mathcal{M}_2) \boldsymbol{K}_{21} \\ &\quad - \widehat{\boldsymbol{n}}_{21} \times \eta_2 \mathcal{L}_2 \boldsymbol{J}_{02} \quad (6.11) \\ \widehat{\boldsymbol{n}}_{21} \times \boldsymbol{H}^{inc} &= -\widehat{\boldsymbol{n}}_{21} \times (\mathcal{M}_1 + \mathcal{M}_2) \boldsymbol{J}_{21} + \widehat{\boldsymbol{n}}_{21} \times (\frac{1}{\eta_1} \mathcal{L}_1 + \frac{1}{\eta_2} \mathcal{L}_2) \boldsymbol{K}_{21} \\ &\quad + \widehat{\boldsymbol{n}}_{21} \times \mathcal{M}_2 \boldsymbol{J}_{02}. \quad (6.12) \end{aligned}$$

Now we consider the conducting scatterer placed beside a discrete dielectric scatterer as shown in Fig. 6.1(b). Following the same procedure, the integral equations on the surface of the discrete dielectric scatterer are

$$\begin{aligned} \widehat{\boldsymbol{n}}_{21} \times \boldsymbol{E}^{inc} &= \widehat{\boldsymbol{n}}_{21} \times (\eta_1 \mathcal{L}_1 + \eta_2 \mathcal{L}_2) \boldsymbol{J}_{21} + \widehat{\boldsymbol{n}}_{21} \times (\mathcal{M}_1 + \mathcal{M}_2) \boldsymbol{K}_{21} \\ &\quad + \widehat{\boldsymbol{n}}_{21} \times \eta_1 \mathcal{L}_1 \boldsymbol{J}_{01} \quad (6.13) \\ \widehat{\boldsymbol{n}}_{21} \times \boldsymbol{H}^{inc} &= -\widehat{\boldsymbol{n}}_{21} \times (\mathcal{M}_1 + \mathcal{M}_2) \boldsymbol{J}_{21} + \widehat{\boldsymbol{n}}_{21} \times (\frac{1}{\eta_1} \mathcal{L}_1 + \frac{1}{\eta_2} \mathcal{L}_2) \boldsymbol{K}_{21} \\ &\quad - \widehat{\boldsymbol{n}}_{21} \times \mathcal{M}_1 \boldsymbol{J}_{01}. \quad (6.14) \end{aligned}$$

And the integral equations on the surface of the discrete conducting scatterer are

$$\widehat{\boldsymbol{n}}_{01} \times \boldsymbol{E}^{inc} = \widehat{\boldsymbol{n}}_{01} \times \eta_1 \mathcal{L}_1 \boldsymbol{J}_{01} + \widehat{\boldsymbol{n}}_{01} \times \eta_1 \mathcal{L}_1 \boldsymbol{J}_{21} + \widehat{\boldsymbol{n}}_{01} \times \mathcal{M}_1 \boldsymbol{K}_{21} \quad (6.15)$$

$$\widehat{\boldsymbol{n}}_{01} \times \boldsymbol{H}^{inc} = \boldsymbol{J}_{01} - \widehat{\boldsymbol{n}}_{01} \times \mathcal{M}_1 \boldsymbol{J}_{01} - \widehat{\boldsymbol{n}}_{01} \times \mathcal{M}_1 \boldsymbol{J}_{21} + \widehat{\boldsymbol{n}}_{01} \times \frac{1}{\eta_1} \mathcal{L}_1 \boldsymbol{K}_{21}. \quad (6.16)$$

6.2.2 Method of Moments

The integral equations formulated in the previous subsection are discretized using the method of moments. The arbitrarily shaped 3-D objects are modeled using triangular patches. Hence it is convenient to use the RWG basis functions $\boldsymbol{f}_n$ to expand the equivalent surface electric and magnetic current densities $\boldsymbol{J}_{ji}$ and $\boldsymbol{K}_{ji}$ as follows:

$$\boldsymbol{J}_{ji} = \sum I_{n_j} \boldsymbol{f}_{n_j} \tag{6.17}$$

$$\boldsymbol{K}_{ji} = \sum M_{n_j} \boldsymbol{f}_{n_j}. \tag{6.18}$$

Substituting Eqs. (6.17)–(6.18) into Eqs. (6.11)–(6.12) and (6.9), and applying the Galerkin's testing procedure, we can convert the integral equations to a linear equation system written as

$$\begin{bmatrix} \overline{\boldsymbol{Z}}^{E_2 I_2} & \overline{\boldsymbol{C}}^{E_2 M_2} & \theta\overline{\boldsymbol{Z}}^{E_2 I_0} \\ \overline{\boldsymbol{D}}^{H_2 I_2} & \overline{\boldsymbol{Y}}^{H_2 M_2} & \theta\overline{\boldsymbol{D}}^{H_2 I_0} \\ \theta\overline{\boldsymbol{Z}}^{E_0 I_2} & \theta\overline{\boldsymbol{C}}^{E_0 M_2} & \overline{\boldsymbol{Z}}^{E_0 I_0} \end{bmatrix} \begin{bmatrix} \boldsymbol{I}_2 \\ \boldsymbol{M}_2 \\ \boldsymbol{I}_0 \end{bmatrix} = \begin{bmatrix} \boldsymbol{E}_2 \\ \boldsymbol{H}_2 \\ \delta\boldsymbol{E}_0 \end{bmatrix} \tag{6.19}$$

where the $\boldsymbol{I}_0$ stands for coefficients of the equivalent electric current density on S_{0i} and the ($\boldsymbol{I}_2$, $\boldsymbol{M}_2$) are the coefficients of the equivalent electric and magnetic current densities on S_{21}. The elements of the sub-matrices, for $u \neq v$, are defined as

$$Z_{mn}^{E_u I_v} = -\int_{T_{m_u}} \boldsymbol{f}_{m_u}(\mathbf{r}) \cdot \left(j\omega\mu_a \boldsymbol{P}_{n_v}^a + \frac{j}{\omega\epsilon_a} \boldsymbol{Q}_{n_v}^a \right) dS_{m_u} \tag{6.20a}$$

$$Y_{mn}^{H_u M_v} = -\int_{T_{m_u}} \boldsymbol{f}_{m_u}(\mathbf{r}) \cdot \left(j\omega\epsilon_a \boldsymbol{P}_{n_v}^a + \frac{j}{\omega\mu_a} \boldsymbol{Q}_{n_v}^a \right) dS_{m_u} \tag{6.20b}$$

$$C_{mn}^{E_u M_v} = -\int_{T_{m_u}} \boldsymbol{f}_{m_u}(\mathbf{r}) \cdot \left(\boldsymbol{\nabla} \times \boldsymbol{P}_{n_v}^a \right) dS_{m_u} \tag{6.20c}$$

$$D_{mn}^{H_u I_v} = -C_{mn}^{E_u M_v} \tag{6.20d}$$

and

$$Z_{mn}^{E_0 I_0} = \int\limits_{T_{m_0}} \boldsymbol{f}_{m_0}(\mathbf{r}) \cdot \left(j\omega\mu_a \boldsymbol{P}_{n_0}^a + \frac{j}{\omega\epsilon_a} \boldsymbol{Q}_{n_0}^a \right) dS_{m_0} \tag{6.21a}$$

$$Z_{mn}^{E_2 I_2} = \int\limits_{T_{m_2}} \boldsymbol{f}_{m_2}(\mathbf{r}) \cdot \left(j\omega\mu_1 \boldsymbol{P}_{n_2}^1 + \frac{j}{\omega\epsilon_1} \boldsymbol{Q}_{n_2}^1 + j\omega\mu_2 \boldsymbol{P}_{n_2}^2 + \frac{j}{\omega\epsilon_2} \boldsymbol{Q}_{n_2}^2 \right) dS_{m_2} \tag{6.21b}$$

$$Y_{mn}^{H_2 M_2} = \int\limits_{T_{m_2}} \boldsymbol{f}_{m_2}(\mathbf{r}) \cdot \left(j\omega\epsilon_1 \boldsymbol{P}_{n_2}^1 + \frac{j}{\omega\mu_1} \boldsymbol{Q}_{n_2}^1 + j\omega\epsilon_2 \boldsymbol{P}_{n_2}^2 + \frac{j}{\omega\mu_2} \boldsymbol{Q}_{n_2}^2 \right) dS_{m_2} \tag{6.21c}$$

$$C_{mn}^{E_2 M_2} = \int\limits_{T_{m_2}} \boldsymbol{f}_{m_2}(\mathbf{r}) \cdot \left(\boldsymbol{\nabla} \times \boldsymbol{P}_{n_2}^1 + \boldsymbol{\nabla} \times \boldsymbol{P}_{n_2}^2 \right) dS_{m_2} \tag{6.21d}$$

$$D_{mn}^{H_2 I_2} = -\, C_{mn}^{E_2 M_2} \tag{6.21e}$$

where

$$\boldsymbol{P}_{n_v}^u = \int\limits_{T_{n_v}} \boldsymbol{f}_{n_v}(\mathbf{r}') g_u(\mathbf{r}, \mathbf{r}')\, dS_{n_v} \tag{6.22}$$

$$\boldsymbol{Q}_{n_v}^u = \boldsymbol{\nabla} \int\limits_{T_{n_v}} \boldsymbol{\nabla}_s' \cdot \boldsymbol{f}_{n_v}(\mathbf{r}') g_u(\mathbf{r}, \mathbf{r}')\, dS_{n_v} \tag{6.23}$$

while the symbols μ_u and ϵ_u denote the permeability and permittivity in medium u, respectively. The elements of the excitation electric and magnetic fields are expressed as

$$E_{u,m} = \int\limits_{T_{m_u}} \boldsymbol{f}_{m_u} \cdot \boldsymbol{E}^{inc}\, dS_{m_u} \tag{6.24a}$$

$$H_{u,m} = \int\limits_{T_{m_u}} \boldsymbol{f}_{m_u} \cdot \boldsymbol{H}^{inc}\, dS_{m_u}. \tag{6.24b}$$

For our problem, we let ($\delta = 0$, $\theta = 1$, $a = 2$) and ($\delta = 1$, $\theta = -1$, $a = 1$) for cases shown in Fig. 6.1(a) and Fig. 6.1(b), respectively.

6.2.3 AIM Implementation

The AIM algorithm described in Chapter 2 needs some modifications in order to account for the equivalent current densities radiating in different media. We assume that there are altogether a total of R media containing current densities. The scatterer is first placed in a rectangular region in every medium, which will be recursively subdivided into smaller cells. A total number of W_r cells will be produced if the subdivision of the rectangular region is taken place in medium r. Each of the basis functions f_n will only be bounded by a cell which comprises $(M+1)^3 = 27$ grid points. Let $N_{t,r}$ denote the total number of basis functions in medium r and $N_{c,r}(w)$ denote the number of basis functions enclosed by the w_r-th cell.

In the initialization stage, the projection matrices of the current densities in all media, $\overline{\mathbf{\Lambda}}_r$, are computed and stored. The Green's function matrices for all media, $\overline{\boldsymbol{G}}_r$, are also computed and stored. During the matrix-vector multiplication, the current densities contained within the same medium will be projected to the grid points of the respective medium. The projection procedure is repeated for the current densities radiating in other media. Next, the Fourier transform of the far-zone interactions for all media are computed and subsequently transferred to the respective testing functions. Lastly, the corrected near-zone interactions of different media are added to the output. The complete modified AIM algorithm is shown in Algorithm 4.

/*Initialization */
for each medium $r = 1$ *to* R **do**
  Compute $\widetilde{\boldsymbol{G}}_r = \mathrm{FFT}(\overline{\boldsymbol{G}}_r)$
  Compute $\overline{\boldsymbol{\Delta}}_r = \overline{\boldsymbol{Z}} - \overline{\boldsymbol{\Lambda}}_r \, \overline{\boldsymbol{G}}_r \, \overline{\boldsymbol{\Lambda}}_r^T$
end
/* Projection step */
for each medium $r = 1$ *to* R **do**
  Set $\widehat{\boldsymbol{I}}_r = 0$
  for each cell $p = 1$ *to* W_r **do**
    for each basis function q in cell p, $q = 1$ *to* $N_{c,r}(p)$ **do**
      $\widehat{I}_r(p) = \widehat{I}_r(p) + [\Lambda_r(p,q)]^T I_{q,r}(p)$
    end
  end
end
/* Far-zone interaction */
for each medium $r = 1$ *to* R **do**
  Compute $\widetilde{\boldsymbol{I}}_r = \mathrm{FFT}(\widehat{\boldsymbol{I}}_r)$
  Compute $\widetilde{\boldsymbol{P}}_r = \widetilde{\boldsymbol{G}}_r \cdot \widetilde{\boldsymbol{I}}_r$
  Compute $\widehat{\boldsymbol{P}}_r = \mathrm{FFT}^{-1}(\widetilde{\boldsymbol{P}}_r)$
end
for each medium $r = 1$ *to* R **do**
  Set $\boldsymbol{V}_r = 0$
  for each cell $p = 1$ *to* W_r **do**
    for each basis function q in cell p, $q = 1$ *to* $N_{c,r}(p)$ **do**
      $V_{q,r}(p) = V_{q,r}(p) + \Lambda_r(p,q)\widehat{P}_r(p)$
    end
  end
end
/* Near-zone interaction */
for each medium $r = 1$ *to* R **do**
  for each basis function $p = 1$ *to* $N_{t,r}$ **do**
    for each basis function q with, $q = 1$ *to* $N_{nz,r}(p)$ **do**
      $V_{q,r}(p) = V_{q,r}(p) + \Delta_r(p,q) I_{q,r}(p)$
    end
  end
end

Algorithm 4: AIM algorithm for solving electromagnetic scattering problems of composite dielectric and conducting objects characterized using the SIE.

Fig. 6.2(a) shows an example of sparsity pattern of the near-zone matrix $\overline{\boldsymbol{Z}}^{\mathrm{near}}$ generated by the modified AIM. By inspecting the matrix carefully, we find that the sub-matrices $Y_{mn}^{H_2M_2}$ and $D_{mn}^{H_2I_2}$ need not be stored as they can be computed using the sub-matrices $Z_{mn}^{E_2I_2}$ and $C_{mn}^{E_2M_2}$, respectively. Hence some savings in memory

can be achieved. Fig. 6.2(b) depicts the sparsity pattern of $\overline{\boldsymbol{Z}}^{\text{near}}$ generated by a more efficient implementation.

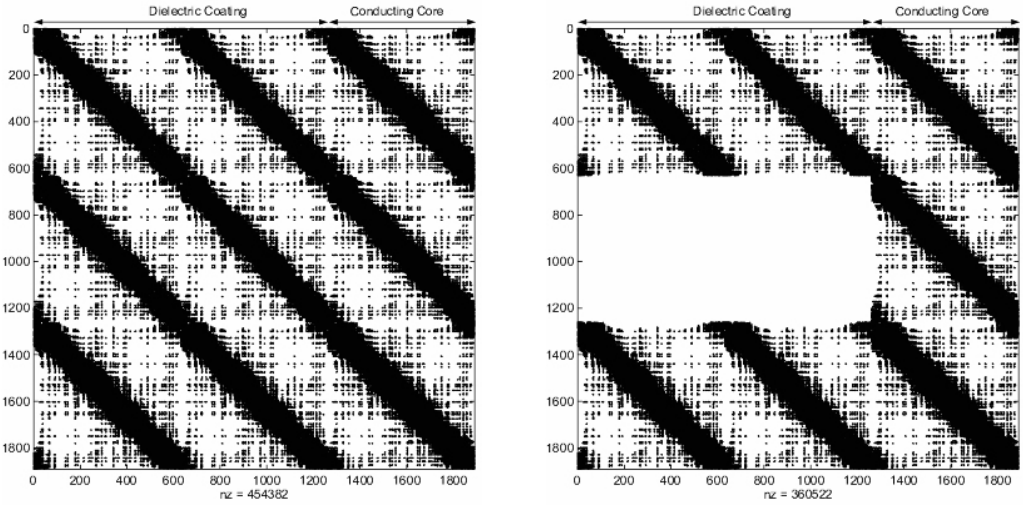

(a) Direct implementation (b) Efficient implementation

Figure 6.2: Sparsity patterns of $\overline{\boldsymbol{Z}}^{\text{near}}$ for composite conducting and dielectric object (SIE).

6.2.4 Numerical Results

In this section, three examples are presented to demonstrate the applicability of AIM in solving the scattering problems of composite conducting and dielectric objects characterized using the SIE method. The first example we consider is a coated metallic sphere having a radius of 1 m. The conducting core has a radius of 0.9 m and the thickness of the coating layer is 0.1 m with a relative permittivity of $\epsilon_r = 1.6 - j0.8$. The bistatic RCSs for VV− and HH−polarizations are computed at 600 MHz using 45,540 unknowns and the results are shown in Fig. 6.3. The results are compared with the Mie series solutions and a good agreement is observed. The first example is also to serve as validation of accuracy of our AIM code.

The second example considered is a metallic-dielectric cylinder. The diameter of the cylinder is 7.62 cm while the length of the metallic and dielectric cylinders is 5.08 cm each. The relative permittivity of the dielectric cylinder is $\epsilon_r = 2.6$. The

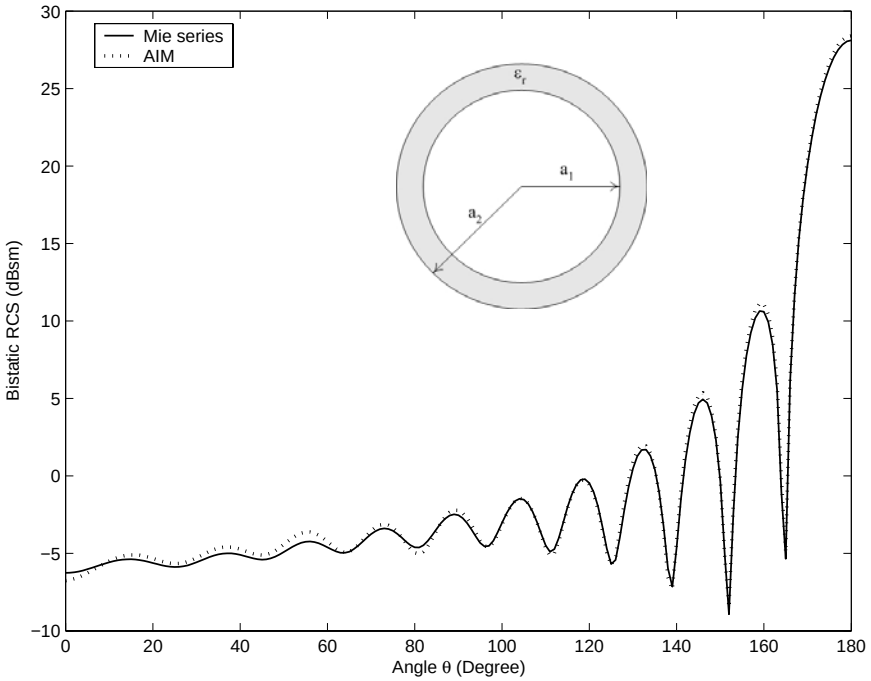

(a) VV−polarization

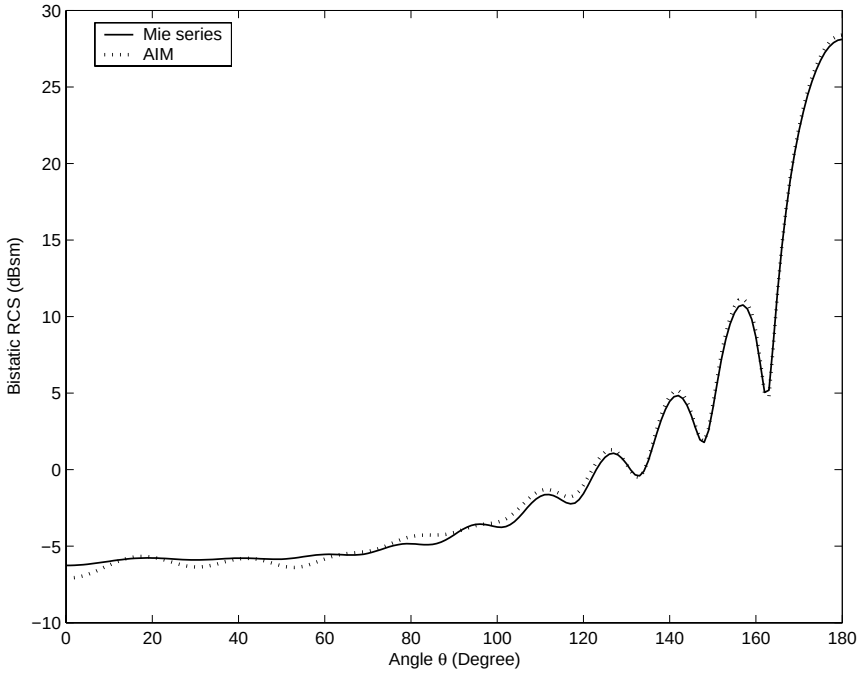

(b) HH−polarization

Figure 6.3: Bistatic RCSs of a coated dielectric sphere ($a_1 = 0.9$ m; $a_2 = 1$ m, $\epsilon_r = 1.6 - j0.8$) at 600 MHz. (a) VV−polarization. (b) HH−polarization.

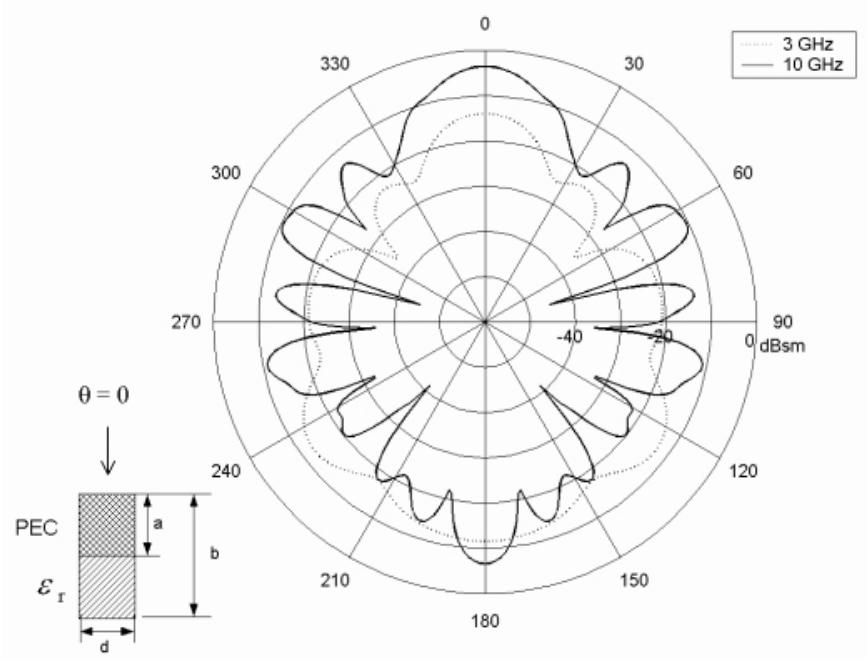

(a) VV−polarization

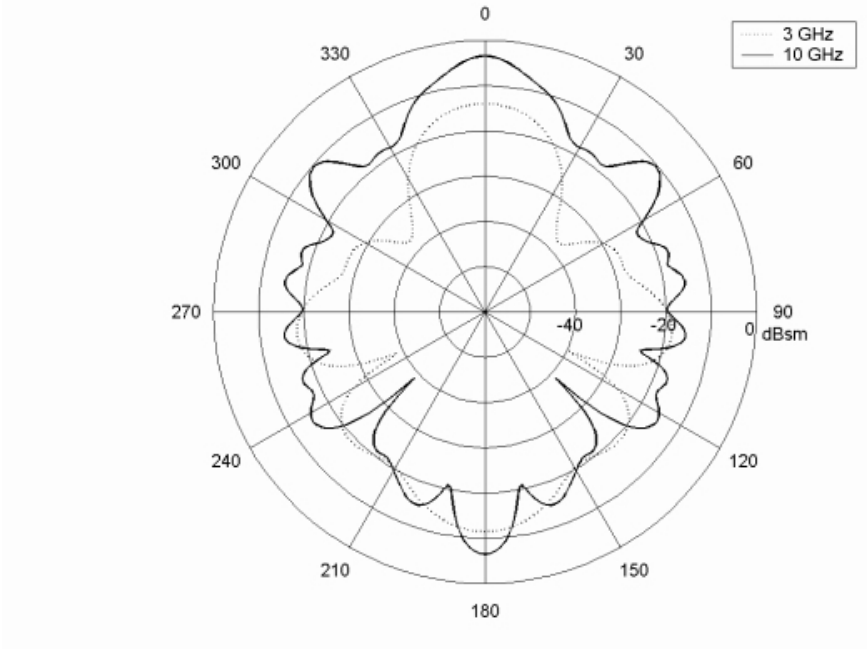

(b) HH−polarization

Figure 6.4: Monostatic RCSs of a PEC-dielectric cylinder (a = 5.08 cm, b = 10.16 cm, d = 7.62 cm, and ϵ_r = 2.6). (a) VV−polarization. (b) HH−polarization.

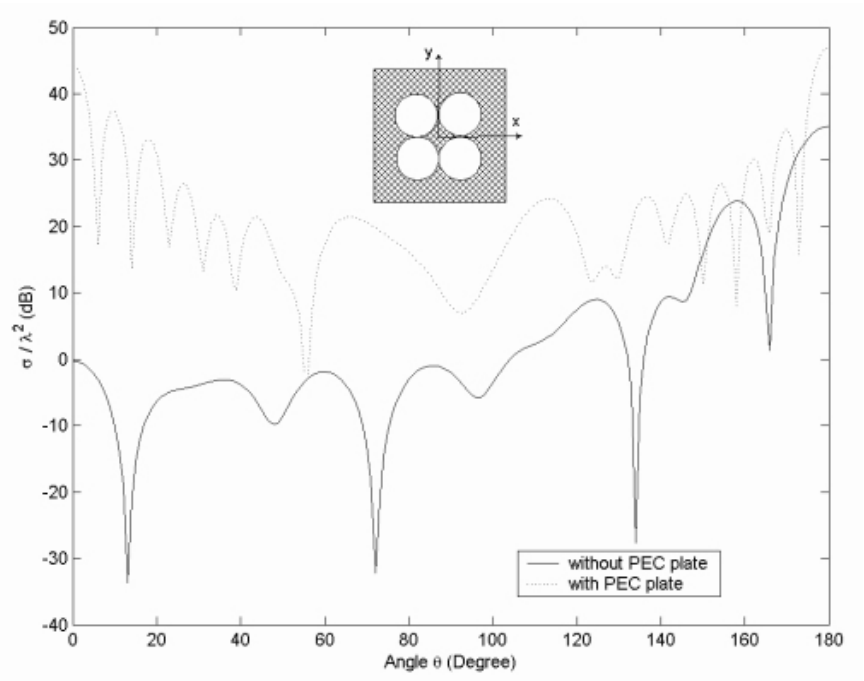

(a) VV−polarization

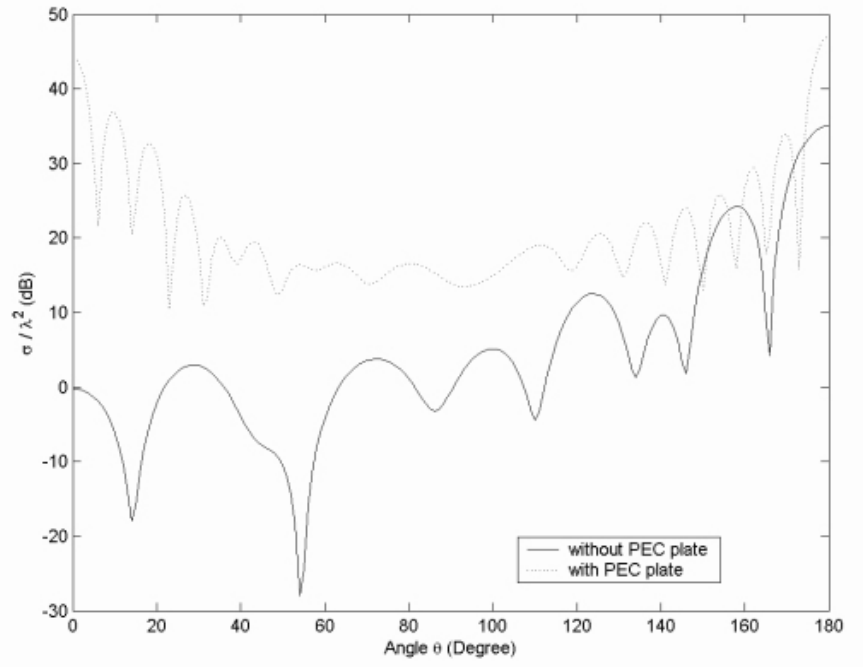

(b) HH−polarization

Figure 6.5: Bistatic RCSs of four agglomerated dielectric spheres ($r = 1\lambda$, $\epsilon_r = 1.6 - j0.4$) in the presence and absence of an $8\lambda \times 8\lambda$ PEC plate. (a) VV−polarization. (b) HH−polarization.

monostatic RCSs for VV− and HH−polarizations are computed at 3 GHz and 10 GHz, and are shown in Fig. 6.4. The RCSs computed at 3 GHz agree well with the published results [31].

The last example considered is a system consisting of four agglomerated dielectric spheres on the top of a PEC plate. The diameter of each of the four spheres is 2λ and the relative permittivity of each of the spheres is $1.6 - j0.4$. The $8\lambda \times 8\lambda$ PEC plate is placed at $z = 0$ and the centers of the spheres are located 1.3λ above the PEC plate. The scattering of plane wave by the spheres in the presence and absence of the finite PEC plate are computed and shown in Fig. 6.5. As expected, the RCSs is higher for the case in the presence of the PEC plate.

Table 6.1 shows the memory used by the AIM and the estimated memory for the MoM in computing the examples. From Table 6.1, we find that the saving in memory is more than 98%. Table 6.2 compares the CPU time taken by the AIM and the estimated CPU time for the MoM in computing the examples.

Table 6.1: Comparison of memory requirement between the AIM and the MoM in solving electromagnetic scattering problems of composite conducting and dielectric objects characterized using the SIE.

Example	Unknowns, N	AIM, M_{AIM}(MB)	MoM, M_{MoM}(GB)	M_{AIM}/M_{MoM}
Coated metallic sphere	45,540	269.51	15.45	1.70%
Metallic-dielectric cylinder (10 GHz)	37,008	173.53	10.20	1.67%
Spheres with PEC plate	43,937	108.71	14.38	0.74%

Note: 1 KB = 1,024 Bytes, 1 MB = 1,024 KB and 1 GB = 1,024 MB

Table 6.2: Comparison of CPU time between the AIM and the MoM in solving electromagnetic scattering problems of composite conducting and dielectric objects characterized using the SIE.

Example	Unknowns, N	AIM, T_{AIM}(sec)	MoM, T_{MoM}(sec)
Coated metallic sphere	45,540	2,020	3,816
Metallic-dielectric cylinder (10 GHz)	37,008	4,533	6,999
Spheres with PEC plate	43,937	4,024	6,099

6.3 Hybrid Volume-Surface Integral Equation Method

6.3.1 Formulation

Consider an arbitrarily shaped 3-D scatterer, which consists of inhomogeneous dielectric material and conducting body as shown in Fig. 6.6. The object is embedded in an isotropic homogeneous background medium with permittivity ϵ_b and permeability μ_b. The scatterer is illuminated by an incident wave $\boldsymbol{E}^{inc}$, which is excited by impressed sources in the background media. The dielectric region V is assumed to have the permeability $\mu = \mu_b$ and complex dielectric constant $\tilde{\epsilon} = \epsilon(\boldsymbol{r}) - j\sigma(\boldsymbol{r})/\omega$ where $\epsilon(\boldsymbol{r})$ and $\sigma(\boldsymbol{r})$ are permittivity and conductivity, respectively, at $\boldsymbol{r}$.

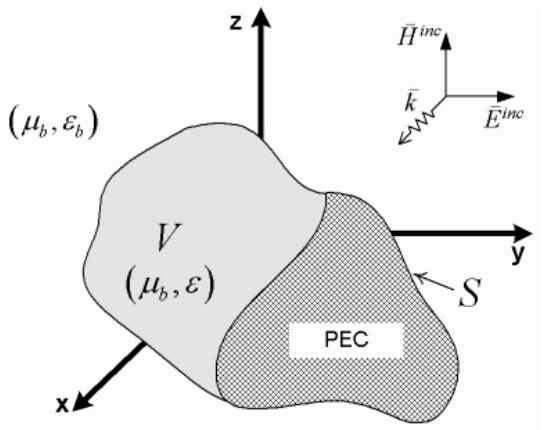

Figure 6.6: Geometry of a scatterer consisting of dielectric material and conducting body embedded in an isotropic homogeneous medium.

By using volume equivalence principle in the dielectric region V, the equivalent volume current densities

$$\boldsymbol{J}_V = j\omega\left(\tilde{\epsilon}-\epsilon_1\right)\boldsymbol{E} \tag{6.25a}$$

$$\boldsymbol{K}_V = j\omega\left(\mu-\mu_1\right)\boldsymbol{H} = 0. \tag{6.25b}$$

In other hand, by using surface equivalence principle on the surface of conductor S, the equivalent surface current densities

$$\boldsymbol{J}_S = \widehat{\boldsymbol{n}}\times\boldsymbol{H} \tag{6.26a}$$

$$\boldsymbol{K}_S = \boldsymbol{E}\times\widehat{\boldsymbol{n}} = 0. \tag{6.26b}$$

The scattered electric field $\boldsymbol{E}^{sca}$ and magnetic field $\boldsymbol{H}^{sca}$ produced by the induced volume and surface current densities are given by

$$\boldsymbol{E}_\Omega^{sca}(\boldsymbol{r}) = -\eta_b\mathcal{L}_b\boldsymbol{J}_\Omega,\ \Omega = S \text{ or } V \tag{6.27}$$

$$\boldsymbol{H}_\Omega^{sca}(\boldsymbol{r}) = \mathcal{M}_b\boldsymbol{J}_\Omega,\ \Omega = S \text{ or } V. \tag{6.28}$$

In the dielectric region V, by taking the scattered field from the surface current into consideration, the total electric field becomes

$$\boldsymbol{E}\left(\boldsymbol{r}\right) = \boldsymbol{E}^{inc}\left(\boldsymbol{r}\right) + \boldsymbol{E}_V^{sca}\left(\boldsymbol{r}\right) + \boldsymbol{E}_S^{sca}\left(\boldsymbol{r}\right). \tag{6.29}$$

Similarly, the scattered field by volume current density also contributes to the total field on S. Since the tangential components of total electric field vanish on conducting surface, we get

$$\widehat{\boldsymbol{n}}\times\boldsymbol{E}^{inc}\left(\boldsymbol{r}\right) = -\widehat{\boldsymbol{n}}\times\left[\boldsymbol{E}_V^{sca}\left(\boldsymbol{r}\right) + \boldsymbol{E}_S^{sca}\left(\boldsymbol{r}\right)\right]. \tag{6.30}$$

Eqs. (6.29) and (6.30) are known as the EFIE as the formulations involve only electric field. For a closed conducting surface, the MFIE can be obtained by con-

sidering the tangential components of the total magnetic field on the conducting surface, which are equal to the induced surface current components. Thus, we get

$$\widehat{\boldsymbol{n}} \times \boldsymbol{H}^{inc}(\boldsymbol{r}) = \boldsymbol{J}_S - \widehat{\boldsymbol{n}} \times \left[\boldsymbol{H}_V^{sca}(\boldsymbol{r}) + \boldsymbol{H}_S^{sca}(\boldsymbol{r})\right]. \tag{6.31}$$

In addition, the CFIE can be formulated for a closed conducting body by linearly combining the EFIE and the MFIE such that

$$\text{CFIE} = \alpha\text{EFIE} + (1-\alpha)\,\text{MFIE} \tag{6.32}$$

where α is a real value between 0 and 1. Since EFIE and MFIE are just special cases of CFIE, we can generally use the CFIE as the SIE in the VSIE formulation.

6.3.2 Method of Moments

The volume of dielectric material and the surface of conducting body are discretized into tetrahedral elements and triangular patches, respectively. These elements are used because of their flexibility to model arbitrarily shaped 3-D object. The surface current density is expanded using the the RWG basis functions $\boldsymbol{f}_n^S$

$$\boldsymbol{J}_S = \sum_{n=1}^{N_S} I_n^S \boldsymbol{f}_n^S. \tag{6.33}$$

As for the dielectric region, the electric flux density $\boldsymbol{D}$ is expanded using the SWG basis functions $\boldsymbol{f}_n^V$ as follows

$$\boldsymbol{D} = \tilde{\epsilon}(\boldsymbol{r})\,\boldsymbol{E} = \sum_{n=1}^{N_V} I_n^V \boldsymbol{f}_n^V. \tag{6.34}$$

By use of Eq. (6.25a), the volume current density is expressed below:

$$\boldsymbol{J}_V = j\omega \sum_{n=1}^{N_V} I_n^V \frac{\tilde{\epsilon}(\boldsymbol{r}) - \epsilon_b}{\tilde{\epsilon}(\boldsymbol{r})} \boldsymbol{f}_n^V = j\omega \sum_{n=1}^{N_V} I_n^V \kappa(\boldsymbol{r})\, \boldsymbol{f}_n^V \tag{6.35}$$

where $\kappa(\bar{r}) = (\tilde{\epsilon}(\bar{r}) - \epsilon_b)/\tilde{\epsilon}(\bar{r})$ is the contrast ratio [29]. The properties of the SWG and the RWG basis functions, for example, the continuity of the electric flux density normal to the interior face (SWG) and the continuity of the surface current density normal to the interior edge (RWG), make them suitable to be implemented in efficiently solving integral equations. It is also noted during discretization of the body, the triangular patches are generated such that it is coincided with the surface of tetrahedron.

Using the volume basis functions to test Eq. (6.29) and the surface basis functions to test Eq. (6.32), the hybrid integral equations will be converted into a matrix equation system as

$$\begin{bmatrix} \overline{\boldsymbol{Z}}^{VV} & \overline{\boldsymbol{Z}}^{VS} \\ \overline{\boldsymbol{Z}}^{SV} & \overline{\boldsymbol{Z}}^{SS} \end{bmatrix} \begin{bmatrix} \boldsymbol{I}^V \\ \boldsymbol{I}^S \end{bmatrix} = \begin{bmatrix} \boldsymbol{E}^V \\ \boldsymbol{E}^S \end{bmatrix} \tag{6.36}$$

where the vectors $\boldsymbol{I}^V$ and $\boldsymbol{I}^S$ represent the coefficients of volume and surface current densities, respectively. The excitation vector can be computed using

$$E_m^V = \int_{V_m} \boldsymbol{f}_m^V \cdot \boldsymbol{E}^{inc}(\boldsymbol{r}')\, dV' \tag{6.37a}$$

$$E_m^S = \int_{S_m} \boldsymbol{f}_m^S \cdot \left[\alpha \boldsymbol{E}^{inc}(\boldsymbol{r}') + (1-\alpha)\,\eta_b \boldsymbol{H}^{inc}(\boldsymbol{r}')\right] dS' \tag{6.37b}$$

while the elements of the block matrices can be computed using

$$\begin{aligned} Z_{mn}^{VV} &= \int_{V_m} \frac{\boldsymbol{f}_m^V \cdot \boldsymbol{f}_n^V}{\epsilon} dV - \omega k_b \eta_b \int_{V_m} \boldsymbol{f}_m^V \cdot \Big[\int_{V_n} \kappa \boldsymbol{f}_n^V g(\boldsymbol{r},\boldsymbol{r}') dV' + \\ &\quad \frac{\boldsymbol{\nabla}}{k_b^2} \int_{V_n} \boldsymbol{\nabla}' \cdot \left(\kappa \boldsymbol{f}_n^V\right) g(\boldsymbol{r},\boldsymbol{r}') dV' \Big] dV \end{aligned} \tag{6.38a}$$

$$\begin{aligned} Z_{mn}^{VS} &= jk_b\eta_b \int_{V_m} \boldsymbol{f}_m^V \cdot \Big[\int_{S_n} \boldsymbol{f}_n^S g(\boldsymbol{r},\boldsymbol{r}') dS' + \\ &\quad \frac{\boldsymbol{\nabla}}{k_b^2} \int_{S_n} \boldsymbol{\nabla}' \cdot \boldsymbol{f}_n^S g(\boldsymbol{r},\boldsymbol{r}') dS' \Big] dV \end{aligned} \tag{6.38b}$$

$$\begin{aligned} Z_{mn}^{SV} &= \int_{S_m} \boldsymbol{f}_m^S \cdot\, j\omega \Big[\alpha j k_b \eta_b \left(\int_{V_n} \kappa \boldsymbol{f}_n^V g(\boldsymbol{r},\boldsymbol{r}') dV' + \right. \\ &\quad \left. \frac{\boldsymbol{\nabla}}{k_b^2} \int_{V_n} \boldsymbol{\nabla}' \cdot \left(\kappa \boldsymbol{f}_n^V\right) g(\boldsymbol{r},\boldsymbol{r}') dV' \right) - (1-\alpha)\,\eta_b \end{aligned}$$

$$\boldsymbol{\nabla} \times \int_{V_n} \kappa \boldsymbol{f}_n^V g(\boldsymbol{r}, \boldsymbol{r}') dV' \Big] \, dS \tag{6.38c}$$

$$Z_{mn}^{SS} = \int_{S_m} \boldsymbol{f}_m^S \cdot \Big[\alpha j k_b \eta_b \Big(\int_{S_n} \boldsymbol{f}_n^S g(\boldsymbol{r}, \boldsymbol{r}') dS' + \frac{\boldsymbol{\nabla}}{k_b^2} \int_{S_n} \boldsymbol{\nabla}' \cdot \boldsymbol{f}_n^S g(\boldsymbol{r}, \boldsymbol{r}') dS' \Big) + (1 - \alpha) \eta_b \Big(\frac{1}{2} \boldsymbol{f}_n^S - \boldsymbol{\nabla} \times \fint_{S_n} \boldsymbol{f}_n^S g(\boldsymbol{r}, \boldsymbol{r}') dS' \Big) \Big] \, dS \tag{6.38d}$$

where $\fint_S$ is the Cauchy principal value. The κ is a constant value within the tetrahedron and it can be taken out from the integration. Besides, we can also rewrite

$$\boldsymbol{\nabla} \cdot \left(\kappa \boldsymbol{f}_n^V \right) = \kappa \boldsymbol{\nabla} \cdot \boldsymbol{f}_n^V + \boldsymbol{\nabla} \kappa \cdot \boldsymbol{f}_n^V \tag{6.39}$$

where the second term is 0 and $I_n^V \left(\kappa_n^+ - \kappa_n^- \right)$ for similar and dissimilar media in $\boldsymbol{f}_n^V$, respectively [29].

6.3.3 AIM Implementation

In the hybrid VSIE formulation, the equivalent volume and surface current densities are the unknowns to be determined. Hence the AIM algorithm needs to be modified to account for both current densities. The scatterer is contained in a rectangular region which has been subdivided into W cells. Each of the basis functions ($\boldsymbol{f}_n^V$ and $\boldsymbol{f}_n^S$) is bounded by a cell which comprises $(M+1)^3 = 27$ grid points. Let N_t^V and N_t^S denote the total number of volume and surface basis functions, and $N_c^V(w)$ and $N_c^S(w)$ denote the numbers of volume and surface basis functions in a w-th cell.

In the initialization stage, the projection matrices for the equivalent volume and surface current densities, $\overline{\boldsymbol{\Lambda}}^{\Omega}$, are computed separately and stored. It is noted that the projection schemes for both current densities are identical except that the equivalent volume current density need to be projected together with the contrast ratio, κ. Since both equivalent current densities radiate in background medium, only one Green's function matrix is required. During the matrix-vector multiplica-

tion, the current densities will be first projected onto grid points. Then the far-zone interactions are computed by convolving the grid currents with the Green's function matrix and subsequently transferred back to the respective testing functions. Lastly, the corrected near-zone interactions of different regions are added to the output. The complete modified AIM algorithm is given in Algorithm 5.

/*Initialization */
Compute $\widetilde{\overline{\boldsymbol{G}}} = \mathrm{FFT}(\overline{\boldsymbol{G}})$
Compute $\overline{\boldsymbol{\Delta}} = \overline{\boldsymbol{Z}} - \overline{\boldsymbol{\Lambda}}\,\overline{\boldsymbol{G}}\,\overline{\boldsymbol{\Lambda}}^T$
/* Projection step */
Set $\widehat{\boldsymbol{I}} = 0$
for each cell $p = 1$ *to* W **do**
  for $\Omega = V$ and S **do**
    for each basis function f_q^Ω in cell p, $q = 1$ *to* $N_c^\Omega(p)$ **do**
      $\widehat{I}(p) = \widehat{I}(p) + [\Lambda^\Omega(p,q)]^T I_q^\Omega(p)$
    end
  end
end
/* Far-zone interaction */
Compute $\widetilde{\boldsymbol{I}} = \mathrm{FFT}(\widehat{\boldsymbol{I}})$
Compute $\widetilde{\boldsymbol{P}} = \widetilde{\boldsymbol{G}} \cdot \widetilde{\boldsymbol{I}}$
Compute $\widehat{\boldsymbol{P}} = \mathrm{FFT}^{-1}(\widetilde{\boldsymbol{P}})$
Set $\boldsymbol{\mathcal{V}} = 0$
for each cell $p = 1$ *to* W **do**
  for $\Omega = V$ and S **do**
    for each basis function f_q^Ω in cell p, $q = 1$ *to* $N_c^\Omega(p)$ **do**
      $\mathcal{V}_q^\Omega(p) = \mathcal{V}_q^\Omega(p) + \Lambda^\Omega(p,q)\widehat{P}(p)$
    end
  end
end
/* Near-zone interaction */
for $\Omega = V$ and S **do**
  for each basis function $f_p^\Omega = 1$ *to* N_t^Ω **do**
    for each basis function f_q^V with, $q = 1$ *to* $N_{nz}^V(p)$ **do**
      $\mathcal{V}_q^\Omega(p) = \mathcal{V}_q^\Omega(p) + \Delta^{\Omega V}(p,q) I_q^V(p)$
    end
    for each basis function f_q^S with, $q = 1$ *to* $N_{nz}^S(p)$ **do**
      $\mathcal{V}_q^\Omega(p) = \mathcal{V}_q^\Omega(p) + \Delta^{\Omega S}(p,q) I_q^S(p)$
    end
  end
end

Algorithm 5: AIM algorithm for solving electromagnetic scattering problems of composite dielectric and conducting objects characterized using the hybrid VSIE.

A typical near-zone matrix $\overline{\boldsymbol{Z}}^{\mathrm{near}}$ generated by using our modified AIM is shown in Fig. 6.7. A coated conducting sphere has been used to generate the $\overline{\boldsymbol{Z}}^{\mathrm{near}}$ in this example. We have also shown the reordered $\overline{\boldsymbol{Z}}^{\mathrm{near}}$ to clearly show the saving achieved by the AIM.

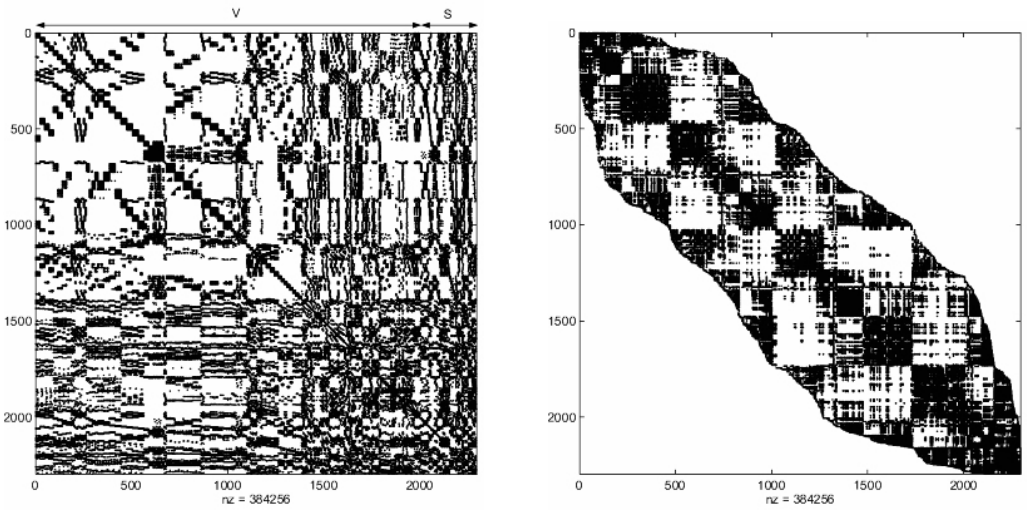

(a) Actual sparsity pattern (b) Reordered sparsity pattern

Figure 6.7: Sparsity patterns of $\overline{\boldsymbol{Z}}^{\text{near}}$ for the composite conducting and dielectric object (VSIE).

6.3.4 Numerical Results

In this section, several examples will be presented to show the accuracy of the proposed method. The first example we consider is a coated conducting sphere having a radius of 1 m. The core of the sphere has a radius of 0.8 m and the thickness of the coating layer, with a relative permittivity of $\epsilon_r = 1.6 - j0.8$, is 0.2 m. The bistatic RCSs for the VV− and HH−polarizations at 300 MHz are computed with 31,174 unknowns and the results are shown in Fig. 6.8. The RCS results are compared with the Mie series solutions and a good agreement has been observed in each case.

The second example is a dielectric-conducting cylinder. The diameter of the cylinder is 7.62 cm while the length of the metallic and dielectric cylinders is 5.08 cm each. The monostatic RCSs for the VV− and HH−polarizations in the XZ−plane are computed at 3 GHz with 11,864 unknowns. The results are shown in Fig. 6.9 and a good agreement is observed with the results obtained using SIE.

The third example is a coated conducting cylinder. The diameter and height of the cylinder are 2 λ and 6 λ, respectively. The cylinder has one coating layer

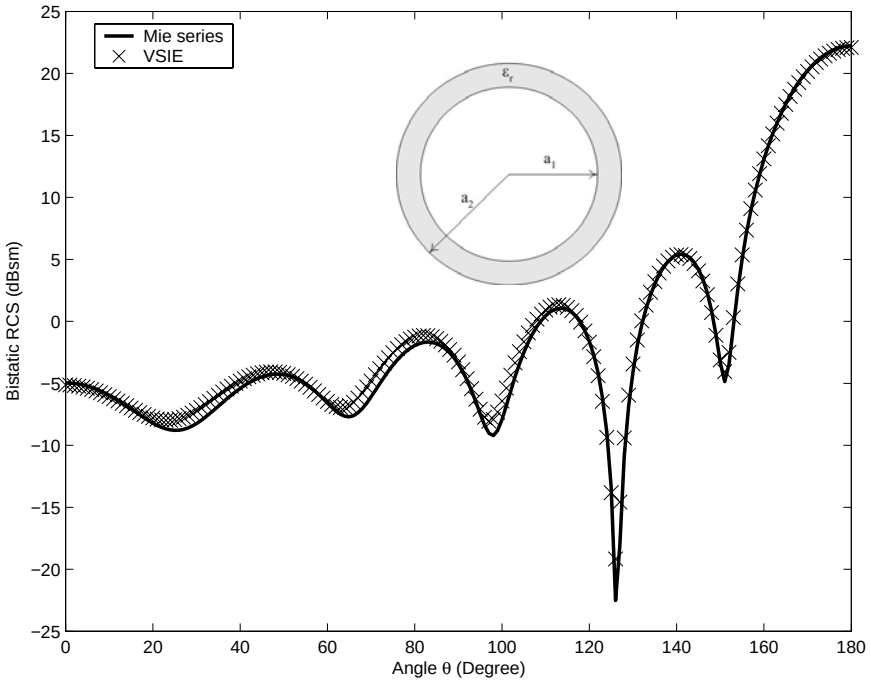

(a) VV−polarization

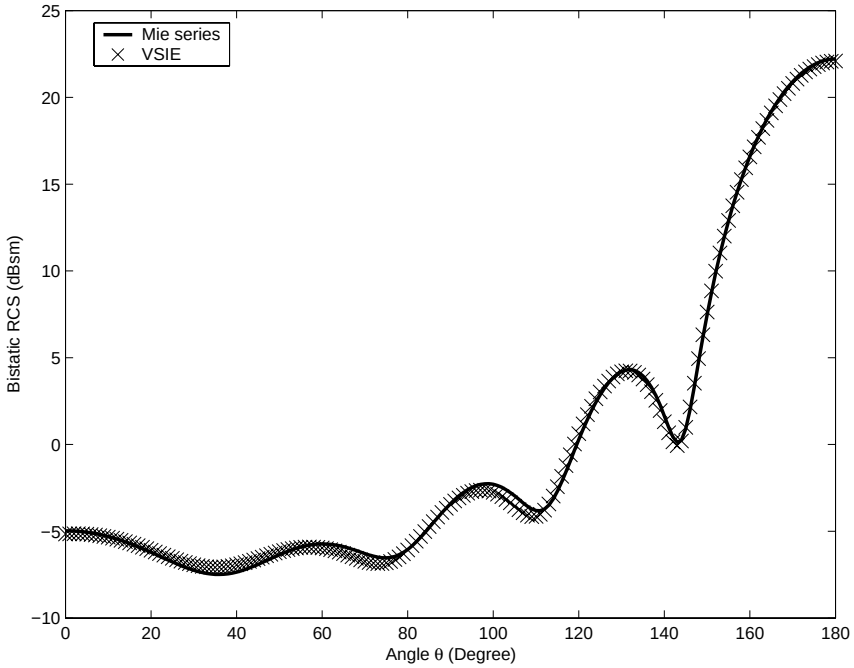

(b) HH−polarization

Figure 6.8: Bistatic RCSs of a coated conducting sphere ($a_1 = 0.8$ m, $a_2 = 1$ m, and $\epsilon_r = 1.6 - j0.8$) at 300 MHz. (a) VV−polarization. (b) HH−polarization.

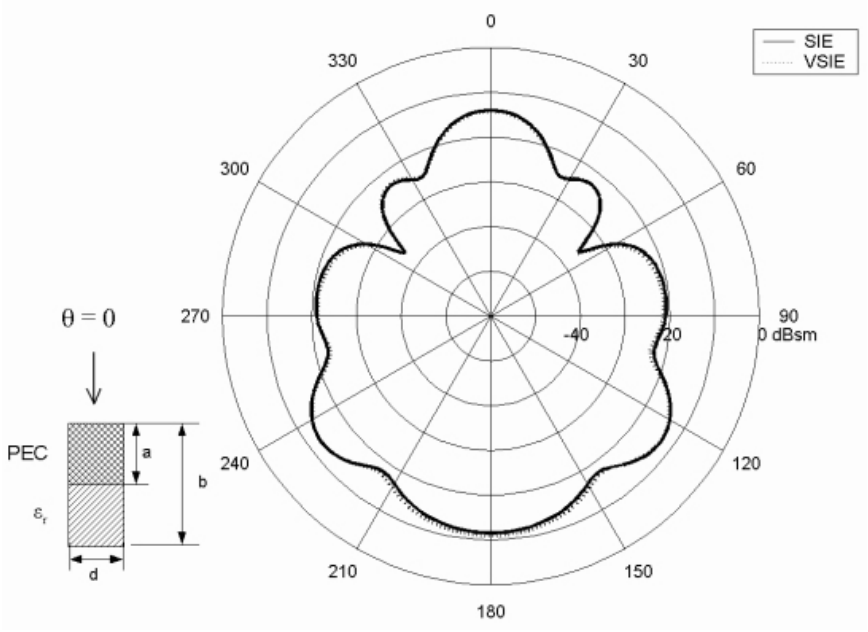

(a) VV−polarization

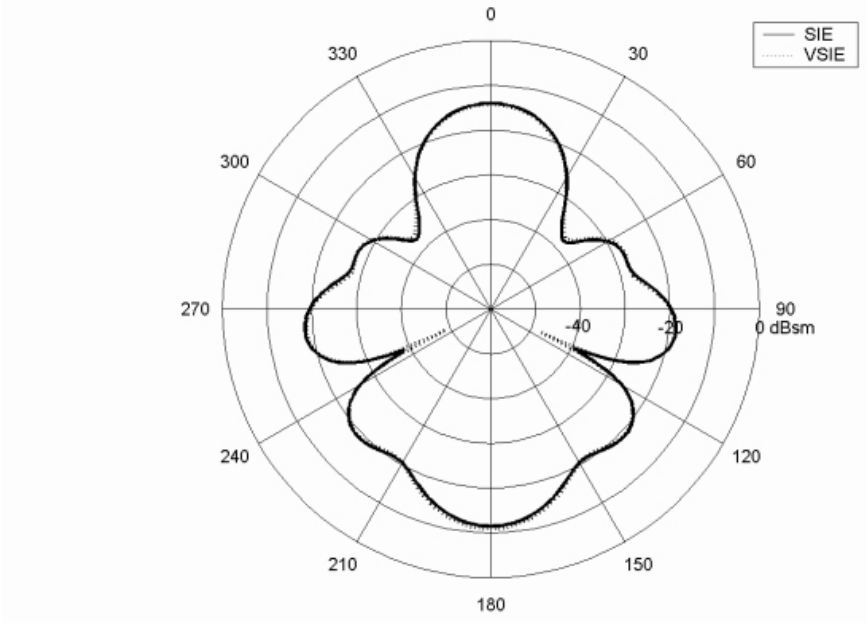

(b) HH−polarization

Figure 6.9: Monostatic RCSs of a PEC-dielectric cylinder ($a = 5.08$ cm, $b = 10.16$ cm, $d = 7.62$ cm, and $\epsilon_r = 2.6$) at 3 GHz. (a) VV−polarization. (b) HH−polarization.

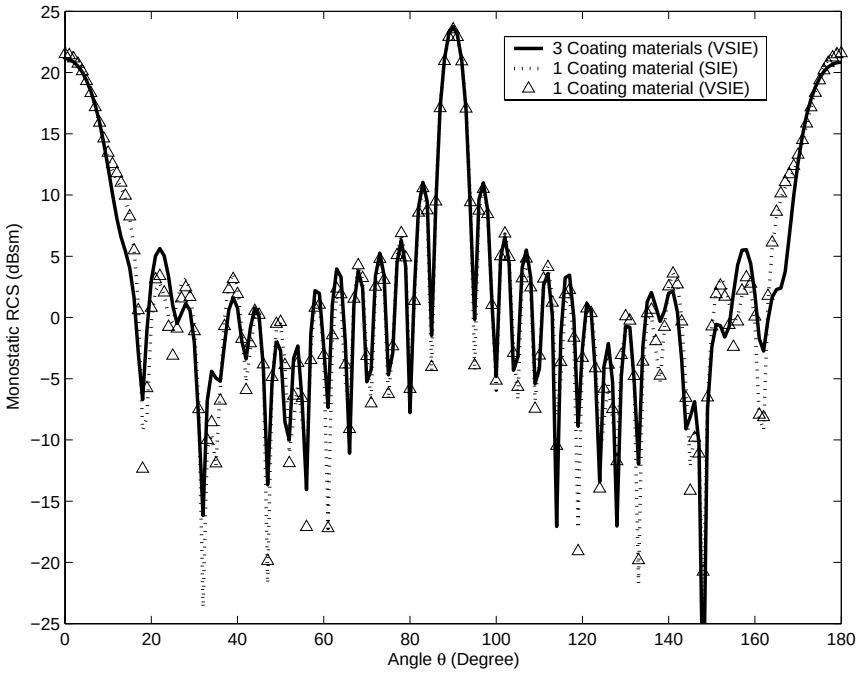

(a) VV−polarization

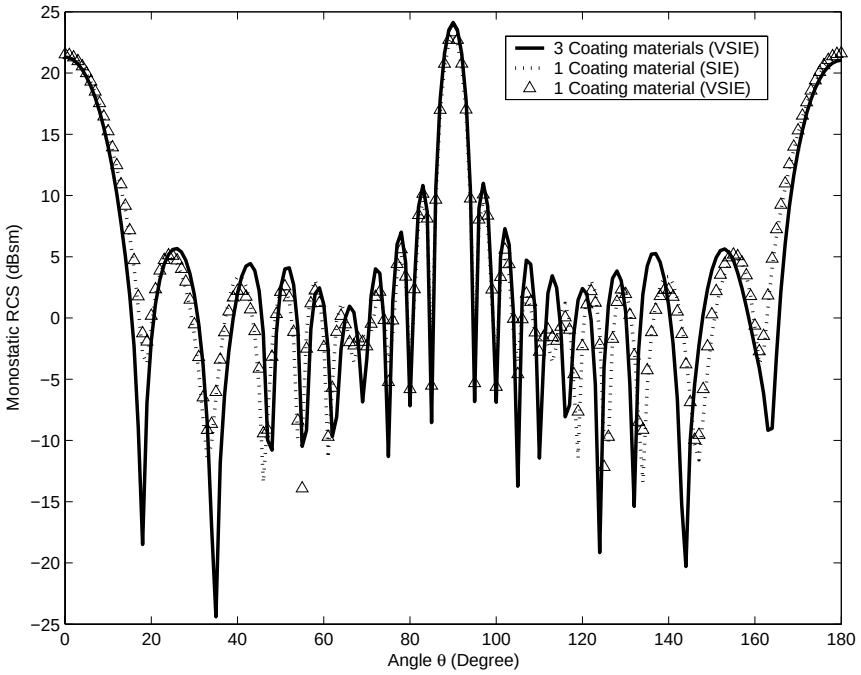

(b) HH−polarization

Figure 6.10: Monostatic RCSs of a conducting cylinder coated with three different dielectric materials ($\epsilon_{r1} = 2.0$, $\epsilon_{r2} = 2.2 - j0.4$, $\epsilon_{r3} = 2.4 - j0.2$) at 300 MHz. (a) VV−polarization. (b) HH−polarization.

with 3 different lossy dielectric materials. The coating layer is 0.05 λ thick and is divided into 3 sections evenly with same height. The relative permittivity ϵ_r of each sections are 2.0, $2.2 - j0.4$ and $2.4 - j0.2$, respectively. The monostatic RCSs for VV− and HH−polarizations are computed at 300 MHz with 105,370 unknowns. The results are shown in Fig. 6.10. To verify the result, the monostatic RCS of the coated cylinder with relative permittivity ϵ_r set equal to 1.44 have been also computed and compared with the solution obtained using the SIE method. The results are shown in Fig. 6.10. An excellent agreement is observed between the results.

The last example we consider is a thin conducting trapezoidal plate with coating on its sides. The dimension of the trapezoidal plate is shown in Fig. 6.11 and the coating layer has relative permittivity of $\epsilon_r = 4.5 - j9.0$. The monostatic RCSs for VV− and HH−polarizations in the $XY-$ and $XZ-$planes are computed at 1 GHz with 60,253 unknowns. The corresponding results are shown in Fig. 6.12. A good agreement with published results [88, 90] is observed.

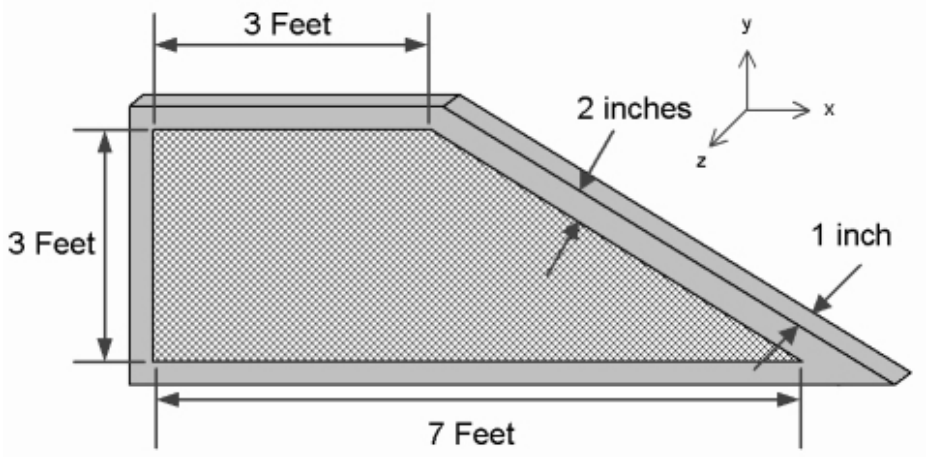

Figure 6.11: The geometry of trapezoidal plate with coating on its sides. The coating material has a relative permittivity, $\epsilon_r = 4.5 - j9.0$.

Table 6.3 shows the comparisons between the memory used by the AIM and the estimated memory for the MoM to compute the examples. For all examples except for Example 2, the saving in memory is more than 95%. For Example 2, the volume of the entire dielectric cylinder is discretized using tetrahedral cells and

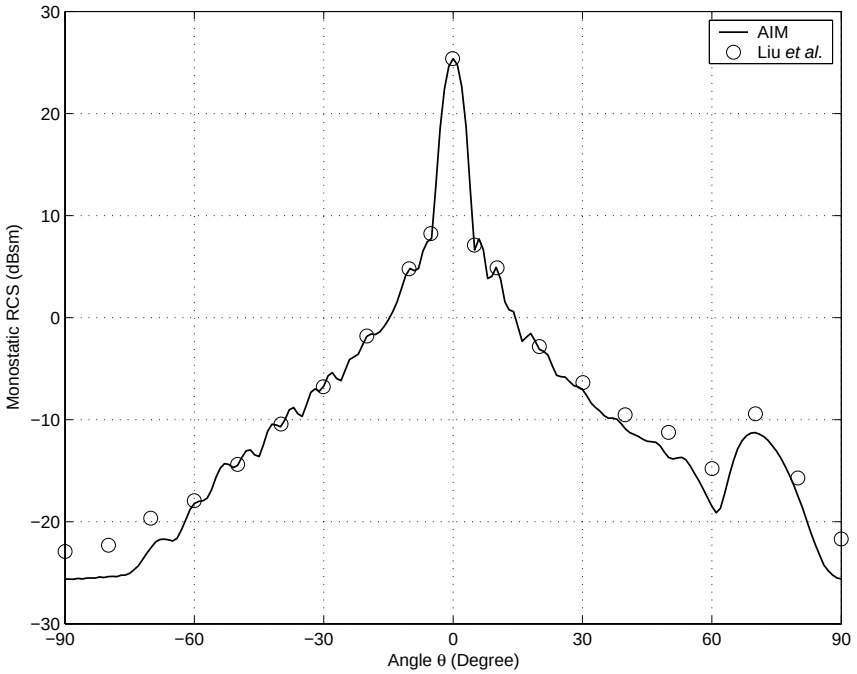

(a) VV−polarization in XZ−plane

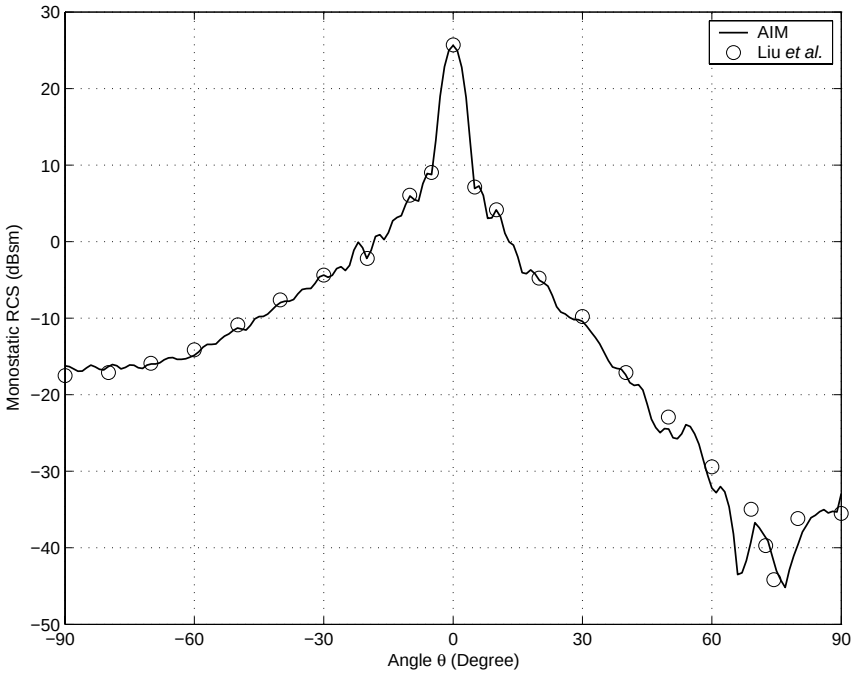

(b) HH−polarization in XZ−plane

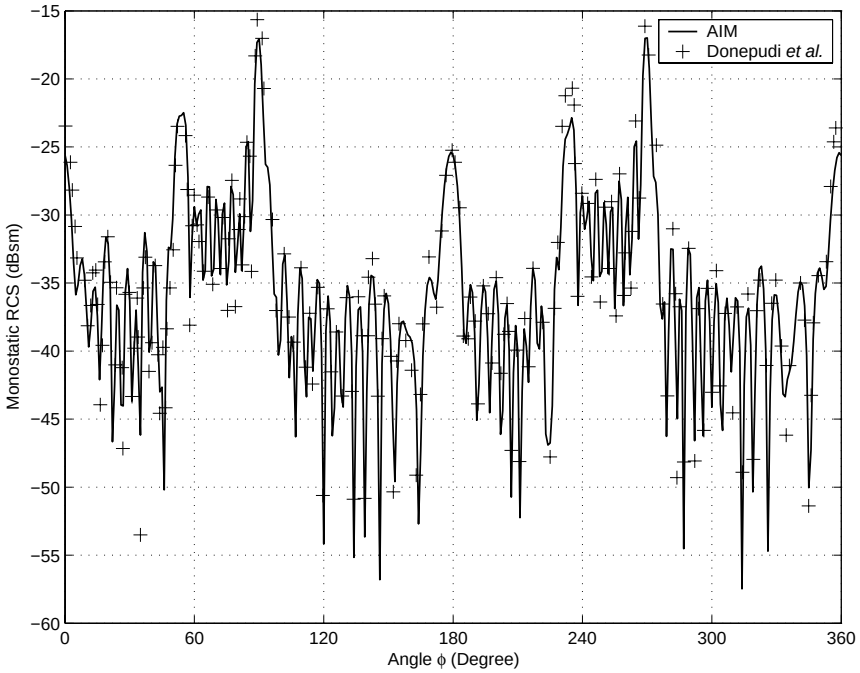

(c) VV−polarization in XY−plane

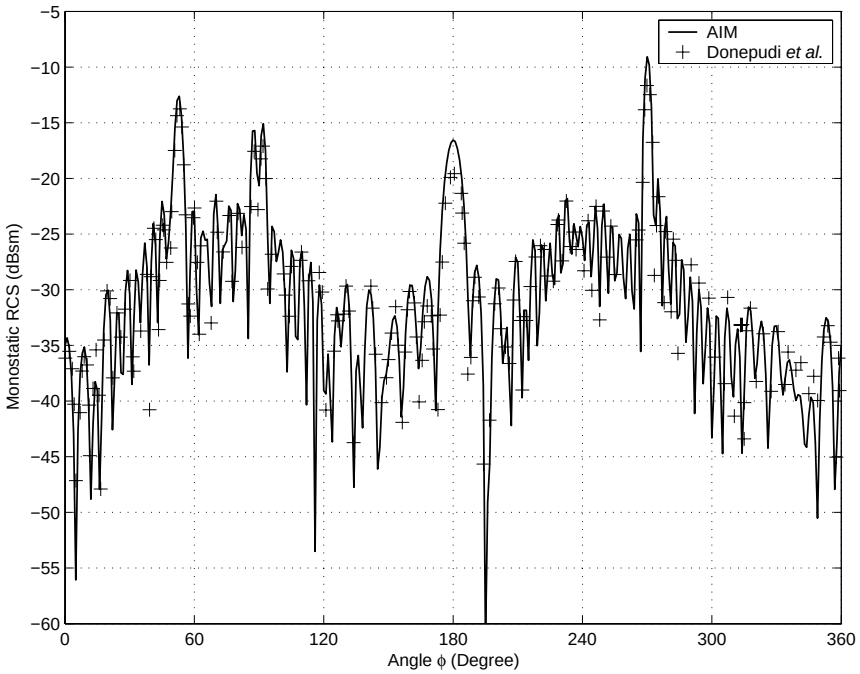

(d) HH−polarization in XY−plane

Figure 6.12: Monostatic RCSs of a trapezoidal conducting plate with coated sides at 1 GHz. (a) VV−polarization in XZ−plane. (b) HH−polarization in XZ−plane. (c) VV−polarization in XY−plane. (d) HH−polarization in XY−plane.

hence more unknowns and near-zone elements are involved.

Table 6.4 shows the CPU time taken by the AIM to solve the examples. The estimated CPU time for the MoM is also shown for comparison. We find that the overall time saving is significant especially for the Examples 3 and 4.

Table 6.3: Comparison of memory requirement between the AIM and the MoM in solving electromagnetic scattering problems of composite conducting and dielectric objects characterized using the VSIE.

Example	Unknowns, N	AIM, M_{AIM}(MB)	MoM, M_{MoM}(GB)	M_{AIM}/M_{MoM}
Coated conducting sphere	31,174	139.16	7.24	1.88%
Conducting-dielectric cylinder	11,864	139.96	1.05	13.03%
Coated cylinder	105,370	417.02	82.72	0.49%
Trapezoidal conducting plate	60,253	286.28	27.05	1.03%

Note: 1 KB = 1,024 Bytes, 1 MB = 1,024 KB and 1 GB = 1,024 MB

Table 6.4: Comparison of CPU time between the AIM and the MoM in solving electromagnetic scattering problems of composite conducting and dielectric objects characterized using the VSIE.

Example	Unknowns, N	AIM, T_{AIM}(sec.)	Estimated MoM, T_{MoM}(sec)
Coated conducting sphere	31,174	68	379
Conducting-dielectric cylinder	11,864	362	583
Coated cylinder	105,370	751	14,434
Trapezoidal conducting plate	60,253	860	8,205

Chapter 7

Preconditioner – Further Acceleration to the Solution

7.1 Introduction

A non-uniform mesh will usually produce ill-conditioned matrix. The ill-conditioned matrix will cause the solution slow to converge, or even fail to converge. To overcome this problem, preconditioning matrix or preconditioner can be used to improve the condition number of a matrix and accelerate the convergence rate of the solution [91–97]. It is applied to transform the original matrix into another matrix, which is easier to be solved by an iterative solver. The solution of the transformed matrix is identical to the solution of the original matrix. Mathematically, we pre-multiply the matrix equation by the preconditioning matrix $\overline{\boldsymbol{M}}^{-1}$ to obtain a preconditioned matrix equation

$$\overline{\boldsymbol{M}}^{-1}\overline{\boldsymbol{Z}}\boldsymbol{I} = \overline{\boldsymbol{M}}^{-1}\boldsymbol{V}. \tag{7.1}$$

Ideally, if $\overline{\boldsymbol{M}}^{-1} = \overline{\boldsymbol{Z}}^{-1}$, then the matrix equation is solved in one step. However it is impractical to construct such a preconditioner as it is indeed computing the inverse of $\overline{\boldsymbol{Z}}$ which requires $O(N^3)$ operations. Practically, the preconditioner

must be simple to construct and inexpensive to store. It is also requires that the computed $\overline{\boldsymbol{M}}^{-1}$ can approximate $\overline{\boldsymbol{Z}}^{-1}$ and hence improves the condition number of the $\overline{\boldsymbol{Z}}$.

In previous chapters, the AIM has been successfully implemented to solve the electromagnetic scattering problems of different type of scatterers. However, we did not discuss the convergence rate of the solutions. In this chapter, we will discuss four preconditioning techniques that can be used to accelerate the solution of the scattering problems. All preconditioners are constructed by using the near-zone matrix $\overline{\boldsymbol{Z}}^{\text{near}}$ that generated by our AIM implementation [98–100].

7.2 Diagonal and Block Diagonal Preconditioner

The diagonal preconditioner (DP) is a diagonal matrix whose diagonal elements are identical to those of the impedance matrix. It is simple to construct and trivial to invert. Moreover, it only requires a row vector of size N to store its matrix elements. The DP can be extracted directly during the construction of $\overline{\boldsymbol{Z}}^{\text{near}}$. Fig. 7.1 depicts the sparsity pattern of DP.

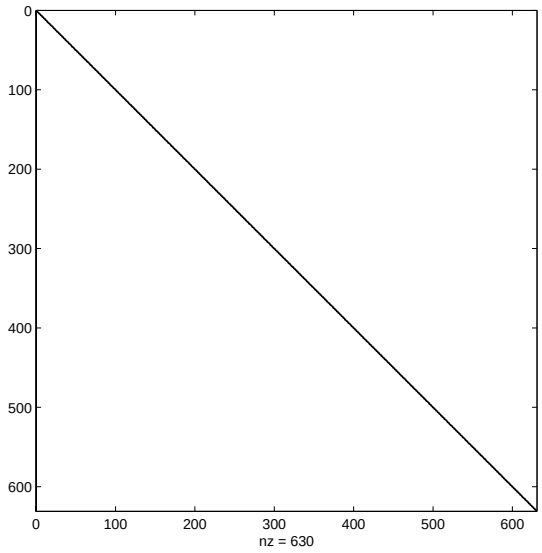

Figure 7.1: Sparsity pattern of diagonal preconditioner.

Another preconditioner closely related to the diagonal preconditioner is the block diagonal preconditioner (BDP). The BDP is a matrix that retains the block diagonal partitions of the impedance matrix $\overline{\boldsymbol{Z}}$. The block diagonal partitions can be obtained using different methods. In our implementation, we have partitioned the Cartesian grids into blocks with the block size equal to the near-zone threshold distance. The fictitious blocks correspond to the block matrices in the BDP. Every block matrix is constructed by computing the interactions among the elements within the block. Then the BDP can be obtained by simply taking the inverse of the block matrices individually. The sparsity pattern of a typical BDP is shown in Fig. 7.2.

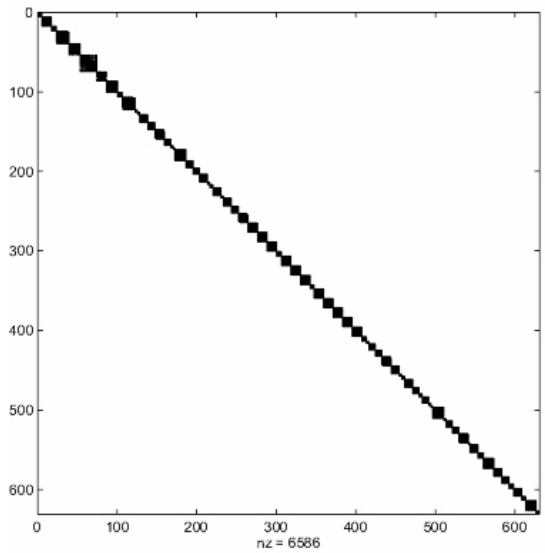

Figure 7.2: Sparsity pattern of block diagonal preconditioner.

7.3 Zero Fill-In Incomplete LU Preconditioner

The direct LU decomposition of $\overline{\boldsymbol{Z}}^{\text{near}}$ may result in a dense matrix preconditioner, which is too expensive to be stored. In contrast, the incomplete LU (ILU) decomposition only factorizes the nonzero entries of the $\overline{\boldsymbol{Z}}^{\text{near}}$. The preconditioner based on the ILU decomposition will have identical sparsity pattern as that of $\overline{\boldsymbol{Z}}^{\text{near}}$. We have implemented the IKJ version of ILU decomposition obtained from [91].

Let the $NZ(\overline{\boldsymbol{Z}}^{\text{near}})$ represent the non-zero entries of the sparse matrix $\overline{\boldsymbol{Z}}^{\text{near}}$, the preconditioner can be constructed using Algorithm 6.

for *i=2,...,n* **do**
  for *k=1,...,i–1* **and** (i,k) in $NZ(\overline{\boldsymbol{Z}}^{near})$ **do**
    compute $z_{ik} = z_{ik}/z_{kk}$
    for *j=k+1,...,n* **and** (j,k) in $NZ(\overline{\boldsymbol{Z}}^{near})$ **do**
      compute $z_{ij} = z_{ij} - z_{ik}z_{kj}$
    end
  end
end

Algorithm 6: Zero Fill-In Incomplete LU, ILU(0).

We refer the preconditioner generated by this algorithm as ILU(0), as no additional elements add into the preconditioner during the factorization. Fig. 7.3 illustrates the sparsity pattern of a ILU(0).

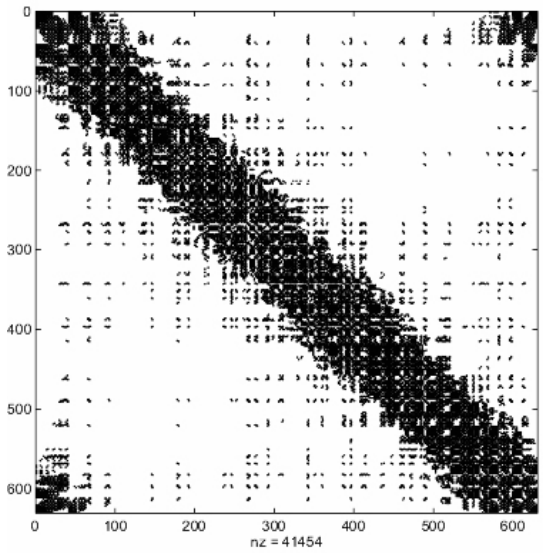

Figure 7.3: Sparsity pattern of ILU(0).

7.4 Incomplete LU with Threshold Preconditioner

The ILU(0) has an identical sparsity pattern as that of $\overline{\boldsymbol{Z}}^{\text{near}}$ and this is considered the major drawback of this method as it needs a large amount of memory for

storage. To overcome the shortcoming of ILU(0), we have considered a variation of ILU decomposition, ILU with threshold (ILUT). The ILUT allows additional rules to control the computational cost and storage, and these let the user save the scarce memory for other usages. We have implemented ILUT(p, τ) given in Ref. [91, 101], which can be constructed using Algorithm 7.

```
for i=1,...,n do
    w = z_{i*}
    for k=1,...,i-1  and when w_k ≠ 0 do
        compute w_k = w_k/z_{kk}
        apply dropping rule 1 to w_k
        if w_k ≠ 0 then
            w = w − w_k u_k
        end
    end
    apply dropping rule 2 to w
    l_{i,j} = w_j for j = 1, ..., i − 1
    u_{i,j} = w_j for j = i, ..., n
    w = 0
end
```

Algorithm 7: Incomplete LU with threshold, ILUT(p, τ).

The dropping rule 1 will drop the element w_k if $|w_k|$ is less than the relative tolerance τ_i, which is obtained by multiplying τ by the norm of i-th row, $||z_{i*}||$. When applying the dropping rule 2, the element in w is dropped if it is less than τ_i and then only p largest elements in the lower and upper parts of the row are kept. The parameter τ controls the computational cost while the parameter p controls the overall memory required to store the preconditioner. These parameters can be adjusted to meet different needs. It is also noted that the ILU(0) is a special case of ILUT where the dropping rules apply to the elements that are in positions not belonging to the sparsity pattern of $\overline{\boldsymbol{Z}}^{\text{near}}$. For simplicity purpose, we have let $\tau = 0$ in our implementation and only varied the value of p to control the storage size of the preconditioner. Fig. 7.4(a) and Fig. 7.4(b) illustrate the sparsity patterns of ILUT(5) and ILUT(40), respectively.

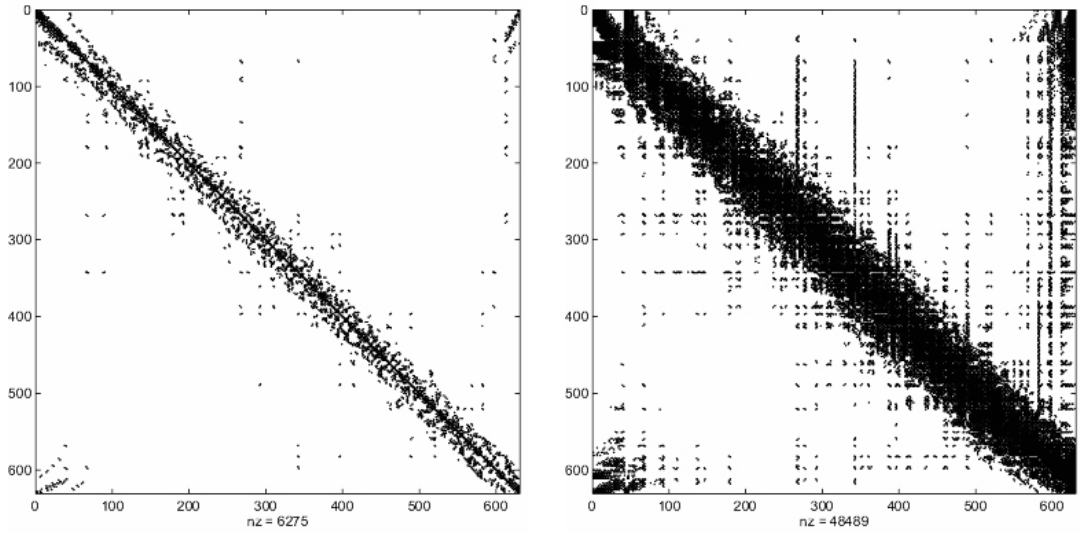

(a) ILUT(5) (b) ILUT(40)

Figure 7.4: Sparsity patterns of ILUT.

7.5 Performance of Preconditioners

In this section, we will present numerical examples to illustrate the performance of the preconditioners implemented in our AIM-accelerated GMRES iterative solver. Here we will demonstrate the capability of the preconditioners in solving the electromagnetic scattering problems formulated using the SIE method and the VSIE method, which represent the two classes of integral equation method used in our work.

7.5.1 Surface Integral Equation

In this section, we will only consider the scattering problem of metallic structures as the preconditioners can be easily modified to cope with other types of scatterers. The first testing object that we have considered is the NASA almond [85]. The maximum dimensions of the almond along the $x-$, $y-$ and $z-$axes are 1 m, 0.4 m and 0.13 m, respectively. The geometry of the NASA almond is shown in Fig. 7.5. The discretization of the object using triangular patches has resulted in 3,510 unknowns. We compute the HH$-$polarization bistatic RCSs of the NASA almond at

900 MHz with the illuminating plane wave incident upon the tip. The convergence characteristics of the solution process without a preconditioner and with different preconditioners are shown in Fig. 7.6.

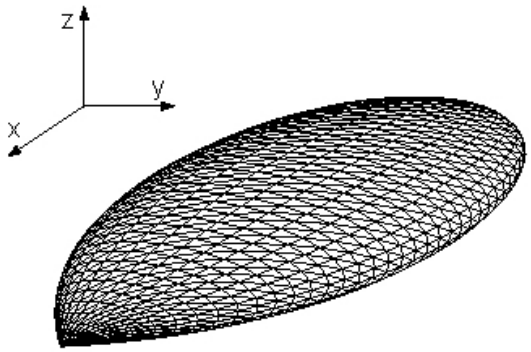

Figure 7.5: Geometry of a NASA almond.

In Fig. 7.6(a), we observe that the DP improves the convergence rate slightly while the BDP shows better improvement in convergence rate as it converges to 10^{-3} in 27 iterations. The ILU(0) preconditioner gives the best results as it converges to 10^{-5} within only 13 iterations. Fig. 7.6(b) shows the convergence rate of the ILU based preconditioners. We find that the ILUT(40) performs better than the other two ILUT preconditioners and produces comparable performance to the ILU(0). The good performance of ILUT(40) over the other two ILUT preconditioners is expected as it contains more matrix elements. However it is surprised that the ILU(0) is just slightly better than ILUT(40) as it contains about 6 times more elements than the latter.

The second example we considered is a metallic generic airplane. The airplane model used in this example is identical to the one shown in Fig. 4.6. The complicated structure has resulted in non-uniform meshes, especially at the corner. The VV−polarization bistatic RCSs are computed with the plane wave incident from the top of the airplane. The convergence characteristics of the solution process without a preconditioner and with different preconditioners are shown in Fig. 7.7.

In Fig. 7.7(a), we observe similar convergence behavior as in the previous exam-

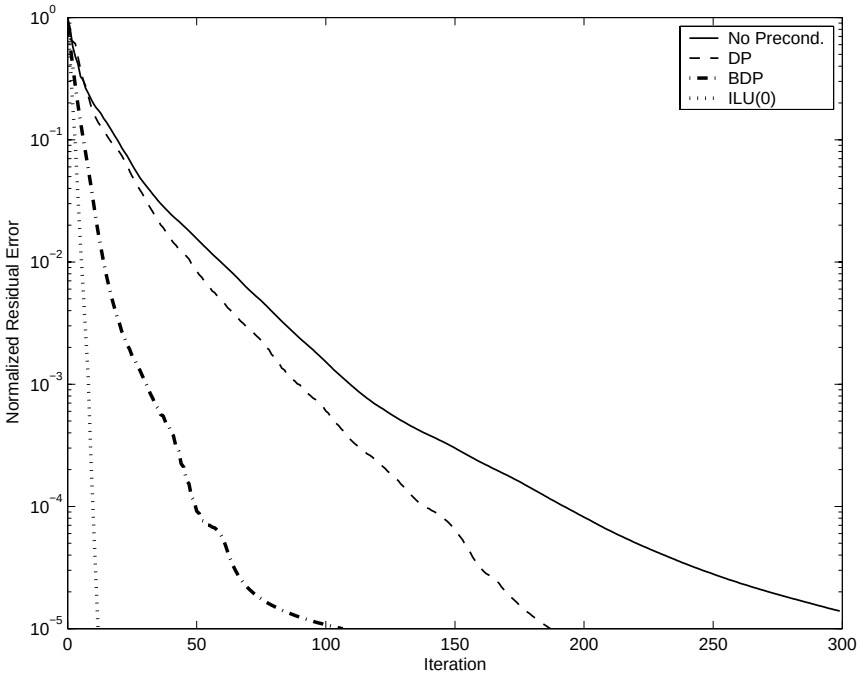

(a) Different preconditioners

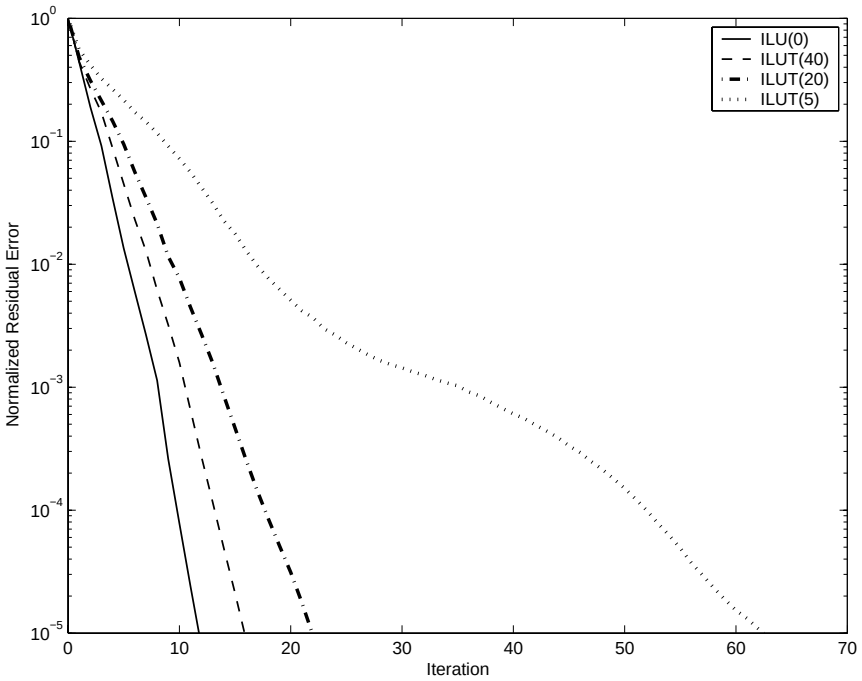

(b) ILU based preconditioners

Figure 7.6: Comparison of the convergence rates for the scattering by a NASA almond. (a) Different preconditioners. (b) ILU based preconditioners.

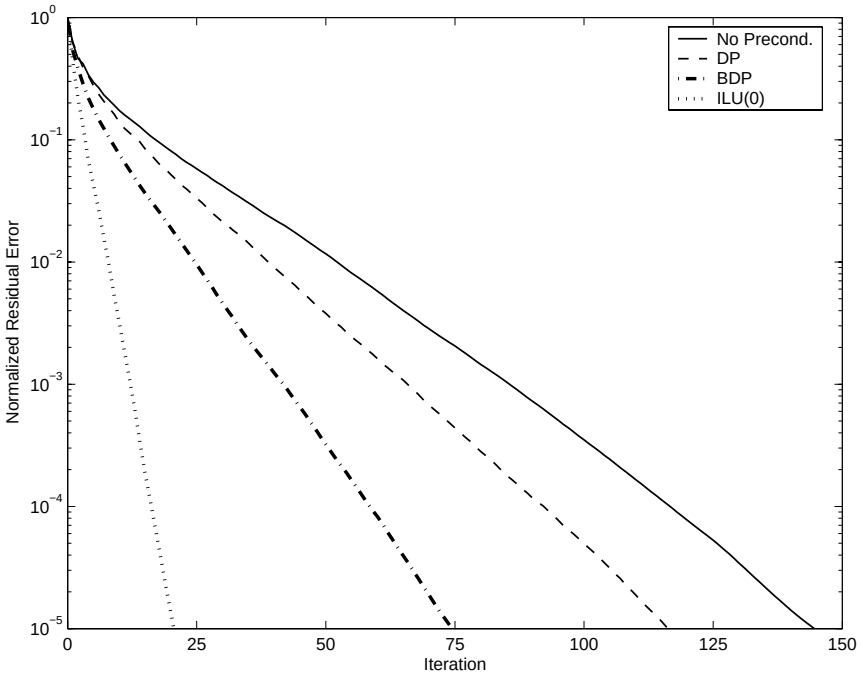

(a) Different preconditioners

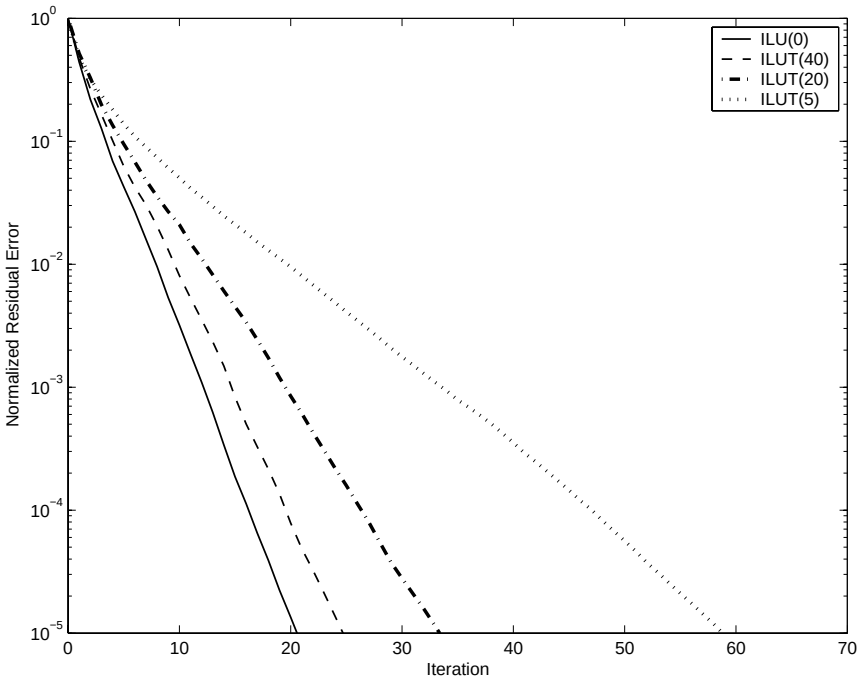

(b) ILU based preconditioners

Figure 7.7: Comparison of the convergence rates for the scattering by a generic airplane. (a) Different preconditioners. (b) ILU based preconditioners.

ple. The DP improves the convergence rate slightly while the BDP shows better improvement in convergence rate as it converges to 10^{-3} in 90 iterations. The ILU(0) preconditioner gives the best results as it converges to 10^{-5} within only 25 iterations. Fig. 7.7(b) shows the convergence rate of the ILU based preconditioners. We find that the ILUT(40) performs better than the other two ILUT preconditioners and produces comparable performance to the ILU(0). It is expected as the ILUT(40) contains more matrix elements than the other two ILUT preconditioners.

Lastly, we compare the performance of these preconditioners in another larger testing case. The scattering object considered in this case is a conesphere whose dimensions are 69 cm $\times$ 7.5 cm $\times$ 7.5 cm [85]. The geometry of the conesphere is shown in Fig. 7.8. The conesphere is discretized using triangular patches and resulted in 64,287 unknowns. We compute the VV$-$polarization bistatic RCSs of the object at 9 GHz with the plane wave incident upon the tip. The convergence characteristics of these preconditioners are shown in Fig. 7.9(a).

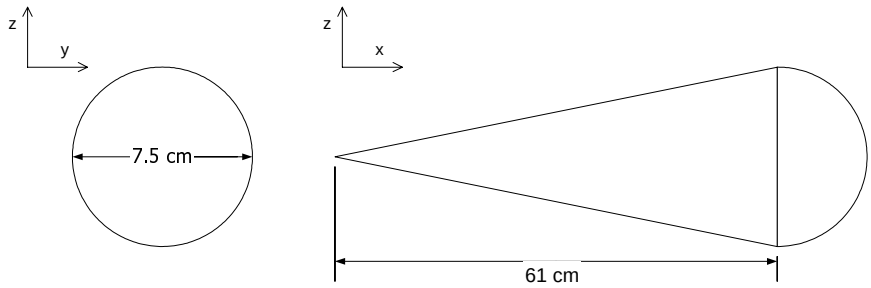

Figure 7.8: Geometry of a metallic conesphere.

The ILU(0) preconditioner outperforms the DP and BDP by reducing the normalized residual error to 10^{-5} in 25 iterations. Again, the performances of the ILUT preconditioners are compared with ILU(0) as shown in Fig. 7.9(b).

Table 7.1 summarizes the performance of the preconditioners in characterizing the electromagnetic scattering by metallic objects using the SIE method. The number of iterations is recorded when the normalized residual error less than 10^{-3} is achieved. All the recorded timings have been rounded to the nearest integer. The

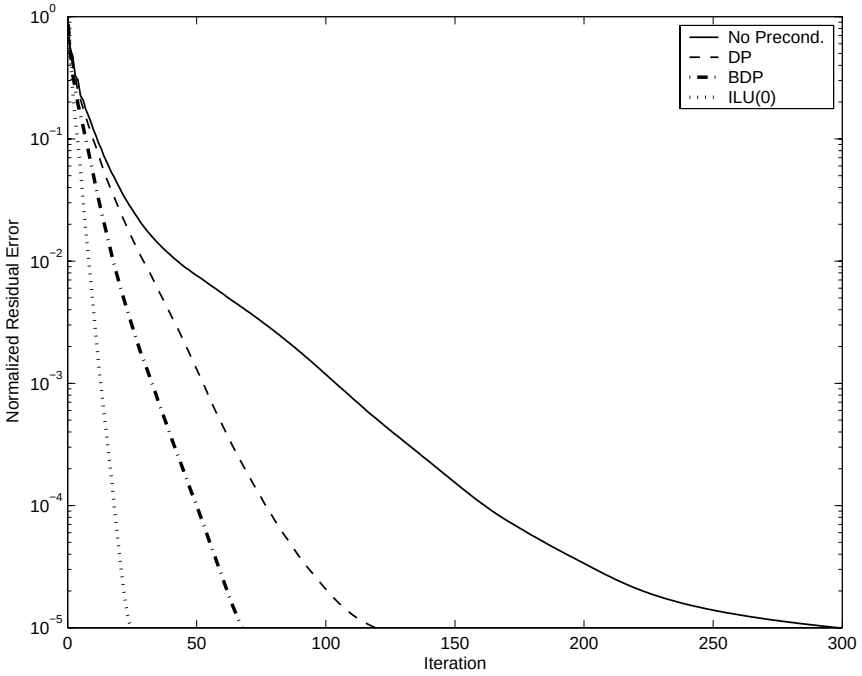

(a) Different preconditioners

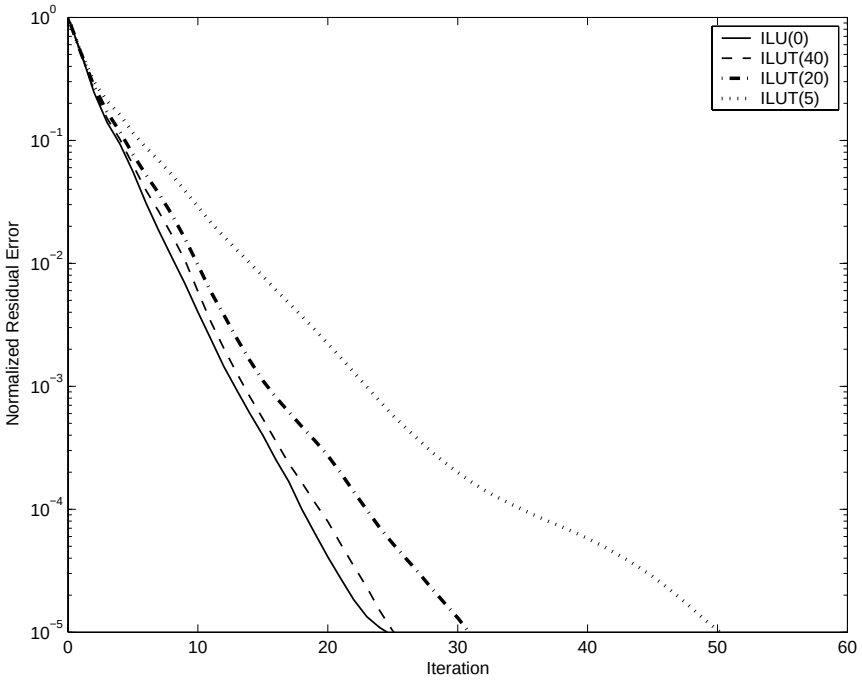

(b) ILU based preconditioners

Figure 7.9: Comparison of the convergence for the scattering by a conesphere. (a) Different preconditioners. (b) ILU based preconditioners.

time used to construct diagonal preconditioner is not included as it is extracted directly from the $\overline{\boldsymbol{Z}}^{\text{near}}$.

From Table 7.1, we observe that the great improvement due to the ILU(0) comes at a price. It consumes more memory than other preconditioners. However, the use of ILU(0) is justified by the overall time saving. It has reduced the total time needed to analyze electromagnetic scattering by the testing objects. We also observe that the ILU based preconditioners produce overall better result and ILUT(40) produces comparable results to the ILU(0) with less memory requirement. The time saving benefited from the preconditioners will be considerable when it is used to compute the monostatic RCS of an electrically large object.

Table 7.1: Performance of the preconditioners in solving electromagnetic scattering problems characterized using the SIE.

Unknowns, N	Preconditioning techniques	Storage	Setup time (sec.)	Number of Iteration, N_{iter}	Solution time (sec.)
3510 (Example 1)	No preconditioner	–	–	110	14
	DP	27 KB	–	90	12
	BDP	2 MB	2	31	4
	ILU(0)	10 MB	4	9	2
	ILUT(40)	2 MB	2	11	2
	ILUT(20)	1 MB	1	14	2
	ILUT(5)	274 KB	1	36	5
6459 (Example 2)	No preconditioner	–	–	86	30
	DP	51 KB	–	66	24
	BDP	2 MB	2	42	14
	ILU(0)	9 MB	3	13	5
	ILUT(40)	4 MB	3	15	5
	ILUT(20)	2 MB	2	20	7
	ILUT(5)	503 KB	1	34	12
64287 (Example 3)	No preconditioner	–	–	104	652
	DP	502 KB	–	53	330
	BDP	19 MB	24	33	211
	ILU(0)	90 MB	52	13	81
	ILUT(40)	38 MB	25	14	85
	ILUT(20)	19 MB	17	16	97
	ILUT(5)	5 MB	10	23	140

Note: 1 KB = 1,024 Bytes and 1 MB = 1,024 KB

7.5.2 Volume-Surface Integral Equation

In this section, the performance of the preconditioners in solving the scattering problem of composite conducting and dielectric objects formulated using the VSIE method will be presented. Two examples will be presented in this section to demonstrate the applicability of these preconditioners in solving the VSIE. The first example is a coated metallic sphere. The core of the sphere is having a radius of 0.8 m and the thickness of the coating layer is 0.2 m. We compute the VV−polarization bistatic RCSs at 300 MHz of the sphere with 31,174 unknowns. The convergence characteristics of the solution process with different preconditioners are shown in Fig. 7.10.

In Fig. 7.10(a), we find that the convergence rate by ILU(0) preconditioner is amazing as it reduces the normalized residual error 10^{-5} within 10 iterations. The comparison of the performance between the ILU(0) and the ILUT preconditioners in solving this problem is shown in Fig. 7.10(b). The ILU(0) again performs better than the ILUT preconditioners. However, the result is expected as the former contains more elements. Nevertheless we have observed that the ILUT(40) produces comparable results to the ILU(0).

Next, we compare the performance of these preconditioners in another testing case which consists of 105,370 unknowns. The scattering object considered in this case is a coated cylinder which has been described in Chapter 7. We compute the VV−polarization bistatic RCSs of the cylinder at 300 MHz. The convergence characteristics of these preconditioners are shown in Fig. 7.11. In Fig. 7.11(a), we see that the ILU(0) preconditioner outperforms the DP and BDP by reducing the normalized residual error to 10^{-5} in 25 iterations. The comparison of the performance between the ILU(0) and ILUT preconditioners is shown in Fig. 7.11(b). Again, we observe that the ILU(0) outperforms all ILUT preconditioners; however, the ILUT(40) produces comparable results with less storage requirement.

We summarize in Table 7.2 the performance of the preconditioners in solving the electromagnetic scattering using the VSIE. The number of iterations is recorded

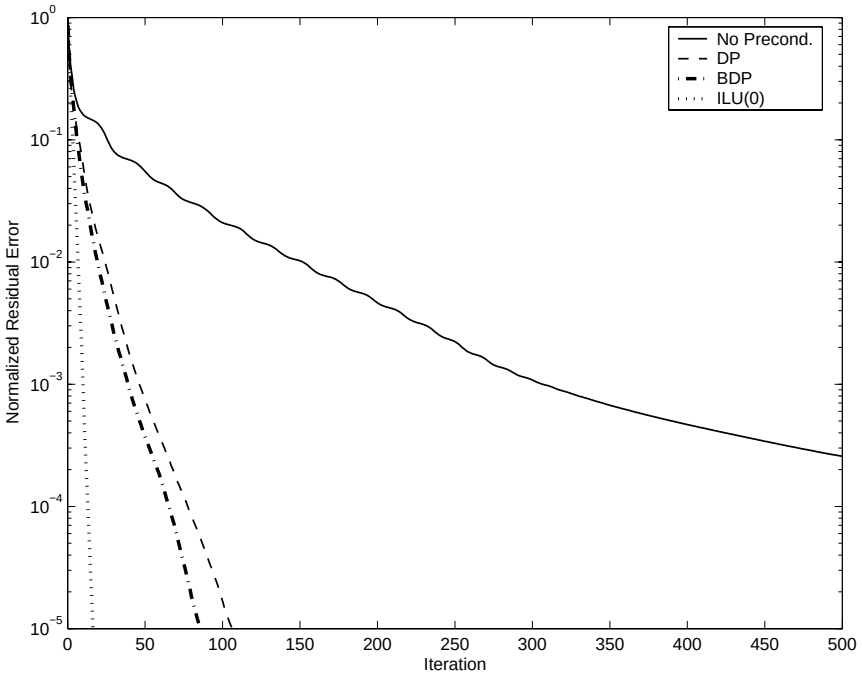

(a) Different preconditioners

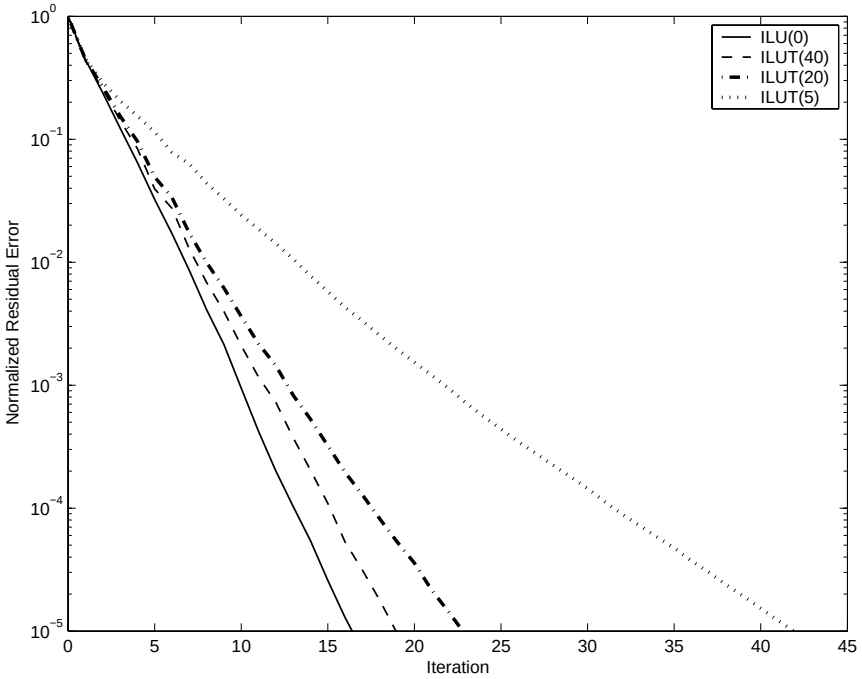

(b) ILU based preconditioners

Figure 7.10: Comparison of the convergence for the scattering by a coated sphere. (a) Different preconditioners. (b) ILU based preconditioners.

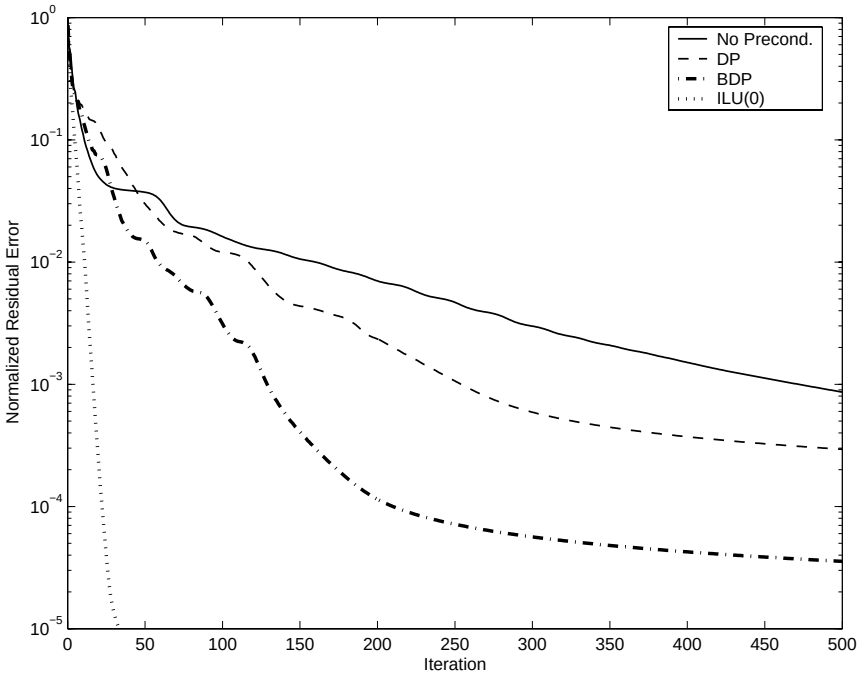

(a) Different preconditioners

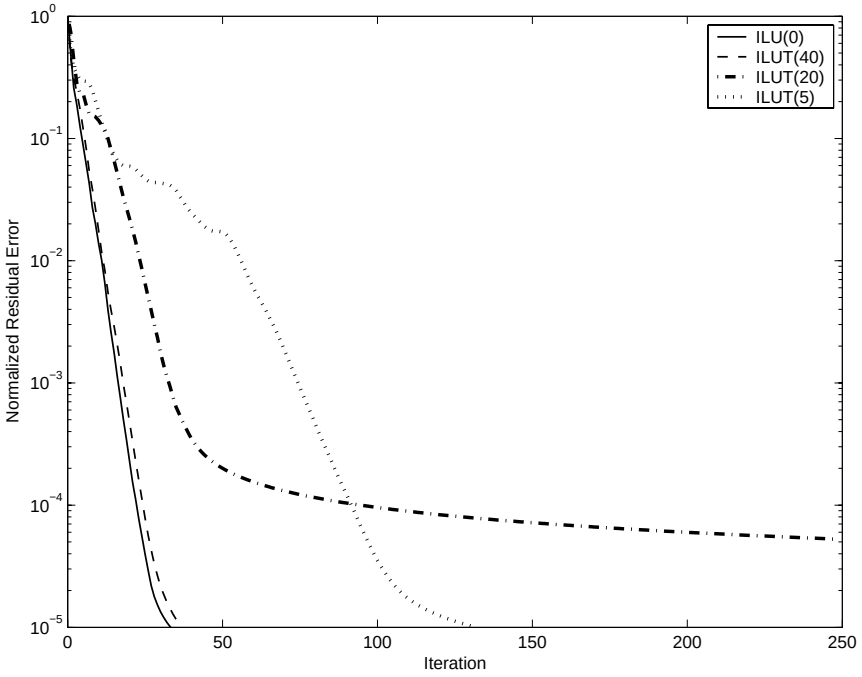

(b) ILU based preconditioners

Figure 7.11: Comparison of the convergence for the scattering by a coated cylinder. (a) Different preconditioners. (b) ILU based preconditioners.

when the normalized residual error less than 10^{-3} is achieved. The recorded timings have been rounded to the nearest integer. The time used to construct diagonal preconditioner is not included as it is extracted directly from the $\overline{\boldsymbol{Z}}^{\text{near}}$.

In Table 7.2, we find that the ILU(0) outperforms the other preconditioners in terms of total number of iterations. It consumes more memory than other preconditioners. However the ILUT(40) is actually the best performer as it uses the least time to produce the solution. The performance of ILU(0) is greatly affected by the its matrix size as the additional time is required to multiply the ILU(0) to the impedance matrix in every iteration.

Table 7.2: Performance of the preconditioners in solving electromagnetic scattering problems characterized using the VSIE.

Unknowns, N	Preconditioning techniques	Storage	Setup time (sec.)	Number of Iteration, N_{iter}	Solution time (sec.)
31174 (Example 1)	No preconditioner	–	–	307	343
	DP	27 KB	–	47	53
	BDP	14 MB	56	39	46
	ILU(0)	125 MB	74	10	18
	ILUT(40)	19 MB	18	12	15
	ILUT(20)	9 MB	16	13	16
	ILUT(5)	2 MB	10	22	26
105370 (Example 2)	No preconditioner	–	–	472	1757
	DP	823 KB	–	254	949
	BDP	65 MB	257	129	508
	ILU(0)	370 MB	215	17	96
	ILUT(40)	63 MB	65	19	78
	ILUT(20)	32 MB	38	32	131
	ILUT(5)	8 MB	25	75	289

Note: 1 KB = 1,024 Bytes and 1 MB = 1,024 KB

Chapter 8

Conclusion and Suggestions for Future Work

8.1 Conclusion

In this thesis, a grid based fast integral equation solver for electrically large objects is presented. The fast solver is developed to solve the electromagnetic scattering problem of arbitrarily shaped 3-D objects made of metallic, dielectric or composite metallic and dielectric structures. The scattering problems are characterized using the surface integral equation method, the volume integral equation method, and the hybrid volume-surface integral equation method.

The method of moments (MoM) is applied to discretize the integral equations and solve the resultant matrix equation using an iterative solver. However, the MoM is inadequate when used to solve large-scale electromagnetic problems, especially those structures with complex dielectric properties. The AIM is used to accelerate the matrix-vector multiplication in iterative solvers and to reduce the memory requirement for matrix storage. In Chapter 4, we have used the AIM to solve the electromagnetic scattering and radiation problems of metallic structures, which is formulated by using the surface integral equation (SIE). Numerical exam-

ples have been presented to show the accuracy and efficiency of our code in solving the electromagnetic problems of metallic structures.

In Chapter 5, we have formulated the scattering problems of dielectric objects using the SIE method and the volume integral equation (VIE) method, separately. The original AIM has been modified to cope with the additional information needed for the dielectric materials. For the scattering problems formulated using the SIE method, additional fast Fourier transform (FFT) needs to be carry out to account for the material properties. On the other hand, formulating the scattering problem using the VIE will normally result in a matrix equation with a large number of unknowns. Hence a proper choice of the type of integral equation methods is necessary. We have presented several numerical examples to demonstrate the accuracy and applicability of the AIM in solving the scattering problems of dielectric objects using the SIE method and the VIE method.

We have also considered the electromagnetic scattering by composite conducting and dielectric objects in Chapter 6. The scattering problems are formulated using the SIE method and the hybrid volume-surface integral equation (VSIE) method, separately. The SIE method is appropriate for the scatterer with piecewise homogeneous dielectric material while the VSIE is preferred for the scatterer with inhomogeneous dielectric material. We have used the modified AIM to analyze the electromagnetic scattering by a large composite conducting and dielectric object. Numerical examples are presented to show the capability and efficiency of our AIM implementation in solving the scattering problems formulated using the SIE method and the VSIE method.

Lastly in Chapter 7, several preconditioning techniques have been incorporated into our AIM code to accelerate the convergence rate of the solutions. The diagonal preconditioner is the simplest preconditioner but it produces only a marginal improvement. The block diagonal preconditioner is constructed using the elements in the block diagonal partition and it provides better convergence rate. Two preconditioners based on the incomplete LU (ILU) decomposition, i.e. zero fill-in ILU

(ILU(0)) and ILU with threshold (ILUT), have also been implemented in our code. The ILU(0) has provided the best convergence rate among the preconditioners investigated; however, it requires large matrix storage. The ILUT has been used to overcome the weakness of the ILU(0) by allowing additional rules to control the number of elements. In our experiment, we find that the ILUT(40) has produced comparable results to the ILU(0).

8.2 Recommendations for Future Work

As technology progresses rapidly in the area of computational electromagnetics, there is plenty of room for future studies. The following items represent some possible future work directions.

1. The simulation in this thesis was performed by using a personal computer (PC), in which the computing resources are limited. The size of problem can be solved is constrained by the available computing resources on the PC. By using parallel computing, it is possible to combine the computing resources of a cluster of personal computers to solve larger problems.

2. The basis functions used in this thesis are of low order. Higher-order basis functions enable the use of larger patches for the discretization and hence reduce the total number of unknowns. In addition, the higher-order basis functions are also able to increase the accuracy of the solution. By combining the higher-order basis functions with the AIM, we expect that the efficiency of the code can be increased.

3. The analyses in this thesis are performed in frequency domain, which implies each simulation will only produce results at a particular frequency. In order to perform the analysis over a wide range of frequencies, we can resort to the time domain analysis. By adopting the time domain AIM analysis, we are able to perform a fast frequency sweep analysis for a large-scale scatterer.

References

[1] K. K. Mei and J. V. Bladel, "Scattering by perfectly conducting rectangular cylinders," *IEEE Trans. Antennas Propagat.*, vol. 11, no. 2, pp. 185–192, March 1963.

[2] K. K. Mei, "On the integral equations of thin wire antennas," *IEEE Trans. Antennas Propagat.*, vol. 13, no. 3, pp. 374–378, May 1965.

[3] M. G. Andreasen, "Scattering from parallel metallic cylinders with arbitrary cross sections," *IEEE Trans. Antennas Propagat.*, vol. 12, no. 6, pp. 746–754, Nov. 1964.

[4] M. G. Andreasen, "Scattering from bodies of revolution," *IEEE Trans. Antennas Propagat.*, vol. 13, no. 2, pp. 303–310, March 1965.

[5] J. H. Richmond, "Scattering by a dielectric cylinder of arbitrary cross section shape," *IEEE Trans. Antennas Propagat.*, vol. 13, no. 3, pp. 334–341, May 1965.

[6] J. H. Richmond, "Scattering by an arbitrary array of parallel wires," *IEEE Trans. Microwave Theory Tech.*, vol. 13, no. 4, pp. 408–412, July 1965.

[7] J. H. Richmond, "TE-wave scattering by a dielectric cylinder of arbitrary cross section shape," *IEEE Trans. Antennas Propagat.*, vol. 14, no. 4, pp. 460–464, July 1966.

[8] J. H. Richmond, "A wire-grid model for scattering by conducting bodies," *IEEE Trans. Antennas Propagat.*, vol. 14, no. 6, pp. 782–786, Nov. 1966.

[9] F. K. Oshiro and K. M. Mitzner, "Digital computer solution of three-dimensional scattering problem," in *Digest of IEEE Int. Antennas Propagat. Symp.*, vol. 5, Oct. 1967, pp. 257–263.

[10] R. F. Harrington and J. R. Mautz, "Straight wires with arbitrary excitation and loading," *IEEE Trans. Antennas Propagat.*, vol. 15, no. 4, pp. 502–515, July 1967.

[11] R. F. Harrington, *Field Computation by Moment Methods*. New York: MacMillan, 1968.

[12] L. V. Kantorovich and V. Krylov, *Approximate Methods of Higher Analysis*. New York, NY: John Wiley & Sons, 1964, translated from Russian.

[13] Y. U. Vorobev, *Method of Moments in Applied Mathematics*. New York, NY: Gordon & Breach, 1965, translated from Russian.

[14] K. S. H. Lee, L. Marin, and J. P. Castillo, "Limitation of wire-grid modelling of a closed surface," *IEEE Trans. Electromagn. Compat.*, vol. EMC-18, no. 3, pp. 123–129, Aug 1976.

[15] J. R. Mautz and R. F. Harrington, "Radiation and scattering from bodies of revolution," *Appl. Sci. Res.*, vol. 20, pp. 405–435, June 1969.

[16] J. R. Mautz and R. F. Harrington, "H-field, E-field and combined-field solution for conducting bodies of revolution," *A.E.U.*, vol. 32, no. 4, pp. 157–164, April 1978.

[17] D. L. Knepp and J. Goldhirsh, "Numerical analysis of electromagnetic radiation properties of smooth conducting bodies of arbitrary shapes," *IEEE Trans. Antennas Propagat.*, vol. 20, no. 3, pp. 383–388, May 1972.

[18] N. N. Wang, J. H. Richmond, and M. C. Gilreath, "Sinusoidal reaction formulation for radiation and scattering from condcting surfacs," *IEEE Trans. Antennas Propagat.*, vol. 23, no. 3, pp. 376–382, May 1975.

[19] E. H. Newman and D. M. Pozar, "Electromagnetic modeling of composite wire and surface geometries," *IEEE Trans. Antennas Propagat.*, vol. 26, no. 6, pp. 784–789, Nov. 1978.

[20] A. W. Glisson and D. R. Wilton, "Simple and efficient numerical methods for problems of electromagnetic radiation and scattering from surfaces," *IEEE Trans. Antennas Propagat.*, vol. 28, no. 5, pp. 593–603, Sept. 1980.

[21] S. M. Rao, D. R. Wilton, and A. W. Glisson, "Electromagnetic scattering by surfaces of arbitrary shape," *IEEE Trans. Antennas Propagat.*, vol. 30, no. 3, pp. 409–418, May 1982.

[22] A. J. Poggio and E. K. Miller, "Integral equation solutions of three dimensional scattering problems," in *Computer Techniques for Electromagnetics*, R. Mittra, Ed. New York: Permagon, 1973.

[23] Y. Chang and R. F. Harrington, "A surface formulation for characteristic modes of material bodies," *IEEE Trans. Antennas Propagat.*, vol. 25, no. 6, pp. 789–795, Nov. 1977.

[24] T. K. Wu and L. L. Tsai, "Scattering from arbitrarily-shaped lossy dielectric bodies of revolution," *Radio Sci.*, vol. 12, no. 5, pp. 709–718, Sept.–Oct. 1977.

[25] J. R. Mautz and R. F. Harrington, "Electromagnetic scattering from a homogeneous material body of revolution," *A.E.U.*, vol. 33, no. 2, pp. 71–80, Feb. 1979.

[26] K. R. Umashankar, A. Taflove, and S. M. Rao, "Electromagnetic scattering by arbitrary shaped three dimensional homogeneous lossy dielectric objects," *IEEE Trans. Antennas Propagat.*, vol. 34, no. 6, pp. 758–766, June 1986.

[27] T. K. Sarkar, E. Arvas, and S. Ponnapalli, "Electromagnetic scattering from dielectric boies," *IEEE Trans. Antennas Propagat.*, vol. 37, no. 5, pp. 673–676, May 1989.

[28] L. N. Medgyesi-Mitschang, J. M. Putnam, and M. B. Gedera, "Generalized method of moments for three-dimensional penetrable scatterers," *J. Opt. Soc. Am. A.*, vol. 11, no. 4, pp. 1383–1398, April 1994.

[29] D. H. Schaubert, D. R. Wilton, and A. W. Glisson, "A tetrahedral modeling method for electromagnetic scattering by arbitrarily shaped inhomogeneous dielectric bodies," *IEEE Trans. Antennas Propagat.*, vol. 32, no. 1, pp. 77–85, Jan 1984.

[30] L. N. Medgyesi-Mitschang and C. Eftimiu, "Scattering from axisymmetric obstacles embedded in axisymmetric dielectrics: The method of moments solution," *Appl. Phys.*, vol. 19, pp. 275–285, 1979.

[31] L. N. Medgyesi-Mitschang and J. M. Putnam, "Electromagnetic scattering from axially inhomogeneous bodies of revolution," *IEEE Trans. Antennas Propagat.*, vol. 32, no. 8, pp. 797–806, August 1984.

[32] J. M. Putnam and L. N. Medgyesi-Mitschang, "Combined field integral equation formulation for inhomogeneous two- and three-dimensional bodies: The junction problem," *IEEE Trans. Antennas Propagat.*, vol. 39, no. 5, pp. 667–672, May 1991.

[33] S. M. Rao, C. C. Cha, R. L. Cravey, and D. L. Wilkes, "Electromagnetic scattering from arbitrary shaped conducting bodies coated with lossy materials of arbitrary thickness," *IEEE Trans. Antennas Propagat.*, vol. 39, no. 5, pp. 627–631, May 1991.

[34] J. M. Jin, V. V. Liepa, and C. T. Tai, "Volume-surface integral formulation for electromagnetic scattering by inhomogeneous cylinders," in *IEEE APS Int. Symp. Dig.*, vol. 1, Syracuse, New York, June 1988, pp. 372–375.

[35] C. C. Lu and W. C. Chew, "A coupled surface-volume integral equation approach for the calculation of electromagnetic scattering from composite

metallic and material targets," *IEEE Trans. Antennas Propagat.*, vol. 48, no. 12, pp. 1866–1868, Dec. 2000.

[36] L. Greengard and V. Rokhlin, "A fast algorithm for particle simulations," *J. Comp. Physics*, vol. 73, no. 2, pp. 325–348, Dec. 1987.

[37] V. Rokhlin, "Rapid solution of integral equations of scattering theory in two dimensions," *J. Comput. Phys.*, vol. 86, no. 2, pp. 414–439, Feb. 1990.

[38] R. Coifman, V. Rokhlin, and S. Wandzura, "The fast multipole method for the wave equation: A pedestrian prescription," *IEEE Antennas Propagat. Mag.*, vol. 35, no. 3, pp. 7–12, June 1993.

[39] C. C. Lu and W. C. Chew, "A fast algorithm for solving hybrid integral equation," *IEE Proceedings-H*, vol. 140, no. 6, pp. 455–460, Dec. 1993.

[40] L. R. Hamilton, P. A. Macdonald, M. A. Stalzer, R. S. Turley, J. L. Visher, and S. M. Wandzura, "3D method of moments scattering computations using the fast multipole method," in *IEEE Antennas Propagat. Int. Symp. Dig.*, vol. 1, June 1994, pp. 435–438.

[41] C. C. Lu and W. C. Chew, "A multilevel algorithm for solving boundary integral equations of wave scattering," *Microwave Opt. Tech. Lett.*, vol. 7, no. 10, pp. 466–470, July 1994.

[42] B. Dembart and E. Yip, "A 3D fast multipole method for electromagnetics with multiple levels," in *Proc. of 11th Annual Review of Progress in Applied Computational Electromagnetics*, vol. 1, Monterey, California, 1995, pp. 621–628.

[43] J. Song and W. C. Chew, "Multilevel fast-multipole algorithm for solving combined field integral equations of electromagnetics scattering," *Microwave Opt. Tech. Lett.*, vol. 10, no. 1, pp. 14–19, Sept. 1995.

[44] J. Song, C. C. Lu, and W. C. Chew, "Multilevel fast multipole algorithm for electromagnetic scattering by large complex objects," *IEEE Trans. Antennas Propagat.*, vol. 45, no. 10, pp. 1488–1493, Oct. 1997.

[45] J. M. Song, C. C. Lu, W. C. Chew, and S. W. Lee, "Fast Illinois Solver Code," *IEEE Antennas Propagat. Mag.*, vol. 40, no. 3, pp. 27–34, June 1998.

[46] T. K. Sarkar, E. Arvas, and S. M. Rao, "Application of FFT and the conjugate gradient method for the solution of electromagnetic radiation from electrically large and small conducting bodies," *IEEE Trans Antennas Propagat.*, vol. 34, no. 5, pp. 635–640, May 1986.

[47] E. Bleszynski, M. Bleszynski, and T. Jaroszewicz, "A fast integral equation solver for electromagnetic scattering problems," in *IEEE APS Int. Symp. Dig.*, vol. 1, 1994, pp. 416–419.

[48] E. Bleszynski, M. Bleszynski, and T. Jaroszewicz, "AIM: Adaptive Integral Method for solving large-scale electromagnetic scattering and radiation problems," *Radio Sci.*, vol. 31, no. 5, pp. 1225–1251, Sept.-Oct. 1996.

[49] F. Ling, C. F. Wang, and J. M. Jin, "Application of adaptive integral method to scattering and radiation analysis of arbitrarily shaped planar structures," *J. Electromag. Waves Applicat.*, vol. 12, no. 8, pp. 1021–1037, Aug. 1998.

[50] C. F. Wang, F. Ling, J. Song, and J. M. Jin, "Adaptive integral solution of combined field integral equation," *Microwave Opt. Tech. Lett.*, vol. 19, no. 5, pp. 321–328, Dec. 1998.

[51] S. Bindiganavali, J. L. Volakis, and H. Anastassiu, "Scattering from plates containing small features using the adaptive integral method(AIM)," *IEEE Trans. Antennas Propagat.*, vol. 46, no. 12, pp. 1867–1878, Dec. 1998.

[52] F. Ling, C. F. Wang, and J. M. Jin, "An efficient algorithm for analyzing large-scale microstrip structures using adaptive integral method combined

with discrete complex-image method," *IEEE Trans. Microwave Theory Tech.*, vol. 48, no. 5, pp. 832–839, May 2000.

[53] Z. Q. Zhong and Q. H. Liu, "A volume Adaptive Integral Method (VAIM) for 3-D inhomogeneous objects," *IEEE Antennas and Wireless Propagat. Letters*, vol. 1, no. 5, pp. 102–105, 2002.

[54] W. B. Ewe, L. W. Li, and M. S. Leong, "Solving mixed dielectric/conducting scattering problem using adaptive integral method," in *Progress In Electromagnetics Research*, J. A. Kong, Ed. Cambridge, Boston: EMW Publishing, 2004, vol. 46, pp. 143–163.

[55] W. B. Ewe, L. W. Li, and M. S. Leong, "Fast solution of mixed dielectric/conducting scattering problem using volume-surface adaptive integral method," *IEEE Trans. Antennas Propagat.*, vol. 52, no. 11, pp. 3071–3077, Nov. 2004.

[56] W. B. Ewe, L. W. Li, Q. Wu, and M. S. Leong, "AIM solution to electromagnetic scattering using parametric geometry," *IEEE Antennas and Wireless Propagation Letter*, Jan. 2005, accepted for publication.

[57] W. B. Ewe, L. W. Li, Q. Wu, and M. S. Leong, "Analysis of reflector and horn antennas using adaptive integral method," *IEICE Transactions on Communications: Special Section on 2004 International Symposium on Antennas and Propagation*, vol. E88-B, no. 6, June 2005.

[58] J. R. Phillips and J. White, "A precorrected-FFT method for capacitance extraction of complicated 3-d structures," in *Proc. of Int. Conf. on Computer-Aided Design*, Santa Clara, California, Nov. 1994, pp. 268–271.

[59] J. R. Phillips and J. K. White, "A precorrected-FFT method for electrostatic analysis of complicated 3-d structures," *IEEE Transactions on Computer-Aided Design of Integrated Circuits and Systems*, vol. 16, no. 10, pp. 1059–1072, Oct. 1997.

[60] X. Nie, L. W. Li, N. Yuan, and T. S. Yeo, "Fast analysis of scattering by arbitrarily shaped three-dimensional objects using the precorrected-FFT method," *Microwave Opt. Tech. Lett.*, vol. 34, no. 6, pp. 438–442, Sept. 2002.

[61] T. J. Peters and J. L. Volakis, "Application of a conjugate gradient fft method to scattering from thin planar material plates," *IEEE Trans. Antennas Propagat.*, vol. 36, no. 4, pp. 518–526, Apr. 1988.

[62] M. F. Catedra, J. G. Cuevas, and L. Nuno, "A scheme to analyze conducting plates of resonant size using the conjugate gradient method and the fast Fourier transform," *IEEE Trans. Antennas Propagat.*, vol. 36, no. 12, pp. 1744–1752, Dec. 1988.

[63] M. F. Catedra and E. Gago, "Spectral domain analysis of conducting patches of arbitrary geometry in multilayer media using CG-FFT method," *IEEE Trans. Antennas Propagat.*, vol. 38, no. 10, pp. 1530–1536, Oct. 1990.

[64] J. M. Jin and J. L. Volakis, "A biconjugate gradient FFT solution for scattering by planar plates," *Electromagnetics*, vol. 12, no. 1, pp. 105–119, Jan.–Mar. 1992.

[65] P. Zwamborn and P. V. den Berg, "Three dimensional weak form of the conjugate gradient FFT method for solving scattering problems," *IEEE Trans. Microwave Theory Tech.*, vol. 40, no. 9, pp. 1757–1766, Sept. 1992.

[66] H. Gan and W. C. Chew, "A discrete BCG-FFT algorithm for solving 3d inhomogeneous scatterer problems," *J. Electromag. Waves Appl.*, vol. 9, no. 10, pp. 1339–1357, July 1995.

[67] C. F. Wang, F. Ling, and J. M. Jin, "A fast full-wave analysis of scattering and radiation from large finite arrays of microstrip antennas," *IEEE Trans. Antennas Propagat.*, vol. 46, no. 10, pp. 1467–1474, Oct. 1998.

[68] X. M. Xu and Q. H. Liu, "Fast spectral-domain method for acoustic scattering

problems," *IEEE Trans. Ultrasonics, Ferroelectrics, and Frequency Control*, vol. 48, no. 2, pp. 522–529, March 2002.

[69] A. F. Peterson, S. L. Ray, and R. Mittra, *Computational Methods for Electromagnetics*, New York : IEEE Press, and Oxford, U.K.: Oxford University Press, 1998.

[70] R. Mittra, Ed., *Computer Techniques for Electromagnetics*. Elmsford, NY: Pergamon Press, 1973.

[71] T. Itoh, Ed., *Numerical Techniques for Microwave and Millimeter-Wave Passive Structures*. New York: John Wiley and Sons, 1989.

[72] R. C. Hansen, Ed., *Moment Methods in Antennas and Scattering*. Norwood, MA: Artech House, 1990.

[73] J. H. H. Wang, *Generalized Moment Methods in Electromagnetics: Formulation and Computer Solution of Integral Equations*. New York: John Wiley and Sons, 1991.

[74] N. Morita, N. Kumagai, and J. R. Mautz, *Integral Equation Methods for Electromagnetics*. Norwood, MA: Artech House, 1991.

[75] K. Umashankar and A. Tafflove, *Computational Electromagnetics*. Norwood, MA: Artech House, 1993.

[76] B. D. Popovic and B. M. Kolundzija, *Analysis of Metallic Antennas and Scatterers*. London: IEE, 1994.

[77] R. F. Harrington, *Time-Harmonic Electromagnetic Fields*. New York, NY: McGraw-Hill, 1961.

[78] C. A. Balanis, *Advanced Engineering Electromagnetics*. New York, NY: John Wiley & Sons, 1989.

[79] T. K. Sarkar, A. R. Djordević, and E. Arvas, "On the choice of expansion and weighting functions in the numerical solution of operator equations," *IEEE Trans. Antennas Propagat.*, vol. 33, no. 9, pp. 988–996, Sept. 1985.

[80] R. D. Graglia, D. R. Wilton, and A. F. Peterson, "High order interpolatory vector bases for computational electromagnetics," *IEEE Trans. Antennas and Propagat.*, vol. 45, no. 3, pp. 329–342, Mar. 1997.

[81] GiD – The personal pre and post processor. [Online]. Available: http://gid.cimne.upc.es/

[82] W. C. Chew, J. M. Jin, E. Michielssen, and J. M. Song, *Fast and Efficient Algorithms in Computational Electromagnetics*. Norwood, MA: Artech House, 2001.

[83] A. F. Peterson, "The interior resonance problem associated with surface integral equations of electromagnetics: Numerical consequences and a survey of remedies," *Electromagnetics*, vol. 10, no. 3, pp. 293–312, 1990.

[84] Y. Saad and M. H. Schultz, "GMRES: A generalized minimal residual algorithm for solving nonsymmetric linear systems," *SIAM J. Sci. Stat. Comp.*, vol. 7, no. 3, pp. 856–869, July 1986.

[85] A. C. Woo, H. T. G. Wang, M. J. Schuh, and M. L. Sanders, "Benchmark radar targets for the validation of computational electromagnetics programs," *IEEE Antennas Propagat. Mag.*, vol. 35, no. 1, pp. 84–89, Feb. 1993.

[86] W. B. Ewe, L. W. Li, and M. S. Leong, "Analysis of reflector and horn antennas using adaptive integral method," in *Proc. of the 2004 International Symposium on Antennas and Propagation*, Sendai, Japan, August 17-21 2004, pp. 229–232.

[87] A. Heldring, J. M. Rius, J. Parron, A. Cardama, and L. P. Ligthart, "Analysis of reflector and horn antennas using multilevel fast multipole algorithm,"

in *Millenium Conference on Antennas and Propagation (AP2000)*, Davos, Switzerland, April 2000.

[88] K. C. Donepudi, J. M. Jin, and W. C. Chew, "A higher order multilevel fast multipole algorithm for scattering from mixed conducting/dielectrics bodies," *IEEE Antennas Propagat. Mag.*, vol. 51, no. 10, pp. 2814–2821, Oct. 2003.

[89] Y. J. Wang, X. C. Nie, L. W. Li, and E. P. Li, "A parallel analysis of the scattering from inhomogeneous dielectric bodies by the volume integral equation and the precorrected-FFT algorithm," *Microwave Opt. Technol. Lett.*, vol. 42, no. 1, pp. 77–79, July 2004.

[90] J. Liu and J. M. Jin, "A novel hybridization of higher order finite element and boundary integral methods for electromagnetic scattering and radiation problems," *IEEE Trans. Antennas Propagat.*, vol. 49, no. 12, pp. 1794–1806, Dec. 2001.

[91] Y. Saad, *Iterative Methods for Sparse Linear Systems*. Boston, MA: PWS Publishing, 1996.

[92] K. Chen, "On a class of preconditioning methods for dense linear systems from boundary elements," *SIAM J. Sci. Comput.*, vol. 20, no. 2, pp. 684–698, 1998.

[93] B. Carpentieri, I. S. Duff, and L. Giraud, "Experiments with sparse preconditioning of dense problems from electromagnetic applications," CERFACS, Toulouse, France, Technical Report TR/PA/00/04, 2000.

[94] N. Munksgaard, "Solving sparse symmetric sets of linear equations by preconditioned conjugate gradient method," *ACM Transactions on Mathematical Software*, vol. 6, no. 2, pp. 206–219, June 1980.

[95] P. Concus, G. H. Golub, and G. Meurant, "Block preconditioning for the conjugate gradient method," *SIAM Journal on Scientific and Statistical Computing*, vol. 6, no. 1, pp. 220–252, Jan. 1985.

[96] G. H. Golub and C. F. V. Loan, *Matrix Computations*, 2nd ed. Baltimore, MD: The Johns Hopkins University Press, 1989.

[97] H. C. Elman and E. Argon, "Ordering techniques for the preconditioned conjugate gradient method on parallel computers," *Computer Physics Communications*, vol. 53, no. 1–3, pp. 253–269, May 1989.

[98] W. B. Ewe, L. W. Li, Q. Wu, and M. S. Leong, "Preconditioners for adaptive integral method implementation," *IEEE Trans. Antennas Propagat.*, Jan. 2005, accepted for publication.

[99] W. B. Ewe, L. W. Li, and M. S. Leong, "A novel preconditioner (ILU) for adaptive integral method implementation in solving large-scale electromagnetic scattering problem of composite dielectric and conducting objects," in *Proc. of the 5th ARPU Doctoral Student Conference* (in CD format and web-database), Sydney, Australia, August 9-13 2004.

[100] W. B. Ewe, L. W. Li, and M. S. Leong, "Preconditioning techniques for adaptive integral method implementation in fast codes," in *Proc. of the 2004 Progress In Electromagnetics Research Symposium (PIERS'04)*, Nanjing, China, August 28-31 2004, p. 29.

[101] Y. Saad, "ILUT: a dual threshold incomplete LU preconditioner," *Numer. Linear Algebra Appl.*, vol. 1, no. 4, pp. 387–402, 1994.